



Dipl.-Ing. Thomas Holzer

**Design of Electrically Excited Salient-Pole  
Synchronous Motor-Generators for  
Full-Size Converter Operation of  
Large Pumped Storage Power Plants**

**DISSERTATION**

to obtain the university degree of  
Doktor der technischen Wissenschaften (Dr. techn.)

submitted to

**Graz University of Technology, Austria**

Supervisor and First Assessor:

Prof. Annette Mütze

Electric Drives and Machines Institute, Graz University of Technology, Austria

Second Assessor:

Prof. Boštjan Polajžer

Institute of Electrical Power Engineering, University of Maribor, Slovenia

Graz, October 2020



## AFFIDAVIT

I declare that I have authored this thesis independently, that I have not used other than the declared sources/resources, and that I have explicitly indicated all material which has been quoted either literally or by content from the sources used. The text document uploaded to TUGRAZonline is identical to the present doctoral thesis.

.....  
Date

.....  
Signature



*“Continuous improvement is better  
than delayed perfection.”*

-Mark Twain



# Contents

<b>Table of Contents</b>	<b>I</b>
<b>Abstract</b>	<b>VII</b>
<b>Kurzfassung</b>	<b>IX</b>
<b>Acknowledgements</b>	<b>XI</b>
<b>1 Introduction</b>	<b>1</b>
1.1 Motivation . . . . .	3
1.2 Thesis Objectives . . . . .	4
1.3 Assumptions and Limitations . . . . .	4
1.4 Original Scientific Contribution . . . . .	6
1.5 Thesis Overview . . . . .	7
1.6 List of Publications . . . . .	8
<b>2 State-of-the-Art in Variable-Speed Pumped Storage Power Plants</b>	<b>9</b>
2.1 Pumped Storage Power Plants . . . . .	9
2.2 Conventional Operation of Pumped Storage Power Plants . . . . .	11
2.2.1 Conventional Directly Line-Connected Arrangements . . . . .	11
2.2.2 Start-Up Converter . . . . .	12
2.2.3 Power Converter for Pumping Mode . . . . .	13
2.2.4 Example Cases for Power Converter Operation . . . . .	13
2.3 Doubly-Fed Induction Machine . . . . .	16
2.4 Full-Size Converter Operated Electrically Excited Salient-Pole Synchronous Machine . . . . .	17
2.5 Economic Considerations . . . . .	18
<b>3 Generator Design for Full-Size Converter Operation - Design Techniques</b>	<b>21</b>

3.1	Generator Design Approach for Conventional Directly Line-Connected Operation . . . . .	21
3.2	Generator Design Approach for Full-Size Converter Operation . . . .	23
3.2.1	Electrically Excited Salient-Pole Synchronous Machine Design Process . . . . .	24
3.2.2	Optimization Process . . . . .	30
<b>4</b>	<b>Generator Design for Full-Size Converter Operation - Computational Results</b>	<b>35</b>
4.1	Example Case for Operation at Unity Power Factor . . . . .	35
4.2	Optimum Design Frequency . . . . .	37
4.2.1	Example Case for Design Frequencies Different than 50 Hz . .	37
4.2.2	Influence of the Rotational Speed . . . . .	40
4.2.3	Influence of the Machine Utilization . . . . .	42
4.2.4	Influence of the Cost Factors . . . . .	43
4.3	Operation at a Load Profile . . . . .	46
4.3.1	Turbine Mode . . . . .	46
4.3.2	Pumping Mode . . . . .	49
4.3.3	Generator Design for Operation at a Load Profile . . . . .	50
4.3.4	Summary of the Generator Design for Operation at a Load Profile	53
4.4	Synchronous Reactance . . . . .	53
4.5	Power Factor . . . . .	55
4.5.1	Power Loss Distribution for Various Power Factors . . . . .	56
4.5.2	Generator Design for Under-Excited Operation . . . . .	58
4.6	Summary of the Generator Design Aspects for FSC Operation . . . .	59
4.6.1	Power Factor . . . . .	59
4.6.2	Design Frequency . . . . .	59
4.6.3	Operation at a Load Profile . . . . .	60
4.6.4	Synchronous Reactance . . . . .	60
4.7	Suggested Generator Design for FSC Operation . . . . .	60
<b>5</b>	<b>Power Converter Topologies for Medium-Voltage High-Power Applications</b>	<b>63</b>
5.1	Particularities of Power Converter Application in Large Pumped Storage Power Plants . . . . .	64
5.2	Review of Semiconductor Power Switches for High-Power Applications	65

5.3	Multilevel Voltage Source Converter Topologies . . . . .	67
5.3.1	Neutral Point Clamped and Flying Capacitor Voltage Source Converters . . . . .	67
5.3.2	Cascaded H-Bridge Voltage Source Converter . . . . .	69
5.3.3	H-Bridge Neutral Point Clamped Voltage Source Converter . . . . .	69
5.3.4	Advanced Multilevel Topologies . . . . .	69
5.3.5	Bidirectional Power Flow of Multilevel Voltage Source Converters . . . . .	69
5.4	Direct AC-AC Power Converters . . . . .	71
5.4.1	Matrix Converter . . . . .	71
5.4.2	Multi-Modular Matrix Converter . . . . .	71
5.5	Fully Scalable Modular Multilevel Converter Topologies . . . . .	73
5.5.1	Modular Multilevel Converter . . . . .	73
5.5.2	Modular Multilevel Matrix Converter . . . . .	76
5.6	Power Converter Manufacturer Overview . . . . .	77
5.6.1	Details on the Individual Power Converters . . . . .	77
5.6.2	Evaluation for Application in Large PSPPs . . . . .	78
5.7	Summary of Power Converter Topologies for Application in Large PSPPs . . . . .	79
<b>6</b>	<b>Analysis of the Modular Multilevel Converter for Application in Large Pumped Storage Power Plants</b> . . . . .	<b>81</b>
6.1	Analysis of the Modular Multilevel Converter - Tools . . . . .	81
6.1.1	Model Parameters of the MMC . . . . .	81
6.1.2	Objectives for the MMC Analysis Tools . . . . .	83
6.1.3	MMC PWM Voltage Waveform Generation Tool . . . . .	83
6.1.4	Simulation Model of the MMC for Analysis of the Switching Behavior . . . . .	86
6.1.5	Analytic Average Loss Model of the MMC . . . . .	88
6.2	Analysis of the Modular Multilevel Converter - Results . . . . .	89
6.2.1	Analysis of the THD of the MMC . . . . .	89
6.2.2	Analysis of the Efficiency of the MMC at Nominal Load . . . . .	90
6.2.3	Efficiency of the Full-Size Converter and the Synchronous Motor-Generator at Nominal Load and Partial Load . . . . .	91
6.3	Summary . . . . .	94

<b>7 Damper Winding Harmonics Analysis at Full-Size Converter Supply - Techniques</b>	<b>95</b>
7.1 Test Bench Setup . . . . .	95
7.2 Theoretical Analysis of the Synchronous Machine's Harmonics . . . .	98
7.2.1 Harmonics Caused by the Synchronous Machine's Geometry	98
7.2.2 Harmonics Caused by the Full-Size Converter Supply . . . . .	99
7.3 Damper Winding Characterization . . . . .	103
7.3.1 Damper Winding Shielding Effect Analysis . . . . .	104
7.3.2 Damper Winding Damping Effect Analysis . . . . .	105
<b>8 Damper Winding Harmonics Analysis at Full-Size Converter Supply - Results</b>	<b>109</b>
8.1 Harmonic Spectrum Analysis of the SM at Line-Connected No-Load Operation . . . . .	109
8.1.1 2D Finite Element Analysis . . . . .	110
8.1.2 Experimental Analysis . . . . .	112
8.2 Motor Operation of the SM at Various Supply Voltages Under Load Condition . . . . .	114
8.2.1 2D Finite Element Analysis . . . . .	114
8.2.2 Experimental Analysis . . . . .	116
8.3 Summary . . . . .	122
<b>Conclusion</b>	<b>125</b>
<b>Symbols and Abbreviations</b>	<b>129</b>
<b>Bibliography</b>	<b>137</b>
<b>A Computation of the Power Loss of the Synchronous Generator</b>	<b>147</b>
A.1 Load Dependent Power Losses . . . . .	147
A.2 Constant Power Losses . . . . .	149
<b>B Power Loss and Cost Distribution of the Generator Designs for FSC Operation</b>	<b>151</b>
B.1 Power Loss Distribution . . . . .	151
B.2 Cost Distribution . . . . .	152

<b>C</b>	<b>Generator Design for Operation at a Load Profile for Common Design</b>	
	<b>Frequencies</b>	<b>155</b>
	C.1 Power Loss Distribution . . . . .	156
	C.2 Cost . . . . .	156
	C.3 Summary . . . . .	157
<b>D</b>	<b>Analytic Average Loss Model of the Modular Multilevel Converter</b>	<b>159</b>
	D.1 Average Currents Through the Semiconductor Power Devices . . . . .	159
	D.2 On-State Power Loss . . . . .	160
	D.3 Switching Power Loss . . . . .	161
	D.4 Total Power Loss and Efficiency . . . . .	162
<b>E</b>	<b>Test Bench Equipment and Measurement System</b>	<b>163</b>
	E.1 Electrical Machines and Supplies . . . . .	163
	E.2 Measurement System . . . . .	164
	E.3 Measurement Procedure . . . . .	165



# Abstract

Large-scale energy storage systems have become increasingly important in the context of increasing integration of renewable energy sources like wind and solar. Large pumped storage power plants are particularly well suited for this application. Implementing a variable-speed technology, i.e., the full-size converter operated synchronous motor-generator, when utilizing a combined pump-turbine, allows the adjustment of the active power not only in turbine mode, but also in pumping mode. The adjustable power range in both modes of operation enables the pumped storage power plant to also participate in the balancing energy market which increases the achievable earnings of the power plant. The possibility to operate at variable-speed provided by the full-size converter operation also allows to provide the two different optimum rotational speeds in turbine and pumping modes for the combined reversible-speed pump-turbine and can also be used to increase the turbine efficiency depending on the hydraulic head.

In addition, due to the decoupling of the synchronous machine from the grid, the design criteria for the electrically excited salient-pole synchronous motor-generator change, i.e., the design frequency can be chosen freely, and the machine no longer needs to provide reactive power to the grid, as this part is taken over by the full-size converter. These aspects and the possible savings for the machine's cost are identified within this thesis. The results for an example-case synchronous motor-generator show that it is possible to achieve a cost reduction for the machine designed particularly for full-size converter operation of 18% compared to a conventional directly line-connected synchronous motor-generator.

The full-size converter operation of large hydropower generators corresponds to a medium-voltage high-power application with bidirectional power flow. In addition, very smooth sinusoidal supply voltage waveforms at the machine terminals are required to not cause additional power loss in the machine and to not cause additional stress on the winding insulation. All these requirements can be met with a modular multilevel converter. Therefore, this thesis investigates this power converter topol-

ogy for application as a full-size converter in large pumped storage power plants. The total efficiency of the system comprising the full-size converter and the synchronous machine is illustrated for operation at nominal and partial load for both turbine and pumping modes. The harmonic content in the stator, damper, and field windings of a custom-built synchronous machine is determined theoretically and analyzed for a purely sinusoidal supply utilizing both results computed by utilizing two-dimensional finite element analysis as well as measurement results obtained from the test bench. In addition, the harmonic content of the machine's windings is obtained from measurements at the test bench for various power converter supplies.

# Kurzfassung

Der weitere Ausbau von erneuerbaren Energien, wie zum Beispiel Windenergie und Solarenergie, benötigt Energiespeichertechnologien im großen Maßstab. Hierfür sind große Pumpspeicherkraftwerke besonders gut geeignet. In Kombination mit einer drehzahlvariablen Technologie, wie zum Beispiel der vollumrichter-gespeisten Synchronmaschine, kann bei Verwendung einer Pumpturbine die Wirkleistung nicht nur im Turbinenbetrieb, sondern auch im Pumpbetrieb beliebig variiert werden. Dies ermöglicht dem Pumpspeicherkraftwerk, zusätzlich am Ausgleichsenergiemarkt teilzunehmen, was wiederum die erzielbaren Einnahmen erhöht. Durch die variable Drehzahl können außerdem die beiden unterschiedlichen optimalen Drehzahlen im Turbinen- und Pumpbetrieb realisiert werden, die sich bei der Verwendung einer kombinierten reversiblen Pumpturbine ergeben. Weiters kann die Drehzahl im Turbinenbetrieb den aktuellen Betriebsbedingungen angepasst und somit auch ein höherer Turbinenwirkungsgrad erzielt werden, der besonders stark von der Fallhöhe abhängt.

Da der Synchrongenerator durch den Betrieb am Vollumrichter nicht mehr direkt mit dem Netz verbunden ist, ergeben sich zusätzliche Freiheitsgrade für das Design der elektrisch erregten Schenkelpol-Synchronmaschine. Zum Beispiel kann die Frequenz für das Generatordesign frei gewählt werden. Außerdem muss der Generator nicht mehr Blindleistung in das Netz einspeisen, da diese Aufgabe bereits vom Vollumrichter erfüllt wird. In dieser Dissertation werden eben diese zusätzlichen Aspekte herausgearbeitet und auch die mögliche Kostenreduktion der Synchronmaschine bei Vollumrichterbetrieb untersucht. Es zeigt sich anhand eines Beispielgenerators, dass es möglich ist, die Kosten einer Synchronmaschine speziell für Vollumrichterbetrieb im Vergleich zu einer konventionellen direkt netzgebundenen Synchronmaschine um 18 % zu reduzieren.

Der Betrieb von großen Wasserkraftgeneratoren entspricht einer Mittelspannungs-Hochleistungs-Anwendung, für die bidirektionaler Leistungsfluss notwendig ist. Zusätzlich müssen die vom Vollumrichter erzeugten Spannungsverläufe möglichst

sinusförmig sein, damit in der Synchronmaschine keine zusätzlichen Verluste verursacht werden und auch keine zusätzliche Beanspruchung für die Wicklungsisolation entsteht. Diese Anforderungen können mit einem Modular Multilevel Converter erfüllt werden, weshalb diese Umrichtertopologie im Rahmen dieser Dissertation für den Einsatz als Vollumrichter in großen Pumpspeicherkraftwerken untersucht wird. Der Gesamtwirkungsgrad von Vollumrichter und Synchrongenerator wird für Nennlast- und Teillastbetrieb sowohl im Turbinen-, als auch im Pumpbetrieb berechnet und dargestellt. Der Oberschwingungsgehalt in Stator-, Dämpfer- und Erregerwicklung bei Betrieb mit reinem Sinus wird am Beispiel einer speziell konstruierten Synchronmaschine untersucht. Einerseits geschieht dies anhand einer theoretischen Herleitung, andererseits anhand eines zweidimensionalen Modells mithilfe der Finite-Elemente-Methode, sowie zusätzlich messtechnisch am Prüfstand. Außerdem wird der Oberschwingungsgehalt in den Wicklungen der Synchronmaschine bei Betrieb mit unterschiedlichen Umrichtertopologien messtechnisch am Prüfstand untersucht.

# Acknowledgements

First of all, I want to thank my supervisor Prof. Dr.-Ing. Annette Mütze for the opportunity to write this thesis at the Electric Drives and Machines Institute at Graz University of Technology and for her support and advice during my research activity.

Next, I would like to thank Prof. Dr. Boštjan Polajžer from the Institute of Electrical Power Engineering at the University of Maribor for taking on the role as a second assessor and for the interesting discussions we had, particularly during his stay in Graz.

Many thanks go to Dr.-Ing. Georg Traxler-Samek for generously sharing his immense knowledge about hydropower generators and to DI Michael Lecker and Dr. Franz Zerobin for the enjoyable meetings throughout the course of this research project. The financial support by Andritz Hydro GmbH, Weiz, Austria is gratefully acknowledged.

Furthermore, I would like to thank Dr. Johann Bacher for the great collaboration regarding the test bench and the measurements carried out as well as Ewald Seelmeister for his enormous support in the workshop.

I also want to thank my friends and the whole team from the Electric Drives and Machines Institute for making the process of writing this thesis a pleasant journey.

The completion of this thesis was only possible because of the tremendous support and encouragement of my family, especially of my mother Monika Holzer and my girlfriend Mag. Johanna Ziegerhofer. A huge thanks to them!



# Chapter 1

## Introduction

Further implementation of renewable energy sources like wind and solar has increased the requirements placed upon energy generation and storage with conventional power plants. The need to reduce the response time for quickly storing and releasing large amounts of energy has increased the interest in the integration of power converters in pumped storage power plants. The use of a variable rotating speed provided by the full-size converter represents a reasonable approach [1–5].

### **Benefits of the Full-Size Converter Operated Synchronous Motor-Generator**

The main reason to implement a variable-speed technology in a pumped storage power plant is the active power control in pumping mode. The active power generated in turbine mode can always be controlled by the water flow rate across the turbine. However, the power consumption of a pump is linked to the rotational speed and therefore, with a conventional directly line-connected synchronous machine, it is not possible to control the absorbed power in pumping mode because of the fixed frequency of the grid. The only option to allow for a variable power consumption with a fixed-speed arrangement is the use of a separate turbine and pump which requires two hydraulic machines and additional hydraulic equipment.

With the full-size converter operated synchronous motor-generator both turbine and pumping modes can be achieved with a single combined reversible-speed pump-turbine, which requires two different directions of rotation. With the use of this technology, the active power can be controlled in both operating modes.

For these combined pump-turbines, the optimum rotational speed differs for turbine and pumping modes. Hence, depending on the operating mode, adjusting the rotational speed increases the efficiency of the pump-turbine. Furthermore, the turbine efficiency can be optimized for a certain operating point, which largely depends

on the hydraulic head and the load.

Being able to control the active power both in turbine and pumping modes allows the pumped storage power plant to participate in the balancing energy market which increases the achievable earnings significantly compared to participation in energy markets only, as the conventional approach does [6–8].

Furthermore, the reactive power can be provided to the grid by the full-size converter, even during machine standstill.

Especially the compliance with the low voltage ride-through requirements of today's grid codes has gained a lot of attention. It can be achieved more easily with a full-size converter operated synchronous machine than with a doubly-fed induction machine [9, 10], which represents the second possible topology to enable variable-speed operation. In contrast to the doubly-fed induction machine, the full-size converter operated synchronous machine also allows pump start-up directly in water and hence, fast start-up times can be realized. The full-size converter operated synchronous machine also allows for a larger variable-speed range, and therefore, a larger adjustable power range than the doubly-fed induction machine.

### **Generator Design Possibilities for Full-Size Converter Operation**

With the absence of a direct grid connection of the synchronous motor-generator due to the full-size converter, certain design parameters of the machine can be more freely chosen: The design frequency can be chosen independently of the grid frequency, the power factor can be used for an optimized machine design, and the synchronous reactance is no longer set by the requirements of the grid [11].

Design parameters that do not change at full-size converter operation compared to a conventional design are the rotational speed, since this parameter is set by the optimum pump-turbine design by the hydraulic head of the power plant, and the mass moment of inertia, which is required to prevent temporary over-speed and turbine runaway [12].

### **Requirements for the Full-Size Converter**

The full-size converter operation of large hydropower generators in pumped storage power plants corresponds to a medium-voltage ( $\geq 13.5$  kV) high-power ( $\geq 100$  MW) regenerative power (bidirectional power flow) application. These requirements need to be fulfilled by the power converter topology in addition to providing smooth

sinusoidal voltage waveforms for the synchronous motor-generator to reduce the additional power loss during operation and to not cause additional stress for the winding insulation. Particularly the damper winding of the electrically excited synchronous machine, which was originally designed to protect the field winding from large induced voltages caused by unbalanced loads, mechanical oscillations, and transient conditions, is now also subject to the additional harmonics in the air-gap field caused by the full-size converter. It is difficult to achieve smooth sinusoidal waveforms and to fulfill the requirements for the voltage and power rating with conventional multilevel power converter topologies used in today's industrial drive applications. Hence, modular multilevel converter topologies have gained a lot of attention because of their arbitrary scalability and excellent performance [13, 14].

## 1.1 Motivation

Being able to react to the current grid requirements more quickly and to increase the earnings by participating in the balancing energy market requires a variable-speed topology to drive the combined reversible-speed pump-turbines in large pumped storage power plants. This is enabled by the full-size converter operated synchronous motor-generator, forming a highly flexible energy storage technology. As a matter of fact, thus far power converters for pumped storage power plants have been mainly selected to meet the demands of conventionally designed machines and of retrofit applications. The new optimization possibilities for the synchronous motor-generator design given by the full-size converter operation have not yet found much attention in the literature. However, when planning and realizing a new pumped storage power plant, the investment cost is, of course, of high importance. Exploiting the modified generator design requirements that are identified in this thesis, due to the full-size converter operation, it is possible to reduce the total cost of the electrically excited salient-pole synchronous motor-generator by 18 %, see Section 4.7.

The full-size converter operation of large pumped storage power plants corresponds to a medium-voltage high-power application with bidirectional power flow. Operating the electrically excited synchronous motor-generator with a full-size converter can result in additional stress for the machine winding insulation and additional power loss which largely depends on the utilized power converter topology. Therefore, identifying a power converter topology capable of supplying the large hydropower generators is of utmost importance. Particularly, the more common

power converter topologies for industrial applications cannot be scaled arbitrarily to achieve the required voltage and power rating and they also lead to a quite stressful operation for the synchronous machine. This is investigated in Section 8.3, utilizing measurements for the harmonic content of the stator, damper, and field windings of a custom-built synchronous machine at the test bench supplied by various full-size converter topologies.

## 1.2 Thesis Objectives

The aim of this thesis is to elaborate the design criteria for electrically excited salient-pole synchronous motor-generators for full-size converter operation in large pumped storage power plants. Therefore, the additional aspects and degrees of freedom for the synchronous motor-generator design when being decoupled from the grid are identified. Utilizing a tailored generator design tool for this particular type of operation, which needed to be developed, the effects of various design parameters on the total cost of the synchronous motor-generator, which considers both costs for materials as well as costs for power loss during operation, should be analyzed.

Out of the various power converter topologies available, a promising power converter topology for the operation of large synchronous motor-generators in pumped storage power plants is identified which needs to allow for medium-voltage high-power bidirectional power flow. The aim is to develop tools to characterize the operational behavior of this power converter topology and to then identify the total efficiency of the system comprising both the machine and the full-size converter.

The additional harmonic content in the stator, damper, and field windings of the synchronous machine should be analyzed utilizing measurements obtained from a custom-built synchronous machine at the test bench for various full-size converter topologies.

## 1.3 Assumptions and Limitations

Within this thesis, the definition of a large pumped storage power plant transfers to a minimum power rating of 100 MW for a single machine. A typical voltage rating of such an electrically excited salient-pole synchronous motor-generator is a line-to-line voltage of 13.5 kV [5] which is defined as the minimum line-to-line voltage within this thesis. A typical voltage rating of a 500 MVA synchronous motor-generator would

be 21 kV [15] which represents the upper limit for the machine's rated voltage. It is assumed that the machine is connected to the grid at a higher voltage level via a block transformer, i.e., to a voltage level of 110 kV.

The possibilities for the synchronous motor-generator design due to the full-size converter operation are investigated for the example case of a 135 MW, 13.5 kV, 200 rpm electrically excited salient-pole synchronous motor-generator. To identify the relationships between the sources of power loss, a simplified power loss model is utilized. It is assumed that the additional power loss due to a non-ideal waveform of the full-size converter can be neglected when utilizing a multilevel power converter topology with a high number of levels. Use of such an extremely high number of levels is assumed to be necessary considering the investigated voltage and power rating. The damper winding power loss and the pole-shoe surface power loss are not taken into account in the simplified power loss model.

While the cost of the synchronous motor-generator is computed using typical values for the active material and the power loss [11], for the full-size converter only the power converter topology is assumed, since accurate data for the cost of the full-size converter is not available. For the full-size converter it is assumed, that the voltage rating on the machine side and the grid side is identical. To compute the power conversion efficiency of the full-size converter, an analytic average loss model for the modular multilevel converter topology is used. This model utilizes average currents and assumes sinusoidal waveforms [16] to compute the switching and on-state power losses. Additional power loss caused by the passive components, i.e., the submodule capacitors and the arm inductors, are neglected. It is assumed that the utilized power semiconductor devices in parallel are turned on and off simultaneously and carry the same current.

The harmonics in the stator, damper, and field windings caused by the full-size converter are analyzed for a custom-built electrically excited synchronous machine at the test bench for motor operation only. This machine has a rated mechanical power of 3.9 kW. The harmonics in the stator, damper, and field windings at a purely sinusoidal supply are also analyzed by finite element analysis for a two-dimensional model of the machine. Hence, potential additional effects due to the end-winding region are neglected within the simulation.

## 1.4 Original Scientific Contribution

The additional degrees of freedom for the synchronous motor-generator design given by the full-size converter operation have not yet found much attention in the literature. This thesis elaborates the design criteria for electrically excited salient-pole synchronous motor-generators for full-size converter operation in large pumped storage power plants. The potential savings of the machine's cost are investigated when applying the various identified generator design aspects, namely, the free choice of the design frequency, the power factor, and the synchronous reactance, as well as considering operation at a load profile.

Several reviews of power converter topologies for medium-voltage applications are available. However, they do not specifically deal with the required voltage and power rating, namely  $\geq 13.5$  kV and  $\geq 100$  MW, and the investigated power converter topologies generally do not allow for bidirectional power flow. This thesis closes this gap by providing an overview of the possible choices of power converter topologies for operating large synchronous motor-generators in pumped storage power plants as well as by identifying their individual advantages and disadvantages.

This thesis shows results for the efficiency of the system comprising the synchronous motor-generator and the full-size converter for operation at a load profile in both turbine and pumping modes. These results are compared to the efficiency of a conventional directly line-connected synchronous motor-generator also operating at a load profile, where partial load operation is only possible in turbine mode due to the fixed operating frequency.

When operating large synchronous motor-generators with a full-size converter, the additional harmonic content in the stator, damper, and field windings is of interest because of the additional power loss caused and the additional stress for the winding insulation. While such an analysis is often carried out utilizing finite element analysis, this thesis shows results for the measured harmonic content of the stator, damper, and field windings for a custom-built electrically excited synchronous machine. To this aim, the synchronous machine is equipped with a measurement system that allows the voltage drops to be measured at six damper bars corresponding to one pole of the four-pole machine. The measured power consumption at the machine terminals as well as the harmonic spectra for various full-size converter supplies are compared to measurements carried out for operation at a purely sinusoidal supply.

## 1.5 Thesis Overview

**Chapter 2** reviews the established concepts of conventional pumped storage power plants and identifies the advantages when utilizing a variable-speed topology compared to a conventional fixed-speed topology. It also presents the full-size converter operated electrically excited salient-pole synchronous motor-generator topology which is investigated throughout this thesis.

**Chapter 3** describes the generator design and optimization process developed to allow creating generator designs specifically for full-size converter operation, including the additional aspects and possibilities enabled by the full-size converter operation which are identified in this Chapter as well.

**Chapter 4** presents the various electrically excited salient-pole synchronous motor-generator designs that have been created and provides a suggestion for the generator design specifically for full-size converter operation.

**Chapter 5** analyzes the various power converter topologies available for medium-voltage high-power drive applications, particularly for application in large pumped storage power plants. It also identifies the modular multilevel converter as a promising full-size converter topology to operate the large synchronous motor-generators.

**Chapter 6** describes the implemented models to compute the total harmonic distortion as well as the efficiency of the modular multilevel converter. The total efficiency of the system, comprising the machine and the full-size converter, is presented as well.

**Chapter 7** depicts the test bench setup to measure the harmonic content of the stator, damper, and field windings of a custom-built synchronous machine at various full-size converter supplies.

**Chapter 8** shows the measurement results for the harmonic content of the synchronous machine's windings and illustrates the importance of choosing a suitable full-size converter topology to operate synchronous motor-generators in large pumped storage power plants.

## 1.6 List of Publications

The work presented in this thesis has resulted in the following three journal and two conference publications. These papers are subjected to copyright by the particular publishers. The journal publication J1 is an extended version of the conference publication C2.

### Journal Publications:

- J1 T. Holzer**, A. Muetze, G. Traxler-Samek, M. Lecker, and F. Zerobin, “Generator Design Possibilities for Full-Size Converter Operation of Large Pumped Storage Power Plants,” *IEEE Transactions on Industry Applications*, vol. 56, no. 4, pp. 3644–3655, Jul-Aug 2020.
- J2 T. Holzer** and A. Muetze, “A Comparative Survey of Power Converter Topologies for Full-Size Converter Operation of Medium-Voltage Hydropower Generators,” *e & i Elektrotechnik und Informationstechnik*, vol. 136, no. 6, pp. 263–270, Oct 2019.
- J3 T. Holzer** and A. Muetze, “Full-Size Converter Operation of Hydro Power Generators: A State-of-the-Art Review of Motivations, Solutions, and Design Implications,” *e & i Elektrotechnik und Informationstechnik*, vol. 136, no. 2, pp. 209–215, Jan 2019.

### Conference Publications:

- C1 T. Holzer**, J. Bacher, and A. Muetze, “Damper Winding Harmonics Analysis of an Electrically Excited Synchronous Machine at Power Converter Supply,” 2020 IEEE International Conference on Electrical Machines (ICEM), Gothenburg, Sweden, pp. 1092–1098, 23-26 Aug 2020.
- C2 T. Holzer** and A. Muetze, “Full-Size Converter Operation of Large Hydro Power Generators: Generator Design Aspects,” 2018 IEEE Energy Conversion Congress and Exposition (ECCE), Portland, OR, USA, pp. 7363–7368, 23-27 Sep 2018.

# Chapter 2

## State-of-the-Art in Variable-Speed Pumped Storage Power Plants

*This Chapter reviews motivations and solutions for variable-speed operation in large hydropower plants with a special emphasis on full-size converter operated electrically excited salient-pole synchronous generators. The established concepts of conventional pumped storage power plants are briefly described. Next, the implemented applications with the use of power converters and synchronous machines in hydropower plants, their power ratings, the power converter topologies used, and the experiences obtained during operation are reviewed. The variable-speed capability offered by doubly-fed induction machines with respect to variable-speed pumped storage power plants is briefly described. The requirements for today's power converters and synchronous machines for utilization in large pumped storage power plants as full-size converter operated synchronous generators are identified. Economic considerations concerning the implementation of variable-speed technologies in pumped storage power plants as well as the impact on the total investment cost conclude this Chapter.<sup>1</sup>*

### 2.1 Pumped Storage Power Plants

Pumped storage power plants (PSPP) offer large scale energy storage by converting electrical energy into potential energy. With this aim, water is pumped from the lower reservoir to the upper reservoir, see Figure 2.1. The water from the upper reservoir can then be used to produce electric energy if needed [12]. Therefore, the operating principle of a PSPP is to store excess energy by operating the pump with the synchronous motor, and to produce electrical energy during peak load periods by operating the turbine and using the electrical machine as a generator.

<sup>1</sup>Selected material of this Chapter has also been published in [1].

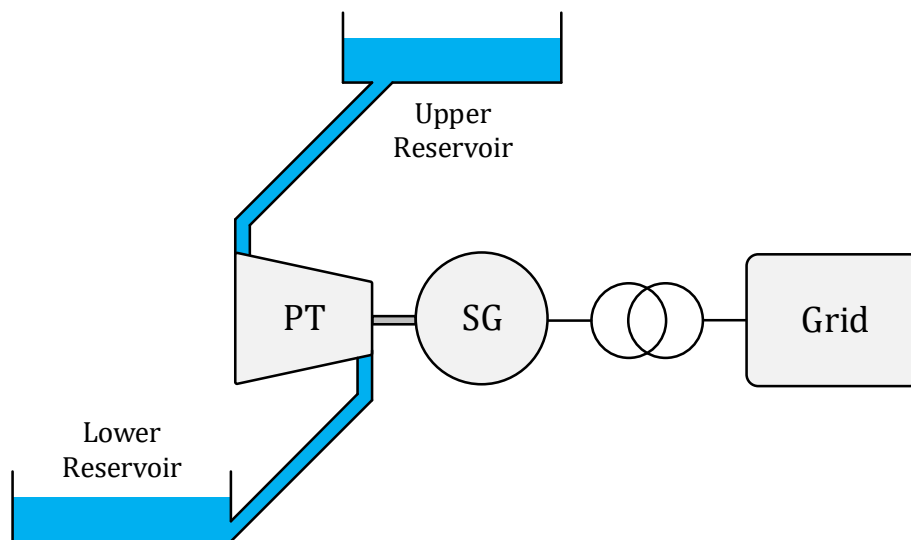


**Figure 2.1:** Block diagram of a pumped storage power plant (PT = Pump-Turbine and SG = Synchronous Motor-Generator).

The choice of the turbine type basically depends on the power plant's hydraulic head (net head) [17]: Kaplan-turbines are typically used up to a net head of 80 m and hence, they are used for run-of-river plants. For PSPPs which have higher net heads Francis-turbines can be used for up to 800 m net head and Pelton-turbines are utilized for applications up to 2000 m net head. Using a Pelton-turbine in a PSPP also requires a separate pump, see Section 2.2.1, while a Francis-turbine can be operated as a pump when reversing the rotational speed [2], see Figure 2.1. Hence, when utilizing a reversible speed Francis pump-turbine, only one hydraulic machine is required for the PSPP.

When designing a turbine, the net head  $H$  and the water flow rate  $Q$  are the main parameters to consider. The mechanical speed for the turbine's design is linked to the net head [18], where a higher net head results in a higher mechanical speed.

Since turbines are designed to achieve high efficiency for one specific parameter set, variations on the hydraulic head as well as partial load operation can lead to a severe reduction of the turbine efficiency [4].

## 2.2 Conventional Operation of Pumped Storage Power Plants

### 2.2.1 Conventional Directly Line-Connected Arrangements

Two main arrangements for the electrical and mechanical machines operating in a PSPP are distinguished from one another:

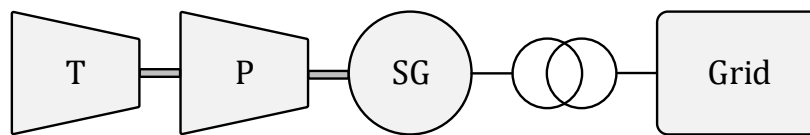


**Figure 2.2:** Block diagram of a PSPP utilizing a ternary machine set (T = Turbine, P = Pump, and SG = Synchronous Motor-Generator).

The first arrangement consists of three machines (ternary machine set, see Figure 2.2): turbine, motor-generator, and pump. These three machines are linked by a common shaft. The rotating direction for this configuration is the same for both turbine and pumping mode. The active power generation in turbine mode can be controlled by the water flow rate across the turbine. For pumping mode, due to the fixed frequency of the directly line-connected motor-generator, the active power is set to one specific value given by the machine design and cannot be controlled. The start-up of the pump is achieved by synchronizing the motor-generator with the turbine. The only option to control the absorbed power in pumping mode is to use the hydraulic short circuit. In this mode, the synchronous machine operates as a motor driving the pump, and additional water is used to operate the turbine. Therefore, the total power consumption of the PSPP can be controlled. However, this mode of operation comes along with additional power loss.

The second arrangement consists of a pump-turbine and a motor-generator, see Figure 2.3. Again, the active power generation in turbine mode can be controlled by the water flow rate across the turbine. For the combined pump-turbine arrangement, the turbine mode and the pumping mode have different rotating directions. Therefore, additional equipment is needed to synchronize the motor-generator in pumping mode. Due to the fixed speed at directly line-connected operation, the active power is set to one specific value and cannot be controlled. One option to allow

for adjusting the active power with this arrangement is to utilize a larger number of smaller sized machines for a given PSPP. In this case, the absorbed active power in pumping mode can be adjusted in the form of discrete steps by starting up or shutting down a different number of machines.

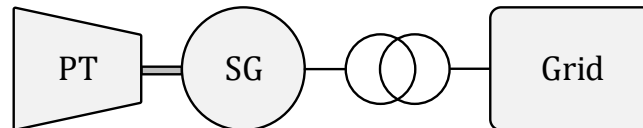


**Figure 2.3:** Block diagram of a PSPP utilizing a combined pump-turbine (PT = Pump-Turbine and SG = Synchronous Motor-Generator).

### 2.2.2 Start-Up Converter

The first use of a power converter in PSPPs was as a start-up converter [19] for the operation in pumping mode, see Figure 2.4. In this operation, the generator is accelerated to nominal speed with the power converter and then synchronized to the grid. After this process, the power converter is bypassed and the additional power loss of the power converter is removed for the steady-state operation of the motor-generator. Compared to power converter technologies nowadays, these first power converters had poor efficiencies and voltage waveforms which additionally stressed the motor-generator. However, due to the short times of operation with the power converter, these drawbacks were accepted. Such start-up converters are listed for up to 21 kV and 40 MW in [20].

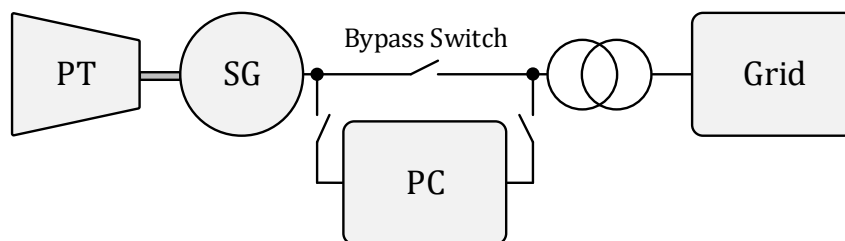


**Figure 2.4:** Block diagram of bypass operation of a PSPP (PT = Pump-Turbine, SG = Synchronous Motor-Generator, and PC = Power Converter).

### 2.2.3 Power Converter for Pumping Mode

The next step, which has been implemented in a few large PSPPs utilizing combined pump-turbines, was the use of a power converter for pumping mode only, see the presentation of the PSPPs Grimsel 2 and Forbach in the next Section. In this case, the power in the pumping mode can be widely controlled by simply adjusting the feeding frequency of the motor-generator. Also, the two different rotational directions for the use of a combined pump-turbine can be realized with this arrangement. For turbine mode, the converter is bypassed with a power switch, in which case the motor-generator operates directly on the grid.

Having the power converter bypassed provides two further advantages. Notably, it is possible to service the power converter while the directly line-connected synchronous machine is fully operating. Furthermore, the bypassed power converter can be used as a source or sink of reactive power [14].

### 2.2.4 Example Cases for Power Converter Operation

A few conventional hydropower plants (HPPs) have implemented a synchronous generator with a power converter. Three representative projects are described in this Section: “Grimsel 2,” which is currently the largest implemented project, “Forbach,” which is the oldest facility with a power converter for pumping mode in Germany which served as a prototype, and “Forte Buso,” which shows the excellent usability of variable-speed operation in turbine mode for a small HPP.

#### Grimsel 2

The PSPP Grimsel 2 in Switzerland [5], which was built between 1974 and 1980 [21], first operated four directly line-connected synchronous machines integrated in ternary machine sets. Then, the power in pumping mode was simply controlled by selecting the number of active units and utilizing the hydraulic short circuit to obtain intermediate power levels which reduced the total efficiency significantly. The power of the PSPP is  $4 \times 80$  MW in turbine operation, and  $4 \times 90$  MW in pumping operation. The average hydraulic head is 400 m and the water flow rate is  $4 \times 22$  m<sup>3</sup>/s. The synchronous speed of the motor-generators is 750 rpm.

In 2013, to react more efficiently to the current demands, one of the synchronous machines was equipped with a 100 MVA power converter with an active front-end

(see Section 5.3.5) and a bypass switch. Figure 2.5 shows the topology of the unit equipped with the power converter.

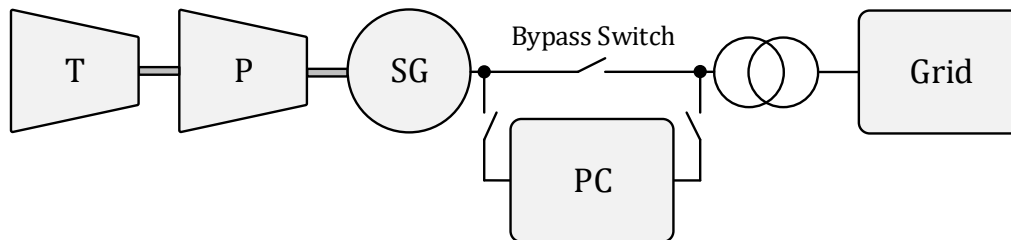


**Figure 2.5:** Block diagram of bypass operation of a PSPP utilizing a ternary machine set (T = Turbine, P = Pump, SG = Synchronous Motor-Generator, and PC = Power Converter).

At that time, this 100 MVA power converter was the most powerful realized voltage source converter (VSC) for a drive application.

The machine set equipped with the power converter can vary its power continuously between 60 MW and 100 MW. The possible operation modes are turbine mode, pumping mode without the power converter (fixed-speed), pumping mode with the power converter (variable-speed), and phase-angle correction using the power converter. Potential turbine operation with the power converter was not considered due to the relatively small variation of the hydraulic head.

As per [5], the power converter showed good usability already within the first 11 months of operation. During this time, it operated for 3500 h (which corresponds to 43.5% of the observed time) in controlled pumping mode and for 850 h (which corresponds to 10.6% of the observed time) in synchronous condenser mode (source or sink of reactive power).

### Forbach

The PSPP Forbach [22], which was built at the end of the 1920s, consists of two ternary machine sets. The total power of the PSPP in turbine mode is 43 MW, the total power in pumping mode is 20 MW. The pumps were shut down in the 1970s due to technical defects, and the power plant was only operated in turbine mode. The reactivation project, which was decided upon in 1988 and finished in 1993, was used to not only enable the 20 MW pumping mode again, but also to introduce

power converter operation of one of the motor-generators, which was 35 years old at that time. The HPP served as a prototype facility for testing a new dimension of converter-fed PSPPs. The idea was to retain as much of the electrical equipment as possible to keep the project costs low. Additionally, the machine should be able to also operate directly line-connected to keep the total efficiency high.

Figure 2.5 shows the topology of the unit equipped with the power converter. The single power converter operating one of the motor-generators of PSPP Forbach is a 21.3 MW current source converter.

The dynamic load on the pump and the hydraulic system is reduced by using the power converter when operation modes change. In particular, for pumping operation, the pump of the power converter operated ternary machine set is discharged and filled at a reduced rotational speed of 197 rpm, in contrast to the synchronous rotational speed of 500 rpm. Also, the converter operation allows the machine set to shut down via electrical braking, thereby recuperating the braking energy back into the grid. This approach is faster and less demanding on the system's mechanical structure than the conventional method of using braking nozzles at the turbine.

### **Forte Buso**

The HPP at Forte Buso [23] optimizes the plant's operating efficiency utilizing a power converter. The total efficiency of the small HPP has been increased by adjusting the turbine's rotational speed, depending on the actual hydraulic head of the reservoir. This small HPP was realized because of a new measure enacted by the Italian legislation that requires large HPPs to ensure minimum ecological flow at the foot of the dam. The dam was built in the early 1950s. The machine operating in the small HPP which was subsequently added went into operation in 2012. This small HPP was built so as to not waste the required water flow. The water flow rate varies depending on the season according to the guideline and the hydraulic head varies naturally depending on the season.

Table 2.1 shows the seasonal data for the hydraulic head  $H$  and the water flow rate  $Q$ . It also shows the design conditions for the turbine and therein, the significant difference between the minimum and maximum values. The nominal values for the final turbine design are  $Q_n = 549$  l/s and  $H_n = 102$  m. The Pelton-turbine is designed for a hydraulic power of 549 kW and a nominal speed of 600 rpm.

By adapting the turbine's rotational speed through operating the generator with

**Table 2.1:** Reference conditions for the HPP at Forte Buso. [23]

	Dec-Mar	Apr-Jul	Aug-Sep	Oct-Nov	Max	Min
$H$ in m	86.1	91.6	103.3	102	110	45
$Q$ in l/s	392	549	470	549	549	392

a power converter, the turbine efficiency at lower hydraulic heads was increased when compared with directly line-connected operation. It was even possible to obtain equal turbine efficiency at even lower hydraulic heads of up to  $H/H_n = 0.44$ .

An evaluation over a 10 month period showed that the variable-speed Pelton-turbine operation increases the HPP's efficiency on average by 11 % compared to fixed-speed turbine operation [23].

## 2.3 Doubly-Fed Induction Machine

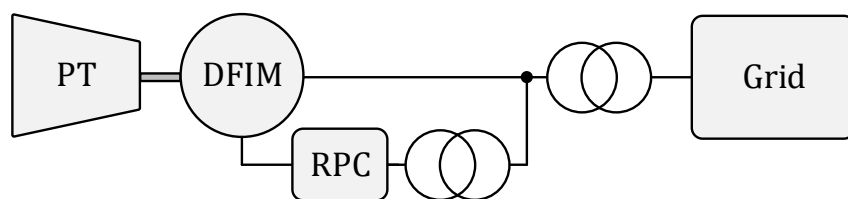


**Figure 2.6:** Block diagram of a DFIM for operation in a PSPP (PT = Pump-Turbine, DFIM = Doubly-Fed Induction Machine, and RPC = Rotor Power Converter).

The doubly-fed induction machine (DFIM) is state-of-the-art when it comes to variable-speed PSPPs, due to its high efficiency of about 98 % [24] and the low additional cost for the power converter compared with full-size converter (FSC) operation. The power converter of the DFIM is connected to the rotor, and is only rated for a fraction of typically less than 1/3 of the machine's rated power [3]. Figure 2.6 shows an exemplary schematic of a DFIM with a power converter for providing the rotor power. The maximum possible rotor power is limited due to the complex rotor construction which, in turn, reduces the range of variable-speed operation [5]. Because of the DFIM's low-start-up torque it is not possible to start the pump directly in water. Therefore, start-up requires the pump to be de-watered

before starting, and, in turn, increases the time required for the transition between the modes of operation [25]. The challenging behavior of the DFIM under fault condition, i.e., low-voltage ride through (LVRT), has been well described in [4] and in [26] and might pave the way for FSC operated synchronous machines in the future as well.

Two of the four pump-turbines of PSPP Goldisthal [27] are equipped with a DFIM with a generative power capability of 340 MVA each. A cyclo-converter with a power rating of 100 MVA allows for the speed to be adjusted by -10 % to +4 % of the rated speed. This translates into a power range of 190 MW to 290 MW in pumping mode [28].

The two 433 MVA DFIMs operating in PSPP Frades II [29] form the largest variable-speed PSPP in Europe. The DFIMs' rotors are equipped with VSCs with a rated power of 82 MVA each. The hydraulic head of the PSPP is 420 m, and the water flow rate per machine is 100 m<sup>3</sup>/s. With a speed range of 350 rpm to 380 rpm in pumping mode, the active power consumption of each machine can be varied between 304 MW and 390 MW. The power in turbine mode can be controlled between 25 % and 100 % of the nominal load by adjusting the water flow rate across the turbine. For this mode of operation, it is possible to adjust the rotational speed slightly to achieve higher efficiency at certain operating points compared to operation at fixed speed.

## 2.4 Full-Size Converter Operated Electrically Excited Salient-Pole Synchronous Machine



**Figure 2.7:** Block diagram of full-size converter operation of a synchronous generator in a PSPP (PT = Pump-Turbine, SG = Synchronous Motor-Generator, and FSC = Full-Size Converter).

Figure 2.7 shows the block diagram for the full-size converter (FSC) operation of a large PSPP. During operation, all power produced or absorbed by the motor-

generator needs to pass through the power converter which is why it is referred to as FSC. Especially when compared with the DFIM, the FSC operated synchronous generator offers advantages such as large speed range, pump start-up directly in water (fast response), as well as compliance with the latest grid requirements concerning LVRT [4]. Depending on the choice of power converter topology, the FSC offers a reactive power capability even at standstill as well as a built-in fault tolerance concerning the semiconductor power switches due to redundancy, which is an important feature.

When compared with the synchronous motor-generator's directly line-connected operation, FSC operation comes with additional investment cost, additional power loss, and additional complexity, as well as increased space requirements. The higher flexibility of the whole system must compensate for these drawbacks. Other problems that occur at FSC operation are additional voltage stress of the winding insulation as well as additional power loss due to the harmonic content of the voltage waveforms. These aspects are investigated in Chapters 5 - 8.

The 100 MVA power converter operated synchronous motor-generator at PSPP Grimsel 2 is still considered the largest implemented FSC project, although the power converter is bypassed during turbine operation, see Section 2.2.4. Reference [30] shows that mid-sized pump-turbines with FSC operated synchronous motor-generators are readily available up to a power rating of 50 MW.

## **2.5 Economic Considerations**

Renewable energy sources like wind and solar require energy storage technologies to compensate for their volatile energy generation. In addition, due to the high energy production of solar power plants, particularly at noon, the span between peak and base energy prices has become smaller. Therefore, the conventional operation strategy of PSPPs utilizing this price span leads to fewer earnings [6].

The economic benefits of upgrading fixed-speed PSPPs to variable-speed PSPPs have recently been studied: Reference [7] computes the achievable earnings for fixed-speed (line-connected pump-turbine, ternary machine set, and ternary machine set utilizing hydraulic short circuit) and variable-speed technologies (FSC operated synchronous motor-generator and DFIM) in PSPPs considering the Austrian-German spot market and the Austrian balancing market. It shows that the main parameter for increasing earnings is the achievable operating range of the PSPP to effectively

participate in the balancing energy market, and that the FSC operated synchronous motor-generator offers the highest flexibility for the operation of pump-turbines.

Reference [31] analyzes the benefits of upgrading from fixed-speed to variable-speed technology for the PSPP Grimsel 2 in Switzerland and considers FSC operated synchronous motor-generators as well as DFIMs. This case study shows that the benefit of the variable-speed upgrade for participation of the power plant in the energy market only leads to an increase of earnings of only 4%. By participating in energy markets and balancing energy markets, earnings can be increased by 58% when utilizing variable-speed technologies (FSC operated synchronous motor-generator or DFIM) compared to the fixed-speed operation.

In summary, providing balancing energy can significantly increase the earnings of PSPPs. This is not possible for directly line-connected synchronous motor-generators operating at fixed-speed without utilizing the hydraulic short-circuit. For participation in the balancing energy market without the hydraulic short-circuit, a highly flexible variable-speed technology is required. The FSC operated synchronous motor-generator is well suited for this application.

The FSC topology comes at the price of the additional investment cost for the FSC. As [32] shows, the FSC topology increases the total cost of the power plant by 12% when compared to a conventional fixed-speed pump-turbine arrangement. Therefore, the presented cost reduction of the motor-generator alone (see Section 4.7) cannot compensate for the additional investment cost for the FSC topology, because the cost for the motor-generator is only a fraction of the cost of the total power plant. Providing balancing energy would require a hydraulic short-circuit when utilizing a fixed-speed arrangement. According to [32], a PSPP utilizing a hydraulic short-circuit would have approximately the same total investment cost as the FSC operated synchronous motor-generator due to the additional costs for the water way and the hydraulic equipment while having a round-trip efficiency (considering both turbine and pumping mode) of 42% compared to the round-trip efficiency of 74% of the FSC topology.



# Chapter 3

## Generator Design for Full-Size Converter Operation - Design Techniques

*This Chapter reviews the conventional design process for electrically excited salient-pole synchronous motor-generators for application in large pumped storage power plants and identifies the shortcomings related to this approach when applied to designs for operating frequencies other than 50 Hz. It also demonstrates the additional aspects and possibilities of the motor-generator design due to the full-size converter operation. Furthermore, this Chapter presents the generator design and optimization approach that has been developed for designs over a large range of design frequencies.<sup>1</sup>*

### 3.1 Generator Design Approach for Conventional Directly Line-Connected Operation

The conventional hydropower synchronous generator design process is based on the apparent power  $S$ , the mechanical speed  $n$ , as well as the mass moment of inertia  $J$ , which is a requirement of the turbine to reduce temporary over-speed and turbine runaway. A large mass moment of inertia allows appropriately compensating load fluctuations in the grid. As per [12], the main dimensions of a large hydropower synchronous machine are chosen as follows:

---

<sup>1</sup>Selected material of this Chapter has also been published in [33] and [34].

First, the stator inside diameter  $d$  (air-gap diameter) is determined as

$$d = \sqrt{\frac{C \cdot J \cdot n}{k_j \cdot S}}, \quad (3.1)$$

where  $C$  is the Esson utilization coefficient that quantifies the electromagnetic utilization. On the one hand, it is limited by the stator and rotor core saturation (that limit the air-gap flux density). On the other hand, it is also restricted by the cooling capability of the machine (that limits the maximum possible linear current density), which is a function of the utilized cooling system. Typical values for the utilization can be found for common operating frequencies (50 Hz and 60 Hz) based on built machines, i.e.,  $C$  is between  $5 \text{ kVA} \cdot \text{min}/\text{m}^3$  and  $8 \text{ kVA} \cdot \text{min}/\text{m}^3$  for a 150 MVA, 50 Hz, 200 rpm synchronous machine utilizing air-cooling [35]. The parameter  $k_j$  is a design-dependent coefficient that considers the structure of the rotor and is only available for common operating frequencies (50 Hz and 60 Hz) [12]. The relationship between  $J$ ,  $k_j$ ,  $d$ , and the total axial length of the machine  $l$  is given by

$$J = k_j \cdot d^4 \cdot l, \quad (3.2)$$

and illustrates the strong influence of the stator inside diameter  $d$  on the mass moment of inertia  $J$ . From these parameters, the total axial length  $l$  is derived:

$$l = \frac{S}{C \cdot n \cdot d^2}. \quad (3.3)$$

In contrast to this approach, the synchronous machine design in [36] is realized via the air-gap shear stress and typical values for  $l/d$ , while [35] and [37] utilize typical values for  $l/\tau_p$ . However, as stated, the important parameter for hydropower generators is the mass moment of inertia which results from the rotor construction, and is therefore hard to predict during the rough design process. Hence, utilizing (3.1) initially results in machine designs closer to the desired mass moment of inertia. However, this approach cannot be applied when designing synchronous motor-generators for a wide range of design frequencies. Therefore, the approach developed in this thesis and presented in Section 3.2 is used to compute the generator designs for full-size converter (FSC) operation presented in Chapter 4.

## 3.2 Generator Design Approach for Full-Size Converter Operation

Compared with directly line-connected operation, the synchronous machine, when operated by an FSC, operates in an island situation, and the FSC takes on some of the requirements for the conventional synchronous motor-generator. Notably, the FSC regulates the active power  $P$  (which, of course, the turbine must provide) and reactive power  $Q$  exchanged with the grid [10]. The motor-generator's electrical frequency  $f$  is no longer fixed at a certain value (e.g., 50 Hz or 60 Hz) and can be chosen for the optimization of the machine design [38].

The main advantage of the FSC operated synchronous machine is the active power control in pumping mode due to the variable-speed operation. For further efficiency improvement, the turbine control can choose the best suited rotational speed for the currently transferred power, the hydraulic head, and the discharge [3]. Therefore, the turbine and pump of such an FSC operated motor-generator can operate at a certain band of rotational speeds rather than at a single line-synchronous rotational speed. Hence, the machines operate at partial load more often in comparison to a conventional directly line-connected PSPP.

Another major advantage of the FSC operation for the motor-generator design is that the machine no longer needs to provide reactive power to the grid, as this part is taken over by the FSC [14]. This results in a smaller and lighter generator design for a given power plant. Low voltage events on the grid side (including short circuits) mainly translate to the machine as a load rejection behind the FSC. The motor-generator and turbine accelerate corresponding to their mass moments of inertia, which translates into certain requirements for the generator's minimum inertia.

Since values for  $k_j$  in (3.1) and (3.2) have only been established for grid frequency operation (50 Hz and 60 Hz), the developed design approach follows the idea of minimizing the cost function (3.34) given in Section 3.2.2. This includes the material costs of the generator as well as the costs of the power loss during operation, while not violating any constraints on the mechanical stability of the construction (which, for instance, limits the lowest possible design frequency) and while maintaining the required mass moment of inertia.

### 3.2.1 Electrically Excited Salient-Pole Synchronous Machine

#### Design Process

This Section presents the conventional design equations for electrically excited salient-pole synchronous motor-generators used to also create the generator designs for FSC operation. In contrast to the design for conventional directly line-connected operation, the additional degrees of freedom for the generator design at FSC operation, i.e., the free choice of the design frequency and the power factor, are utilized.

#### Design Specifications

The design specification for the generator design process include the apparent power  $S$ , the power factor  $\cos \varphi$ , the stator phase voltage  $U_{\text{ph}}$ , the number of phases  $m$ , the rotational speed  $n$ , the design frequency  $f$ , as well as the Esson utilization coefficient  $C$ .

#### Main Dimensions

Utilizing an initially chosen stator inside diameter  $d$ , the total axial length  $l$  is derived [12]:

$$l = \frac{S}{C \cdot n \cdot d^2}. \quad (3.4)$$

The number of pole-pairs  $p$  is related to  $f$  and  $n$  according to

$$p = \frac{f}{n} \quad (3.5)$$

and leads to the pole-pitch  $\tau_p$  as follows:

$$\tau_p = \frac{d \cdot \pi}{2 \cdot p}. \quad (3.6)$$

#### Stator Winding

Utilizing an initially chosen fundamental air-gap flux density  $B_{\delta 1}$  (typically between 0.8 T and 1.05 T [35]), the fundamental air-gap flux  $\phi_{\delta 1}$  can be computed:

$$\phi_{\delta 1} = \frac{2}{\pi} \cdot B_{\delta 1} \cdot l \cdot \tau_p. \quad (3.7)$$

Assuming an initial winding factor  $k_{w1}$  (typically 0.92 [36]), the number of phase winding turns  $w_{ph}$  results from:

$$w_{ph} = \frac{U_{ph}}{\sqrt{2} \cdot \pi \cdot f \cdot k_{w1} \cdot \phi_{\delta 1}}. \quad (3.8)$$

Large hydropower generators utilize a two-layer Roebel bar winding, and, therefore, the number of conductors per slot is  $z_s = 2$ . The number of parallel paths  $a$  is chosen to obtain a proper slot-pitch (typically around 70 mm for this type of machine [35]). The relation between these quantities is

$$q = \frac{w_{ph} \cdot a}{z_s \cdot p}. \quad (3.9)$$

Next, the number of stator slots  $Q_s$  can be computed using

$$Q_s = 2 \cdot p \cdot q \cdot m, \quad (3.10)$$

and the slot-pitch  $\tau_s$  results from

$$\tau_s = \frac{d \cdot \pi}{Q_s}. \quad (3.11)$$

With a coil pitch  $y$  for sufficiently suppressing the 5th and 7th order harmonics, which needs to be evaluated for each individual design, the winding factor  $k_w$  can be calculated for each harmonic order  $\nu$  [39]:

$$k_{w\nu} = \frac{\sin\left(\frac{\nu\pi}{2m}\right)}{q \cdot \sin\left(\frac{\nu\pi}{2mq}\right)} \cdot \sin\left(\frac{y}{\tau_p} \cdot \frac{\nu\pi}{2}\right). \quad (3.12)$$

Note that for (3.12)  $\tau_p$  is an integer describing the number of slots within one pole-pitch. Having computed the actual winding factor  $k_{w1}$ , the fundamental air-gap flux  $\phi_{\delta 1}$  and the air-gap flux density  $B_{\delta 1}$  need to be corrected accordingly.

#### Slot Geometry, Conductors, and Insulation

The phase current  $I_{ph}$  can be calculated with

$$I_{ph} = \frac{S}{m \cdot U_{ph}} \quad (3.13)$$

which results in the machine's linear current density  $A$  [39]:

$$A = \frac{2 \cdot m \cdot w_{ph} \cdot I_{ph}}{2 \cdot p \cdot \tau_p}. \quad (3.14)$$

$A$  is restricted by the cooling capability of the utilized cooling technology and is typically limited at 120 A/mm for air-cooled machines [35]. The required copper cross section for the stator winding  $A_{\text{cu}}$  can be calculated using a typical current density  $J_{\text{cu}}$  (between 3 A/mm<sup>2</sup> and 7 A/mm<sup>2</sup> [35]) for this type of machine:

$$A_{\text{cu}} = \frac{I_{\text{ph}}}{a \cdot J_{\text{cu}}}. \quad (3.15)$$

With  $z_s$  conductors per slot, the cross section of the stator slot  $A_s$  can be computed via a typical slot fill factor for a high-voltage winding for this type of machine of  $\varphi_s = 0.5$  [35]:

$$A_s = \frac{A_{\text{cu}} \cdot z_s}{\varphi_s}. \quad (3.16)$$

With a given slot height to slot width ratio for the stator slots  $h_s/w_s$ , the slot geometry can be derived from

$$A_s = h_s \cdot w_s. \quad (3.17)$$

Assuming the conductors' geometry within the slots follows the same ratio as the slot geometry, which is a simplified approach, the conductor geometry can be computed with

$$w_{\text{cu}} = \sqrt{\frac{z_s \cdot A_{\text{cu}}}{\frac{h_s}{w_s}}} \quad (3.18)$$

and

$$h_{\text{cu}} = w_{\text{cu}} \cdot \frac{h_s}{w_s}. \quad (3.19)$$

To reduce the stator winding's load dependent power loss to an acceptable level, the conductor needs to be subdivided into a number of strands to form a Roebel bar, with a number of strands arranged side by side in the slot,  $a_x$ , and a number of strands stacked on top of each other,  $a_y$ . This results in a total number of subconductors  $a_{\text{sc}} = a_x \cdot a_y$  per conductor.

### Air-Gap Length, Reactances, and Excitation Demand

A typical upper limit for the synchronous reactance  $x_d$  for this type of machine is  $x_d = 1.2$  pu [11]. The relation between the synchronous reactance  $x_d$ , the magnetizing reactance  $x_h$ , and the leakage reactance of the stator winding  $x_\sigma$  is

$$x_d = x_\sigma + x_h. \quad (3.20)$$

The equivalent air-gap length  $\delta'$  can be computed utilizing the pole field factor  $\beta$  for the utilized rotor pole geometry [39]:

$$\delta' = \frac{4}{\pi} \cdot m \cdot \mu_0 \cdot f \cdot w_{\text{ph}}^2 \cdot k_{\text{w1}}^2 \cdot \frac{l \cdot \tau_p \cdot \beta}{p \cdot X_h}. \quad (3.21)$$

This equivalent air-gap length  $\delta'$  includes the geometrical air-gap, the openings of the slots and the cooling ducts, and the magnetomotive force (mmf) drop in the iron due to saturation effects. The geometrical air-gap length  $\delta$  is assumed to be responsible for 70 % of the total mmf drop [36], and, therefore

$$\delta = 0.7 \cdot \delta'. \quad (3.22)$$

Note that due to mechanical constraints, a minimum air-gap length is required and hence, a mechanical air-gap length of less than 10 mm is not realistic for large hydropower generators.

With the voltage drop at the leakage reactance  $U_\sigma$

$$U_\sigma = X_\sigma \cdot I_{\text{ph}}, \quad (3.23)$$

the internal voltage  $U_h$  is derived via the geometric sum, see Figure 3.1, as follows:

$$U_h = \sqrt{U_{\text{ph}}^2 + U_\sigma^2 - 2 \cdot U_{\text{ph}} \cdot U_\sigma \cdot \cos\left(\frac{3\pi}{2} - \varphi\right)}. \quad (3.24)$$

The corresponding main flux at load  $\phi_h$  results from

$$\phi_h = \phi_{\delta 1} \cdot \frac{U_h}{U_{\text{ph}}}. \quad (3.25)$$

The overall mmf  $\Theta_m$  and the stator winding mmf  $\Theta_s$  can be computed as follows [36]:

$$\Theta_h = \frac{\delta' \cdot B_{\delta 1}}{\mu_0} \cdot \frac{U_h}{U_{\text{ph}}} \quad (3.26)$$

and

$$\Theta_s = \frac{\sqrt{2}}{\pi} \cdot m \cdot z_s \cdot q \cdot k_w \cdot \frac{I_{\text{ph}}}{a}. \quad (3.27)$$

The required rotor winding mmf  $\Theta_f$  results from the geometric sum of these two quantities, see Figure 3.1:

$$\Theta_f = \Theta_m - \Theta_s. \quad (3.28)$$

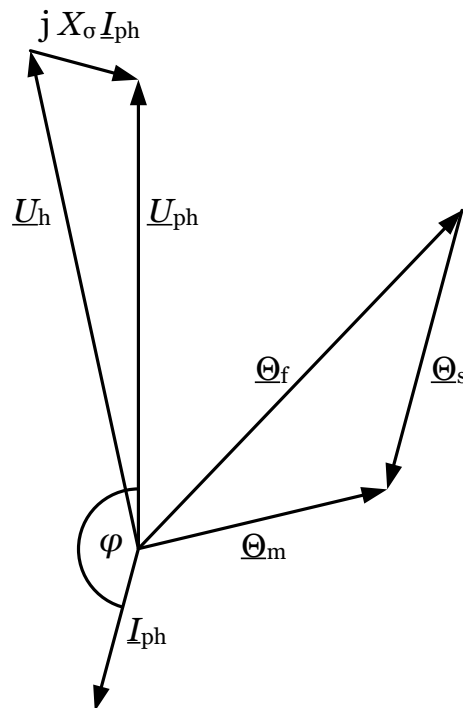


**Figure 3.1:** Phasor diagram of the synchronous machine for over-excited generator operation including the mmf relations.

### Stator Geometry Calculation

Assuming a typical stator yoke flux density  $B_{y,s}$  between 1 T and 1.45 T [35] and an iron fill factor  $k_{fe}$ , the stator yoke height  $h_{y,s}$  can be computed

$$h_{y,s} = \frac{\phi_h}{2 \cdot B_{y,s} \cdot l \cdot k_{fe}} \quad (3.29)$$

which results in the stator outside diameter  $d_o$  of

$$d_o = d + 2 \cdot h_s + 2 \cdot h_{y,s}. \quad (3.30)$$

From these parameters, the inner machine volume  $V_i$  as well as the total construction volume  $V$  can be computed:

$$V_i = \frac{d^2 \cdot \pi}{4} \cdot l \quad (3.31)$$

and

$$V = \frac{d_o^2 \cdot \pi}{4} \cdot l. \quad (3.32)$$

### Rotor Geometry Design

Analyzing the generator dimensions used in simulations of four high-power hydropower generators with power ratings between 50 MVA and 500 MVA, as published in [11, 15, 40, 41], typical values for the parameter ratios of the rotor pole dimensions are derived. Figure 3.2 illustrates the parameters of interest, and Table 3.1 shows the value ranges for the relations describing the rotor pole geometry.

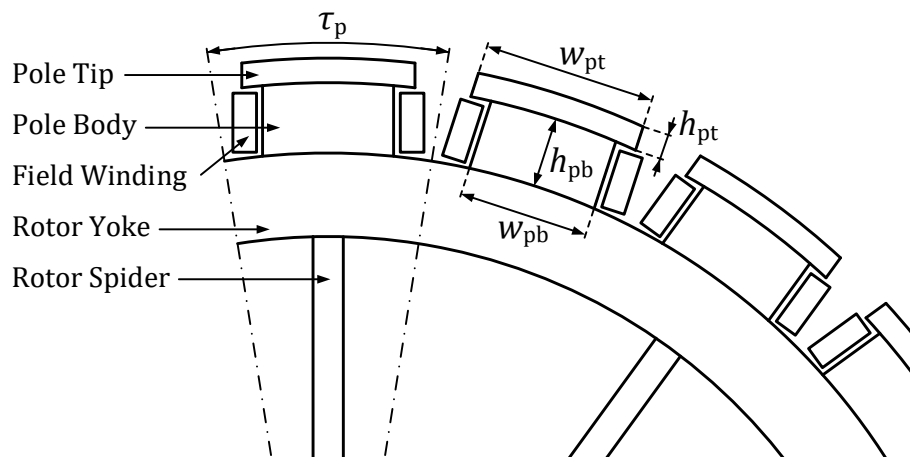


**Figure 3.2:** Pole construction and parameters of interest.

Parameter ratio	$w_{pt}/\tau_p$	$w_{pb}/w_{pt}$	$h_{pt}/w_{pt}$	$h_{pb}/\tau_p$
Value range	0.69 - 0.76	0.67 - 0.73	0.13 - 0.15	0.20 - 0.32

**Table 3.1:** Value ranges for the parameter ratios describing the rotor pole geometry.

### Power Loss Distribution

Based on a simplified model, the total power loss  $P_{total}$  comprises the load dependent power loss  $P_{load}$ , the stator iron power loss  $P_{fe}$ , as well as the mechanical power loss  $P_{mech}$ :

$$P_{total} = P_{load} + P_{fe} + P_{mech}. \quad (3.33)$$

The load dependent power loss  $P_{load}$  comprises the resistive power loss in the stator winding, the additional power loss in the Roebel bars, the power loss due to

skin effect, and the field winding power loss. The stator iron power loss  $P_{fe}$  consists of hysteresis and eddy current losses which are computed by using the Steinmetz equation. The total mechanical power loss  $P_{mech}$  comprises the bearing friction and the windage losses. The damper winding power loss as well as the pole shoe surface power loss are not taken into account. This simplified model is utilized to identify the relationship between the losses of the different loss components and the generator design for FSC operation. More details of the computation of the individual power losses are provided in Appendix A.

It is assumed that the additional power loss due to the non-ideal power supply of the FSC can be neglected when utilizing a multilevel power converter topology with a high number of levels. Use of such an extremely high number of levels is considered necessary considering the investigated voltage and power rating, see Chapter 5.

### **Generator Mass, Mass Moment of Inertia, and Mechanical Strength**

For the cost evaluation presented in Section 3.2.2, the masses of the active materials of the synchronous generator are required. These include the copper masses of the stator winding and the field winding as well as the masses of the electric steel of the stator and the rotor. In addition, to calculate the rotor's mass moment of inertia, the masses of the rotor spider and the shaft are computed as well. The rotor construction's mechanical stability for standstill, nominal-speed, as well as runaway-speed is calculated using the approach presented in [42].

### **3.2.2 Optimization Process**

The optimization algorithm minimizes the total cost function (3.34) using the cost factors presented in this Section. The optimization algorithm is linked to the generator design process presented in Section 3.2.1. The generators are designed and optimized automatically utilizing an evolutionary algorithm for each individual design frequency investigated. The optimization algorithm can vary the stator inside diameter  $d$  which transfers directly to the total axial length  $l$  via (3.3) via Esson's utilization coefficient  $C$ . The initial air-gap flux density  $B_{\delta 1}$  can be chosen by the optimization algorithm and is used as a starting point for designing the winding. Also, the different options for the winding design, namely the number of parallel paths and the configuration of the fractional slot winding, are investigated extensively

within the generator design process. The rotor's geometry is computed from typical relations for salient-pole hydropower generators, see Section 3.2.1. The desired mass moment of inertia  $J$ , which is an important requirement for hydropower generators, see Section 3.1, is a constraint during the optimization process. It can be obtained by adjusting  $d$  and the cross section of the rotor yoke  $A_{y,r}$ , which is the last optimization variable. The other main constraints include the flux density at the smallest cross section of the stator teeth, the maximum allowed current in the conductors, as well as the mechanical stress on the rotor construction.

The parameters used in the optimization process, i.e., the design specifications, the optimization variables, the initial values, and the optimization constraints, are summarized in the following. The initial values and the bounds of the constraint variables have been chosen from literature and experience.

### Design Specifications

$S$	...	Apparent power
$\cos \varphi$	...	Power factor
$U_{\text{ph}}$	...	Stator phase voltage
$m$	...	Number of phases
$n$	...	Rotational speed
$f$	...	Design frequency

### Optimization Variables

$d$	...	Stator inside diameter
$B_{\delta 1}$	...	Fundamental design air-gap flux density
$A_{y,r}$	...	Cross section of the rotor yoke ( $h_{y,r} \cdot l$ )

### Optimization Constraints

$J$	...	Required mass moment of inertia
$A_{\max}$	...	Maximum allowed linear current density of the stator winding
$B_{t,\max}$	...	Maximum allowed flux density at the smallest cross section of the stator teeth
$v_{\max}$	...	Maximum allowed circumferential speed of the rotor
$\sigma_{\max}$	...	Maximum allowed mechanical stress on the utilized materials of the rotor construction
$\tau_{p,\max}$	...	Maximum allowed pole-pitch to ensure mechanical feasibility of the rotor poles (based on built machines)

### Cost Evaluation and Target Function

The cost of the different generator designs is calculated using the costs for the following active parts: stator iron  $C_{fe,s}$ , rotor iron  $C_{fe,r}$ , and copper  $C_{cu}$ . In addition, the costs for the load dependent power losses  $C_{load}$  as well as the costs for the constant power losses (load independent power losses)  $C_{const}$  during operation are taken into account, as presented in [11]:

$$C_{fe,s} = 4 \text{ EUR/kg}; C_{fe,r} = 6 \text{ EUR/kg}; C_{cu} = 11 \text{ EUR/kg};$$

$$C_{load} = 2000 \text{ EUR/kW}; C_{const} = 3000 \text{ EUR/kW};$$

The optimization algorithm minimizes the synchronous generator's total cost  $C_{total}$  using the following equation:

$$C_{total} = m_{fe,s} C_{fe,s} + m_{fe,r} C_{fe,r} + (m_{cu,s} + m_{cu,r}) C_{cu} + P_{load} C_{load} + (P_{fe} + P_{mech}) C_{const}, \quad (3.34)$$

where  $m_{fe,s}$  is the stator iron mass (stator core),  $m_{fe,r}$  is the rotor iron mass (rotor poles and yoke),  $m_{cu,s}$  is the stator copper mass, and  $m_{cu,r}$  is the rotor copper mass. The load dependent power loss  $P_{load}$  is rated using the power loss evaluation cost factor for load dependent power losses  $C_{load}$ , while the stator iron power loss  $P_{fe}$  and the mechanical power loss  $P_{mech}$  are rated using the power loss evaluation cost factor for constant power losses (load independent power losses)  $C_{const}$ .

The total cost of the various generator designs presented in Section 4 are mainly computed for operation at nominal load with fixed-speed. In addition, Section 4.3 shows the total cost of the generator designs when considering a load profile which represents the operational behavior of the PSPP, including nominal and partial load turbine operation with fixed-speed as well as nominal and partial load pump operation utilizing variable-speed.

Note that due to the motor-generator's variable-speed operation in large PSPPs, not only does the stator current change depending on the operating point, but the rotational speed does likewise, and therefore, the electrical frequency as well. Although in reality, the iron power loss as well as the mechanical power loss change with the load, which is also included in the computational results presented in Section 4.3, the techniques defined by the standard [43] are used to evaluate these losses with the power loss evaluation cost factors for constant power loss.

The cost analysis considers both the initial cost, i.e., the material cost, and the cost for the power loss occurring during operation to allow for a direct comparison of various generator designs.

The additional investment cost for the FSC as well as a profitability analysis of the PSPP are not covered in this analysis. Reference [32] provides a cost comparison of PSPPs utilizing fixed-speed and variable-speed technologies, including costs for the entire power plant. References [7] and [31] analyze the economic perspective of various pumped storage power schemes. An excerpt of the results presented in these studies can be found in Section 2.5.

Utilizing the generator design optimization process presented in this Chapter in combination with the additional aspects and degrees of freedom at FSC operation, which are identified in Chapters 1 and 4, it is possible to reduce the synchronous motor-generator's total cost by 18% compared to a machine design for conventional directly line-connected operation, see Section 4.7.



# Chapter 4

## Generator Design for Full-Size Converter Operation - Computational Results

*This Chapter presents the computational results for various electrically excited salient-pole generator designs utilizing the generator design and optimization approach presented in Section 3.2. First, operation at unity power factor, as possible at full-size converter operation, is investigated. Next, the optimum design frequency is determined, in which the influence of the rotational speed, the Esson utilization coefficient, as well as the cost factors on the synchronous generator designs are analyzed. Then, this Chapter discusses the influence of the partial load profile on the generator design, the requirements for the synchronous reactance, as well as the power factor of the synchronous generator. At the end, this Chapter presents the suggested newly identified generator design for full-size converter operation.<sup>1</sup>*

### 4.1 Example Case for Operation at Unity Power Factor

This Section investigates how the machine design is influenced by operating at unity power factor ( $\cos \varphi = 1$ ), as is possible at full-size converter (FSC) operation (considering an AC-DC-AC voltage-source converter arrangement). Table 4.1 shows the differences between a conventional 150 MVA, 50 Hz, 200 rpm motor-generator operated at a power factor  $\cos \varphi = 0.9$  and the design of a motor-generator designed for active power only. Table 4.2 shows the different design values for the two designs in relation to the reference design, which is the unity power factor design and is used for comparison throughout this Chapter.

<sup>1</sup>Selected material of this Chapter has also been published in [33] and [34].

**Table 4.1:** Comparison of a conventional motor-generator design and the design for unity power factor (absolute values).

Motor-generator design	Conventional design	Unity power factor design
$S$ in MVA	150	135
$U_{ph}$ in kV	7.8	7.8
$\cos \varphi$	0.90	1.00
$f$ in Hz	50	50
$n$ in rpm	200	200
$d$ in m	7.4	7.5
$l$ in m	1.6	1.4
$V$ in $m^3$	84	75
$V_i$ in $m^3$	69	62
$m_s$ in t	88	81
$m_r$ in t	253	221
$\eta$ in %	98.87	99.09
Cost in $10^6$ EUR	5.52	4.67

**Table 4.2:** Comparison of a conventional motor-generator design and the design for unity power factor (relative values compared to the unity power factor reference design).

Motor-generator design	Conventional design	Unity power factor design
$S$ in MVA	150	135
$P$ in MW	135	135
$Q$ in Mvar	65	0
$\cos \varphi$	0.90	1.00
$f$ in Hz	50	50
$V$ in pu	1.11	1.00
$V_i$ in pu	1.11	1.00
$m_s$ in pu	1.09	1.00
$m_r$ in pu	1.14	1.00
$\eta$ in %	98.87	99.09
Cost in $10^6$ EUR	5.52	4.67

### Volume and Mass

The unity power factor design shows a significant reduction of the inner machine volume  $V_i$  and the total construction volume  $V$  of 10 %, and, correspondingly, also of the stator mass  $m_s$  and the rotor mass  $m_r$ .

### Efficiency

Even with this reduction in mass and therefore material cost, the computed efficiency increases by 0.22 percentage points, which is very beneficial for large hydropower plants and helps to compensate for the FSC's additional power loss. Note that only fixed-speed nominal load operation is considered in this Section.

### Cost

The total costs of the generator designs, which comprise both the costs for material as well as the costs for power loss during operation, are computed using (3.34) and the cost factors presented in Section 3.2.2. Compared to the directly line-connected  $\cos \varphi = 0.9$  generator design, the  $\cos \varphi = 1$  design for FSC operation shows a cost reduction of 15.4 %.

In the following, this unity power factor design for operation at 50 Hz  $\cos \varphi = 1$  is used as the reference design.

## 4.2 Optimum Design Frequency

### 4.2.1 Example Case for Design Frequencies Different than 50 Hz

This Section investigates the influence of the design frequency on the generator design. The free choice of the design frequency is possible due to the decoupling of the synchronous machine via the FSC from the grid. Figure 4.1 compares the volumes, masses, efficiencies, and the total costs of unity power factor designs for design frequencies between 30 Hz and 140 Hz and their conventional 50 Hz  $\cos \varphi = 0.9$  counterpart.

All the designs operate at the same machine utilization, have identical inner machine volumes and start-up time constants.

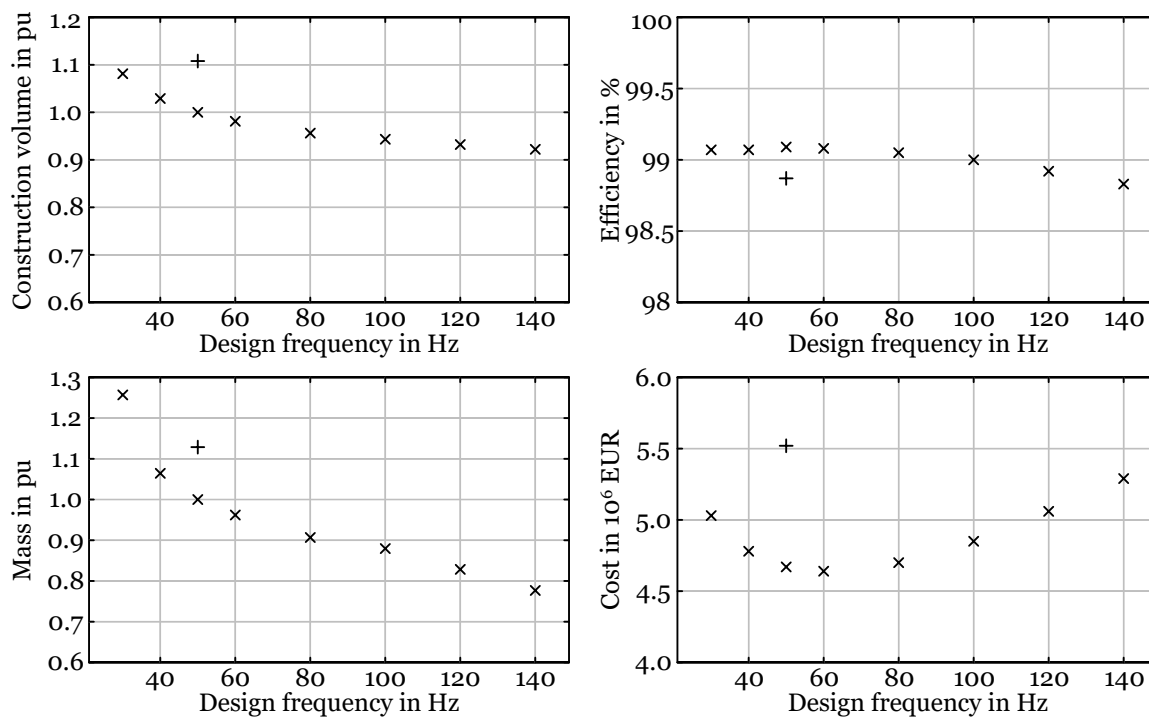


**Figure 4.1:** Construction volume, total mass, efficiency, and cost of the conventional design and the unity power factor designs for various design frequencies; + = conventional design for 50 Hz  $\cos \varphi = 0.9$ ,  $\times$  = designs for operation at  $\cos \varphi = 1$ .

### Volume and Mass

The construction volume decreases with higher design frequencies, as is commonly known for machines used in industrial and traction applications, at much smaller powers. For constant speed, as it is the case in the application investigated here, such a design has a higher number of poles and hence reduced stator yoke height due to the reduced air-gap flux. However, for this type of large synchronous machine, the savings in machine masses are significantly less when compared to much smaller power machines. This is due to the required mass moment of inertia and the mechanical stability of the rotor construction. The rotor has a much larger impact on the total mass compared to the stator, see Figure 4.2. In addition, for higher design frequencies, the rotor shows a smaller mass reduction than the stator.

While the masses of the investigated machine designs for design frequencies between 30 Hz and 140 Hz vary in a range from +25.7% to -22.3% compared to the reference design for 50 Hz, the construction volumes vary in a more narrow band from +8.1% to -7.8%, see Figure 4.1.

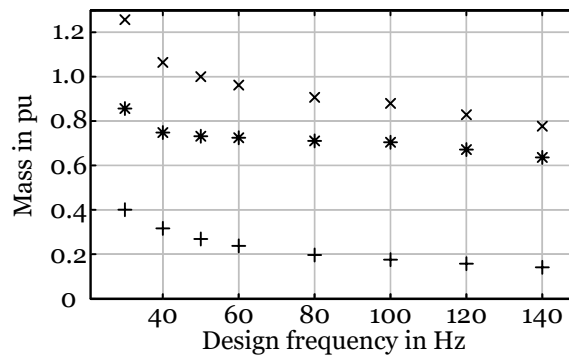


**Figure 4.2:** Mass distribution of the unity power factor designs for various design frequencies;  $\times$  = total mass,  $+$  = stator mass,  $*$  = rotor mass.

### Efficiency

The efficiency of the unity power factor synchronous generator designs is highest for design frequencies around 50 Hz. Particularly for higher design frequencies, the stator iron power loss becomes quite dominant (see Appendix B), thus reducing the efficiency.

The efficiencies of the investigated machine designs for design frequencies between 30 Hz and 140 Hz vary, ranging from 98.83 % to 99.09 %. The 50 Hz design has the highest efficiency.

### Cost

The total costs of the various generator designs are computed using (3.34) and the cost factors presented in Section 3.2.2. Figure 4.1 shows the curve's optimum (minimum total cost) for the 60 Hz design. This highlights the significant role of the operating costs over the course of a generator's lifetime when compared to only the material costs. For higher design frequencies, the construction material cost is significantly reduced. However, since the costs for power losses are considerably high for large hydro generators [11], the presented cost minimized designs with a high design frequency are of less interest because of their reduced efficiencies. For more details on the distribution of the costs see Appendix B.

The 60 Hz machine design results in the minimum cost for this analysis, and is 0.64 % cheaper than the reference design for 50 Hz. The most expensive design is the 140 Hz design, representing the highest investigated design frequency. The costs are 13.3 % higher than the reference design for 50 Hz.

### 4.2.2 Influence of the Rotational Speed

The generators presented in Sections 4.1 and 4.2.1 are designed for a rotational speed of 200 rpm. Figure 4.1 shows that the optimum design frequency for this specific parameter set would be 60 Hz. This Section discusses the influence of the rotational speed on the optimum design frequency. Figure 4.3 shows the construction volumes, the total masses, the efficiencies, and the total costs of unity power factor generator designs at various design frequencies for different rotational speeds, namely 100 rpm, 200 rpm, and 400 rpm.<sup>2</sup>

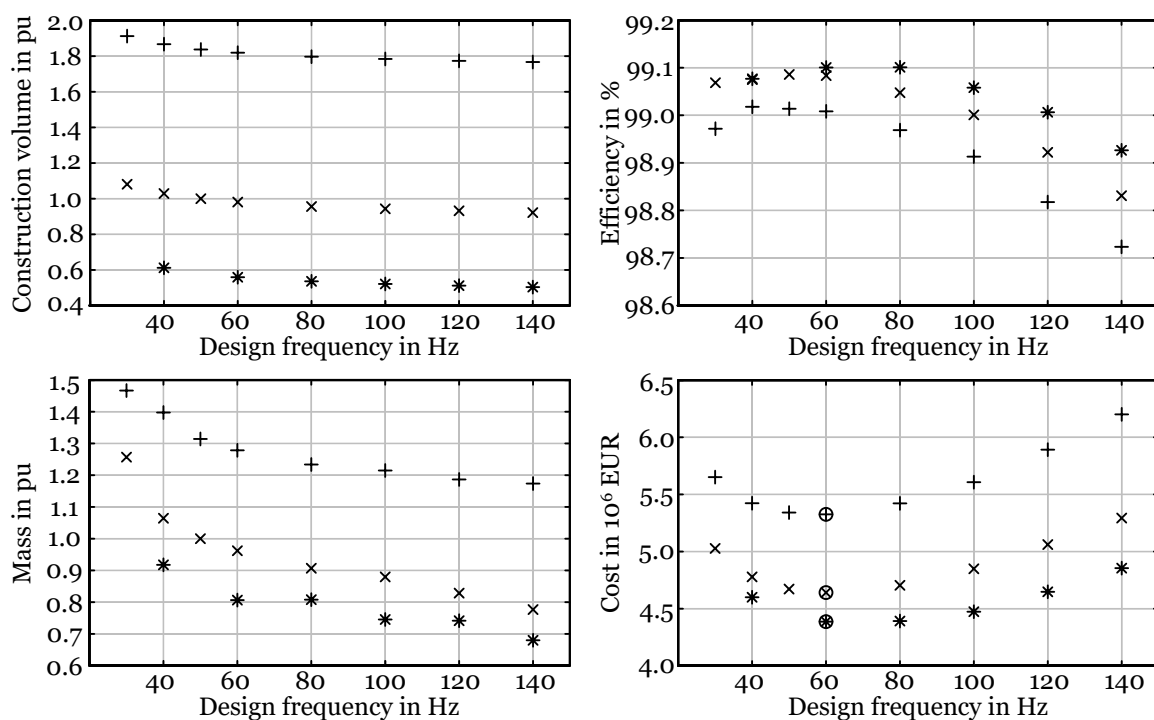


**Figure 4.3:** Construction volume, total mass, efficiency, and cost of the unity power factor designs for various design frequencies and rotational speeds; + = 100 rpm, x = 200 rpm, \* = 400 rpm, o = generator design with minimum costs for the corresponding rotational speed.

Since the start-up time constant (acceleration time constant)  $T_a$  is [12]

$$T_a = J \cdot \frac{\omega_{\text{mech}}^2}{S}, \quad (4.1)$$

<sup>2</sup>Note that it is not possible to design a 400 rpm generator for operation at 30 Hz or 50 Hz, because these designs would require an uneven number of poles. Therefore, Figure 4.3 does not show results for these combinations of rotational speed and frequencies.

a significantly larger mass moment of inertia  $J$  is required for low mechanical angular frequencies  $\omega_{\text{mech}}$  at a given apparent power  $S$  to maintain an equal  $T_a$ . The two parameters that affect the mass moment of inertia  $J$  are the rotor diameter (which is close to the stator inside diameter  $d$ ) and the rotor mass  $m_r$ . The mass moment of inertia for a solid cylinder is

$$J_{\text{cylinder}} = \frac{1}{2} \cdot m_{\text{cylinder}} \cdot \frac{d_{\text{cylinder}}^2}{4} = \frac{\pi}{32} \cdot d_{\text{cylinder}}^4 \cdot l_{\text{cylinder}} \cdot \rho, \quad (4.2)$$

indicating the significant impact of the diameter on the mass moment of inertia:

$$J_{\text{cylinder}} \sim d_{\text{cylinder}}^4. \quad (4.3)$$

### Volume and Mass

Therefore, to achieve an equal  $T_a$ , the 100 rpm generator designs have almost double the construction volumes of the corresponding 200 rpm generator designs. Meanwhile, the 400 rpm generator designs have almost half the construction volume of the corresponding 200 rpm generator designs. On average, the masses of the rotors of the 100 rpm generator designs are only 43 % larger than those of the 200 rpm generator designs, and the masses of the rotors of the 400 rpm generator designs are only 37 % less than those of the 200 rpm generator designs.

### Efficiency

The maximum generator efficiency is highest for the 400 rpm generator designs and lowest for the 100 rpm generator designs. The maximum efficiency for the 100 rpm generator designs is 99.02 % and can be found at 40 Hz; for the 200 rpm generator designs it is 99.09 % at 50 Hz, and for the 400 rpm generator designs it is 99.10 % for both 60 Hz and 80 Hz.

### Cost

The generator cost includes costs for material as well as costs for power loss during operation. The higher the generator's rotational speed, which is set by the turbine for a specific application, the lower the generator's cost. This results from the combination of the reduced amount of material required and the increased efficiency. For all the investigated rotational speeds, the minimum individual cost is at 60 Hz. Therefore, the rotational speed does not influence the choice of the design frequency for the here investigated generator designs.

### 4.2.3 Influence of the Machine Utilization

The generators presented in Sections 4.1 and 4.2.1 are designed for an Esson utilization coefficient of  $8.5 \text{ kVA} \cdot \text{min}/\text{m}^3$  [12]. Figure 4.1 shows that the optimum design frequency for this specific parameter set would be 60 Hz. This Section discusses the influence of the machine utilization on the optimum design frequency. According to [35],  $8.5 \text{ kVA} \cdot \text{min}/\text{m}^3$  represents the upper limit for high-power hydropower generators utilizing air-cooling and therefore, utilizations of  $8.5 \text{ kVA} \cdot \text{min}/\text{m}^3$ ,  $7.0 \text{ kVA} \cdot \text{min}/\text{m}^3$ , and  $5.5 \text{ kVA} \cdot \text{min}/\text{m}^3$  are investigated in this Section, which should cover the typical range. Figure 4.4 shows the construction volumes, total masses, efficiencies, and costs of unity power factor generator designs at various design frequencies for the different machine utilizations.

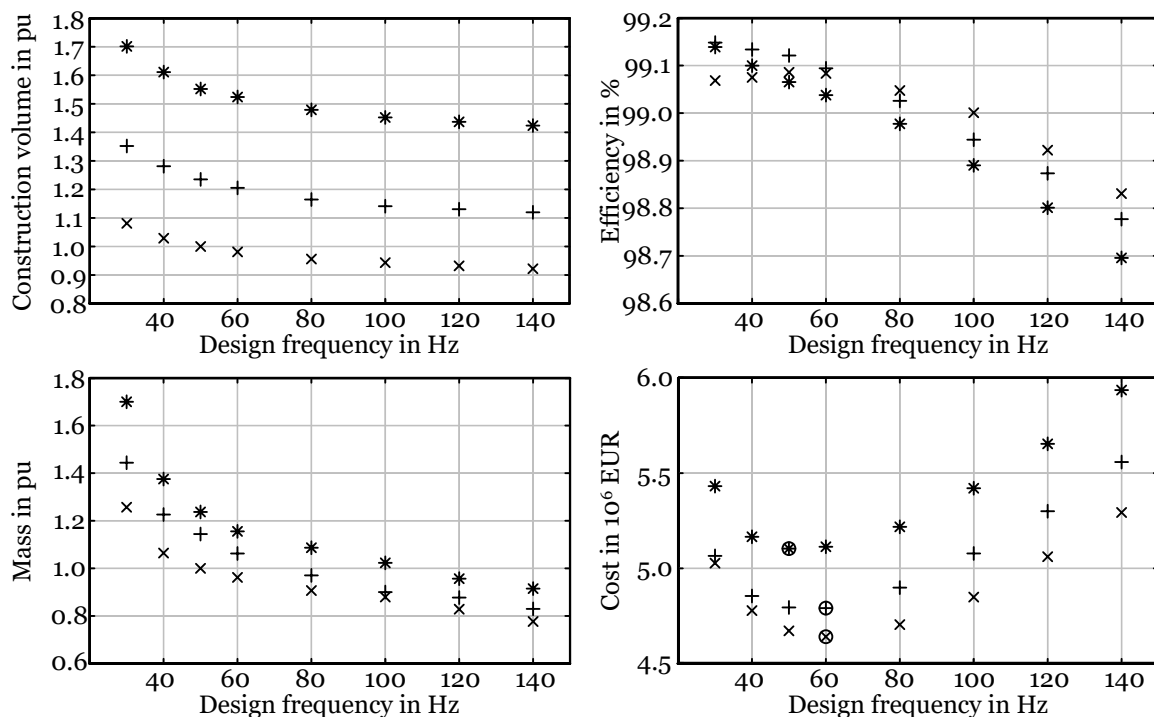


**Figure 4.4:** Construction volume, total mass, efficiency, and cost of the unity power factor designs for various design frequencies and utilization factors;  $\times = 8.5 \text{ kVA} \cdot \text{min}/\text{m}^3$ ,  $+ = 7.0 \text{ kVA} \cdot \text{min}/\text{m}^3$ ,  $* = 5.5 \text{ kVA} \cdot \text{min}/\text{m}^3$ ,  $\circ =$  generator design with minimum costs for the corresponding utilization factor.

### Volume and Mass

With a lower electromagnetic utilization, the amount of material required for the generator construction increases. Therefore, the total construction volume as well as the total mass are lowest for the generator designs with a utilization of  $8.5 \text{ kVA} \cdot \text{min}/\text{m}^3$  presented in Figure 4.4, which represents the highest investigated utilization.

### Efficiency

While the generator designs with a utilization of  $8.5 \text{ kVA} \cdot \text{min}/\text{m}^3$  have its maximum efficiency at 50 Hz, the efficiencies for generator designs using a lower utilization factor are highest for the lowest considered design frequency of 30 Hz. However, much more material is needed.

### Cost

Since the generator cost includes costs for material as well as costs for power loss during operation, the minimum total cost can be found at 60 Hz for the  $8.5 \text{ kVA} \cdot \text{min}/\text{m}^3$  and the  $7.0 \text{ kVA} \cdot \text{min}/\text{m}^3$  designs, and at 50 Hz for the  $5.5 \text{ kVA} \cdot \text{min}/\text{m}^3$  design. Therefore, the utilization factor has only a marginal influence on the optimum design frequency.

#### 4.2.4 Influence of the Cost Factors

The presented computed generator costs in Sections 4.1 and 4.2.1 utilize the cost factors given in Section 3.2.2. Figure 4.1 shows that the optimum design frequency for this specific parameter set would be 60 Hz. The total cost function (3.34) includes costs for materials as well as costs for power loss during operation. Therefore, a different allocation of the power loss evaluation cost factors, as could be the case for a specific practical application, may influence the resulting optimum design frequency. The initial cost factors, as presented in Section 3.2.2, are as follows:

$$C_{\text{fe,s}} = 4 \text{ EUR/kg}; C_{\text{fe,r}} = 6 \text{ EUR/kg}; C_{\text{cu}} = 11 \text{ EUR/kg};$$

$$C_{\text{load}} = 2000 \text{ EUR/kW}; C_{\text{const}} = 3000 \text{ EUR/kW};$$

To analyze the influence of the cost factors on the machine design, the same 135 MW, 50 Hz, 200 rpm, unity power factor motor-generators, as designed in Section 4.2.1, were designed again by minimizing the total cost function (3.34), but this

time with different power loss evaluation cost factors for the load dependent and the constant power losses:

$$C_{\text{load}}/2 = 1000 \text{ EUR/kW}; C_{\text{const}}/2 = 1500 \text{ EUR/kW};$$

$$C_{\text{load}} = 2000 \text{ EUR/kW}; C_{\text{const}} = 3000 \text{ EUR/kW};$$

$$2 C_{\text{load}} = 4000 \text{ EUR/kW}; 2 C_{\text{const}} = 6000 \text{ EUR/kW};$$

The cost factors for the materials are kept constant. Figure 4.5 shows the construction volumes, the total masses, the efficiencies, and the costs of unity power factor generator designs at various design frequencies for different power loss evaluation cost factors for the load dependent and the constant power losses. The individual minimum cost for one parameter set is marked with a circle.

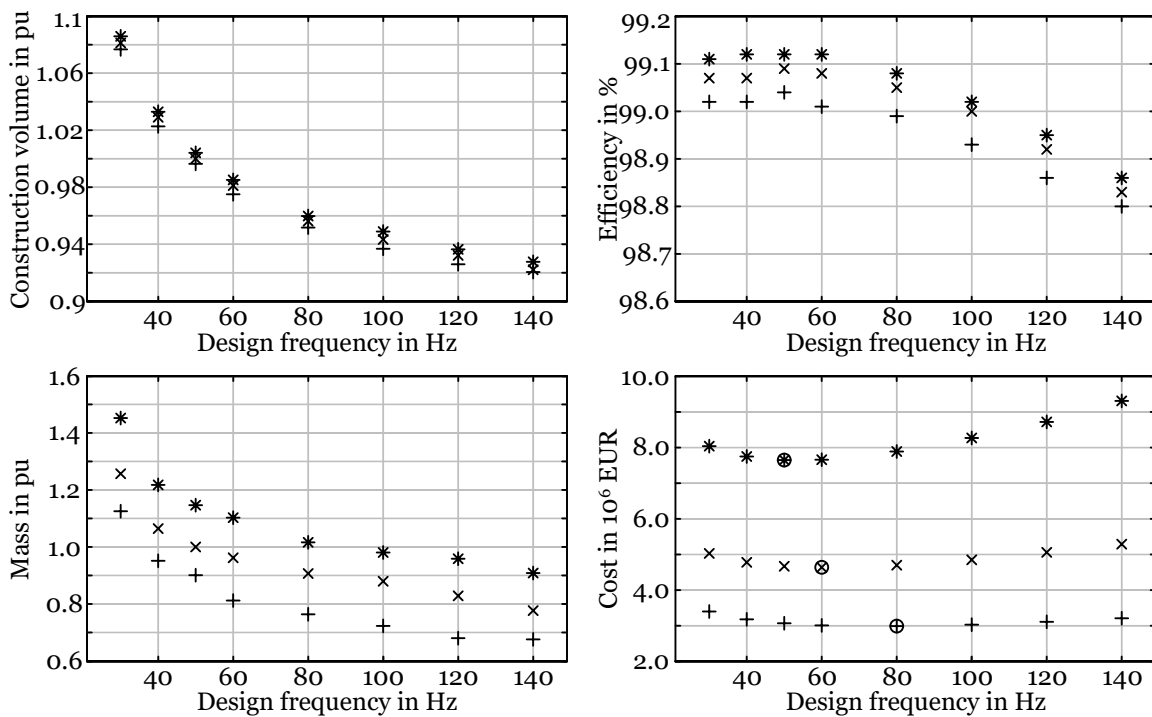


**Figure 4.5:** Construction volume, total mass, efficiency, and cost of the unity power factor designs for various design frequencies and power loss evaluation cost factors; + =  $C_{\text{load}}/2$  and  $C_{\text{const}}/2$ , x =  $C_{\text{load}}$  and  $C_{\text{const}}$ , \* =  $2 C_{\text{load}}$  and  $2 C_{\text{const}}$ , o = generator design with minimum costs for the corresponding power loss evaluation cost factors.

### Volume and Mass

For high costs for power losses, the optimization algorithm aims for high efficiency by increasing the value of active material in the synchronous motor-generator. Therefore, when utilizing  $2 C_{\text{load}}$  and  $2 C_{\text{const}}$ , the total mass is on average 15.4 % higher compared to the initial parameter set of  $C_{\text{load}}$  and  $C_{\text{const}}$ . When utilizing  $C_{\text{load}}/2$  and  $C_{\text{const}}/2$ , the total mass is on average 13.6 % lower compared to the initial parameter set of  $C_{\text{load}}$  and  $C_{\text{const}}$ . The total construction volume is largest when utilizing high costs for power losses, namely  $2 C_{\text{load}}$  and  $2 C_{\text{const}}$ . However, the effect on the construction volume is not as pronounced as for the total mass.

### Efficiency

The maximum efficiency is 99.12 % when utilizing  $2 C_{\text{load}}$  and  $2 C_{\text{const}}$ , 99.09 % when utilizing  $C_{\text{load}}$  and  $C_{\text{const}}$ , and 99.04 % when utilizing  $C_{\text{load}}/2$  and  $C_{\text{const}}/2$ .

### Cost

The higher the costs for power losses are, the lower the optimum design frequency is. Because of the trade-off between the material required to realize the generator and the achieved generator efficiency, the optimum design frequency shifts from 80 Hz to 60 Hz towards 50 Hz when the power loss evaluation cost factors for the power losses increase. Note that the different power loss evaluation cost factors depend on the individual practical application and the customer's requirements.

Knowing that the power loss evaluation cost factors can shift the optimum design frequency, the generator designs presented in the following Sections are computed using the initial power loss evaluation cost factors of Section 3.2.2 to ensure comparability. One single exception for the use of the initial power loss evaluation cost factors is in Section 4.3.3, in which a larger difference between the costs for load dependent and constant power losses ( $C_{\text{load}} = 4000 \text{ EUR/kW}$  and  $C_{\text{const}} = 8000 \text{ EUR/kW}$ ) is used to better illustrate the role of the operating profile in the generator design process.

## 4.3 Operation at a Load Profile

The motivation for implementing the FSC operated synchronous motor-generator in large pumped storage power plants (PSPPs) is the flexibility to adjust the produced as well as the absorbed power to the current needs of the grid. The active power generated in turbine mode can always be controlled by the water flow rate  $Q$  across the turbine. The rotational speed  $n$  is constant for turbine operation. A pump's power consumption is linked to the rotational speed  $n$  and therefore, when utilizing a variable-speed technology like the FSC operated synchronous motor-generator, the power consumption in pumping mode can be controlled as well. Being able to control the active power both in turbine and pumping modes allows the PSPP to participate in the balancing energy market. This, in turn, increases the achievable earnings significantly compared to participation in energy markets only, see Section 2.5. Therefore, this topology will not operate at nominal load all the time and knowing the load profile during operation might influence the optimum design of the generator itself.

Table 4.3 shows an exemplary load profile for operating the PSPP. The parameters 'mode,' 'load,' and 'operating time' are the given values for the load profile. In this example, the power plant operates in turbine mode for half of the time and in pumping mode for the other half of the time. The power plant operates at nominal load for 10 % of the time, at 75 % of the nominal load for 20 % of the time, and at 50 % of the nominal load for 20 % of the time, both in turbine mode T and pumping mode P. Note that the chosen load profile shows quite severe partial load behavior (operating 80 % of the time at  $\leq 75$  % of the nominal load) and a real power plant might not require such drastic behavior. The characteristic operating parameters of the generator operating at this load profile (presented in the lower part of Table 4.3) are then computed utilizing the relations presented in Section 3.2.

### 4.3.1 Turbine Mode

For the investigation of the load profile's influence during operation, at first, only the turbine operation T in Table 4.3 of the PSPP is considered.

**Table 4.3:** Exemplary load profile for operation of the pumped storage power plant and computed motor-generator operating parameters;

T = turbine mode, P = pumping mode.

Operating point	T100	T75	T50	P100	P75	P50
Mode of operation	T	T	T	P	P	P
Load in pu	1.00	0.75	0.50	1.00	0.75	0.50
Operating time in pu	0.10	0.20	0.20	0.10	0.20	0.20
$n$ in pu	1.00	1.00	1.00	1.00	0.91	0.79
$f$ in pu	1.00	1.00	1.00	1.00	0.91	0.79
$U_{ph}$ in pu	1.00	1.00	1.00	1.00	0.91	0.79
$I_{ph}$ in pu	1.00	0.75	0.50	1.00	0.83	0.63
$U_h$ in pu	1.00	0.99	0.98	1.00	0.90	0.79
$\phi_h$ in pu	1.00	0.99	0.98	1.00	1.00	0.99
$\Theta_m$ in pu	1.00	0.98	0.96	1.00	0.99	0.98
$\Theta_s$ in pu	1.00	0.75	0.50	1.00	0.83	0.63
$\Theta_f$ in pu	1.00	0.83	0.69	1.00	0.89	0.78
$I_f$ in pu	1.00	0.83	0.69	1.00	0.89	0.78

### Operating Mode Explanation

In turbine mode, the active power can be controlled by the water flow rate  $Q$  and hence, the rotational speed  $n$  remains constant even at partial load operation. Note that the rotational speed of the turbine and the synchronous generator could be varied at FSC operation in turbine mode to better adjust to the current hydraulic head  $H$  to increase the turbine efficiency for a specific operating point. However, as discussed in Section 2.2.4, this becomes significant only for large variations of the hydraulic head [5]. In addition, at FSC operation of the synchronous generator, the rotational speed could be adjusted to better fit the optimum rotational speed for turbine mode of the combined pump-turbine. This can be 15% lower than the nominal speed in pumping mode [19]. However, this still transfers to a constant rotational speed in turbine mode.

Therefore, the variation of the rotational speed  $n$  and the electrical frequency  $f$  are neglected for this investigation. Hence, these values remain constant for all operating points in turbine mode. As a result, in this investigation, the turbine

mode is treated similarly to the conventional turbine operation of a fixed-speed directly line-connected synchronous motor-generator, as described in Section 2.2.

### Effect on the Motor-Generator's Operating Parameters

The generator stator phase voltage  $U_{ph}$  remains constant in turbine mode. Therefore, the stator phase current  $I_{ph}$  is directly proportional to the load of the current operating point for a constant power factor because

$$P = 3 \cdot U_{ph} \cdot I_{ph} \cdot \cos\varphi. \quad (4.4)$$

Figure 4.6 shows the phasor diagram of the synchronous generator operating at unity power factor. Therein included are the magnetomotive force (mmf) relations to better describe the behavior presented in Table 4.3. It illustrates the relations for operation at unity power factor not only at nominal load (T100, Figure 4.6 (a)) but also for operation at 50 % thereof (T50, Figure 4.6 (b)). The influence of the stator resistance is neglected which is common practice for large synchronous machines. At half the stator phase current  $I_{ph}$ , the voltage drop across the leakage reactance  $X_\sigma$  is halved as well, but the magnitude of the internal voltage  $U_h$  remains fairly constant ( $U_{hT50} = 0.98 U_{hT100}$ ), as does the main flux  $\phi_h$ . Therefore, the overall mmf  $\Theta_m$  remains fairly constant as well at partial load operation. The stator winding mmf  $\Theta_s$  is directly proportional to the stator current  $I_{ph}$ . The geometrical sum of the overall mmf  $\Theta_m$  and the stator winding mmf  $\Theta_s$  results in the required mmf for the rotor winding (field winding)  $\Theta_f$ . The excitation current (field current)  $I_f$  is directly proportional to the rotor winding mmf  $\Theta_f$  which decreases significantly ( $\Theta_{fT50} = 0.69 \Theta_{fT100}$ ) at partial load operation.

### Conclusion

Summarizing, the only quantities that change significantly at partial load operation in turbine mode are the stator phase current  $I_{ph}$  and the field current  $I_f$ . Since the resistive power loss increases with the square of the current,

$$P_{cu} \sim I^2, \quad (4.5)$$

the load dependent power loss  $P_{load}$  changes significantly. The mechanical power loss  $P_{mech}$  remains constant because of the constant rotational speed  $n$ , and the stator iron power loss  $P_{fe}$  remains constant because of the constant electrical frequency  $f$  and the fairly constant air-gap flux  $\phi_m$ .

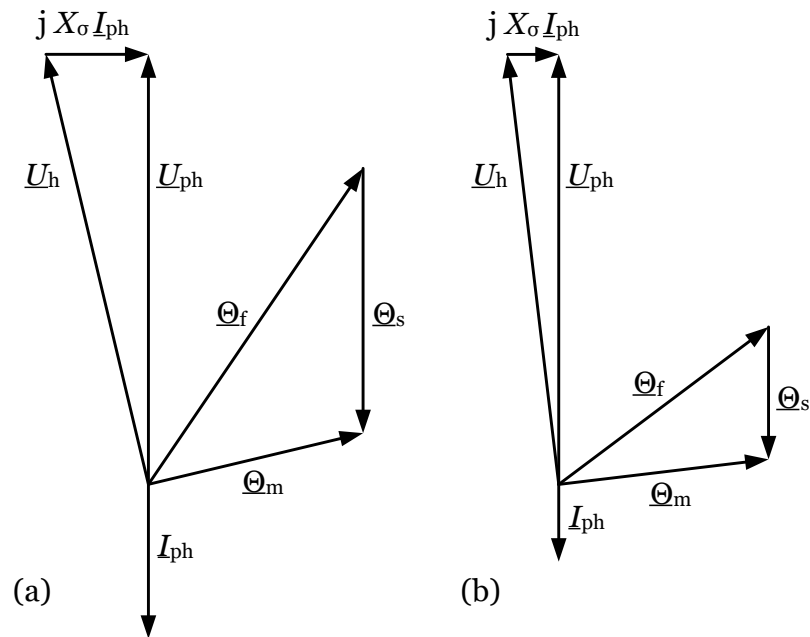


**Figure 4.6:** Phasor diagram of the synchronous generator operating at unity power factor in turbine mode including the mmf relations; (a) nominal load operation (T100); (b) partial load operation at 50% of the nominal load (T50).

### 4.3.2 Pumping Mode

Next, the motor-generator operating parameters in pumping mode P in Table 4.3 are analyzed.

#### Operating Mode Explanation

The synchronous machine's power consumption in pumping mode, due to the pump's mechanical characteristic, follows the relation

$$P \sim n^3, \quad (4.6)$$

which leads to a reduced power consumption  $P$  at reduced rotational speed  $n$ . Therefore, the power plant's power consumption can be controlled in pumping mode when utilizing a variable-speed technology like the FSC operated synchronous motor-generator. When operating the PSPP in pumping mode, the synchronous machine operates as a motor, and the flux in the machine needs to be kept at a constant level throughout the entire speed range. Therefore,

$$U_{ph} \sim f \quad (4.7)$$

operation is required. As a result, the stator phase current  $I_{ph}$  is no longer directly proportional to the output power as in turbine mode.

### Effect on the Motor-Generator's Operating Parameters

Because of (4.7), the main flux  $\phi_h$  remains fairly constant at partial load operation ( $\phi_{h|P50} = 0.99 \phi_{h|P100}$ ), see Table 4.3, as does the overall mmf  $\Theta_m$  ( $\Theta_{m|P50} = 0.98 \Theta_{m|P100}$ ). The stator winding mmf  $\Theta_s$  is directly proportional to the stator current  $I_{ph}$ , which is now higher compared to the turbine mode ( $\Theta_{s|P50} = 1.26 \Theta_{s|T50}$ ). The geometrical sum of the overall mmf  $\Theta_m$  and the stator winding mmf  $\Theta_s$  results in the required mmf of the rotor winding (field winding)  $\Theta_f$  which, again, remains at a higher level compared to the turbine mode. The excitation current (field current)  $I_f$  is directly proportional to the rotor winding mmf  $\Theta_f$  which, again, decreases significantly at partial load operation, but remains at a higher level compared to the turbine mode ( $\Theta_{f|P50} = 1.13 \Theta_{f|T50}$ ).

### Conclusion

To summarize, partial load operation in pumping mode leads to a reduced rotational speed  $n$ , reduced stator phase voltage  $U_{ph}$ , reduced stator phase current  $I_{ph}$ , and reduced field current  $I_f$ . This reduces all sources of power losses in the machine, namely the mechanical power loss  $P_{mech}$ , the stator iron power loss  $P_{fe}$ , and the load dependent power loss  $P_{load}$ .

### 4.3.3 Generator Design for Operation at a Load Profile

The load profile of the motor-generator influences the power loss distribution during operation and thus affects the generator designs created by the cost minimization generator design algorithm, as long as the power loss evaluation cost factors for load dependent and for constant power losses differ. To better illustrate this effect, the values presented in Tables 4.4 and 4.5 are the results for a 135 MW, 120 Hz,<sup>3</sup> 200 rpm,  $\cos \varphi = 1$  generator design with the power loss evaluation cost factors  $C_{load} = 4000$  EUR/kW and  $C_{const} = 8000$  EUR/kW. To highlight the role of the load and

---

<sup>3</sup>Preliminary studies have shown that the overall effect of the load profile on the generator design is quite low for 50 Hz designs. Therefore, the effect is illustrated for 120 Hz synchronous motor-generator designs in this Section. The results for 50 Hz generator designs are given in Appendix C.

thus operating profile, i.e., partial load operation, the power loss evaluation cost factors are chosen significantly larger than the initial values presented in Section 3.2.2. The cost for materials remain, however, unchanged. In addition, the two power loss evaluation cost factors used here differ even by a factor of two (and not by a factor of 1.5, as the initial cost factors). The load profile shown in Table 4.3 is used. Again, this load profile shows quite severe partial load behavior (operating 80 % of the time at  $\leq 75$  % of the nominal load), and a real power plant might not require such drastic behavior. However, these values are chosen to illustrate the role of the load profile in the generator design.

Three different generators have been designed, each with a different optimization objective:

- SG1: minimum costs for nominal load operation
- SG2: minimum costs occurring over the course of the operating profile for turbine mode only (T)
- SG3: minimum costs occurring over the course of the operating profile for both turbine and pumping modes (T + P)

Thereby, the role of the operating profile, i.e., consideration of partial load operation, in the generator design shall be identified.

Table 4.4 shows the power loss distribution (load dependent power losses  $P_{\text{load}}$  and constant power losses  $P_{\text{const}}$ ) of the three generator designs evaluated for nominal load in comparison to the reference motor-generator design SG1. It illustrates the changes in the power loss distribution of the motor-generator designs when using the various optimization objectives listed above.

Table 4.5 shows the actual cost of SG1 (comprising costs for materials and costs for power loss), which was originally designed to minimize the cost for nominal load operation, when operating SG1 at the load profile including turbine mode only (T) and also when operating SG1 at the load profile including both turbine and pumping modes (T + P). These costs are compared with the costs of the generators specifically designed to minimize the cost for these operating profiles (SG2 and SG3). Note that operation in pumping mode only is not addressed individually, because it is analyzed within the evaluation for operation in both turbine and pumping modes.

**Table 4.4:** Power loss distribution of the generator designs evaluated for nominal load compared to the reference design SG1; T = turbine mode only, T + P = turbine and pumping modes.

Design	Minimization target	$P_{\text{load}}$ pu	$P_{\text{const}}$ pu
SG1	Nominal load	1.00	1.00
SG2	Load profile T	1.30	0.88
SG3	Load profile T + P	1.17	0.93

**Table 4.5:** Total cost of the generator designs evaluated for operation at the load profile presented in Table 4.3; T = turbine mode only, T + P = turbine and pumping modes.

Design	Minimization target	Modes of operation	Cost $10^6$ EUR
SG1	Nominal load	T	9.07
SG1	Nominal load	T + P	8.58
SG2	Load profile T	T	8.92
SG3	Load profile T + P	T + P	8.52

### Generator Design for Operation at a Load Profile in Turbine Mode Only

Per the machine's operating principle, in turbine mode, the only power loss type that changes with the load is the load dependent power loss. Hence, the optimization algorithm aims to reduce the constant power losses  $P_{\text{const}}$ , namely the stator iron power loss  $P_{\text{fe}}$  and the mechanical power loss  $P_{\text{mech}}$ , since these power losses remain constant throughout the entire operating range.

Table 4.4 shows that the constant power losses  $P_{\text{const}}$  decrease from 1.00 pu for SG1 to 0.88 pu for SG2, while the load dependent power losses  $P_{\text{load}}$  increase from 1.00 pu to 1.30 pu. Table 4.5 shows a cost reduction of SG2 of 1.7% when comparing the costs of SG1 and SG2 operating at the load profile presented in Table 4.3 in turbine mode only (T).

### Generator Design for Operation at a Load Profile in Turbine and Pumping Modes

In pumping mode, not only the load dependent power losses  $P_{\text{load}}$  decrease with reduced load, but also the constant power losses  $P_{\text{const}}$ , namely the stator iron power loss  $P_{\text{fe}}$  and the mechanical power loss  $P_{\text{mech}}$ , because of the reduced rotational speed  $n$  and electrical frequency  $f$ . Therefore, all the power loss sources decrease at partial load operation. Thus, the ratios between the different types of power loss do not change significantly and thus no power loss type can be specifically addressed during the design.

Table 4.4 shows that for SG3, considering both turbine and pumping modes (T + P), the constant power losses  $P_{\text{const}}$  decrease from 1.00 pu for SG1 to 0.93 pu for SG3, while the load dependent power losses  $P_{\text{load}}$  increase from 1.00 pu to 1.17 pu. This is not as drastic as for the turbine mode only (T) presented earlier and leads to a cost reduction of 0.7 % when comparing the costs for SG1 and SG3 operating in both turbine and pumping modes (T + P), see Table 4.5.

#### 4.3.4 Summary of the Generator Design for Operation at a Load Profile

The possibility for operating at variable speed only translates in a significant cost reduction of the synchronous motor-generator if the following holds true: the load profile includes operation at  $\leq 75\%$  of the nominal load for 80 % of the time (like the partial load profile used during this investigation), the power loss evaluation cost factors for the load dependent and the constant power losses differ significantly, and the design frequency is chosen to be quite high (like the 120 Hz used during this investigation). In contrast, with the more common applications, with generator design frequencies between 40 Hz and 80 Hz and similar power loss evaluation cost factors for load dependent and constant power losses - in contrast to common assumptions - the operating profile including partial load only marginally affects the synchronous motor-generator design.

## 4.4 Synchronous Reactance

Reference [11] showed that with FSC operation, and therefore a decoupling of the synchronous machine from the grid, the conventional requirement for the synchronous reactance to provide static stability to the grid no longer applies. Therefore,

at FSC operation, the synchronous reactance can be adjusted to further optimize the generator design. The synchronous reactance  $x_d$  is inversely proportional to the equivalent air-gap length (including the geometrical air-gap, the effect of slot openings and cooling ducts, and the mmf drop in the iron)  $\delta'$ :

$$x_d \sim \frac{1}{\delta'}. \quad (4.8)$$

Therefore, an increase of  $x_d$  reduces the air-gap length, hence excitation, and thus the field winding power loss.

The generator designs presented so far were computed using a synchronous reactance of  $x_d = 1.1$  pu. Reference [11] investigates 105 MVA hydropower generator designs for pumped storage applications with  $x_d = 1.2$  pu,  $x_d = 2$  pu, as well as no limitation of the synchronous reactance.

For the calculations presented in this Section, the synchronous reactance is set to  $x_d = 1.1$  pu,  $x_d = 1.3$  pu, and  $x_d = 1.6$  pu. For small ratios of air-gap length to slot width (caused by a large  $x_d$ ), the pole shoe surface power loss can increase significantly. This, however, is not computed in this Section, because of the low values for  $x_d$  used in this analysis compared to [11]. No additional boundaries are set on the parameters, i.e., the air-gap can take on any value in the theoretical design. To ensure comparable results, as with the previous analyses, the Esson utilization coefficient  $C$  is held constant and the different synchronous generator designs have identical inner machine volumes and start-up time constants. The optimization algorithm aims, again, to minimize the total cost function for nominal load operation (3.34) using the cost factors presented in Section 3.2.2.

Table 4.6 shows the characteristic values of the generator designs for design frequencies of 50 Hz and 100 Hz and the different values of the synchronous reactance. In addition to the characteristic machine parameters, it shows the excitation demand per pole  $\Theta_f$ , the equivalent air-gap length  $\delta'$ , the mechanical air-gap length  $\delta$ , and the total cost of the generator. Note that the design for operation at 50 Hz  $\cos \varphi = 1$   $x_d = 1.1$  pu is again used as the reference design.

The excitation demand per pole decreases from the  $x_d = 1.1$  pu design to the  $x_d = 1.3$  pu design by 7.4 % and 7.3 % for the 50 Hz and 100 Hz designs, respectively. Increasing  $x_d$  from  $x_d = 1.3$  pu to  $x_d = 1.6$  pu decreases the excitation demand per pole by 7.0 % and 7.3 % for the 50 Hz and 100 Hz designs. The synchronous reactance is mainly determined by the mechanical air-gap length which reduces drastically for high values of  $x_d$ , particularly for high frequency designs. Because of the rotor's

**Table 4.6:** Generator designs for various synchronous reactances for design frequencies of 50 Hz and 100 Hz.

$P$ MW	$\cos \varphi$ -	$f$ Hz	$x_d$ pu	$\Theta_f$ pu	$\delta'$ mm	$\delta$ mm	$m$ pu	$\eta$ %	Cost $10^6$ EUR
135	1	50	1.1	1.00	23.3	16.3	1.00	99.09	4.67
135	1	50	1.3	0.93	19.2	13.4	1.00	99.10	4.63
135	1	50	1.6	0.86	15.1	10.6	1.00	99.11	4.59
135	1	100	1.1	0.50	11.7	8.2	0.88	99.00	4.85
135	1	100	1.3	0.46	9.6	6.7	0.88	99.01	4.81
135	1	100	1.6	0.43	7.6	5.3	0.89	99.03	4.78

radial extension during operation and a possible eccentricity, a mechanical air-gap length of less than 10 mm is difficult to manufacture and hence not realistic for this size of machine. The cost mainly decreases due to the increased efficiencies at higher values of  $x_d$  because of the smaller equivalent air-gap  $\delta'$  of the synchronous machine and hence excitation requirements. The cost for the 50 Hz design decreases by 1 % when increasing the synchronous reactance from  $x_d = 1.1$  pu to  $x_d = 1.3$  pu, while the cost decreases by 0.8 % when increasing  $x_d$  from  $x_d = 1.3$  pu to  $x_d = 1.6$  pu. The cost for the 100 Hz design decreases by 0.8 % when increasing  $x_d$  from  $x_d = 1.1$  pu to  $x_d = 1.3$  pu, while the cost decreases by about 0.7 % when increasing  $x_d$  from  $x_d = 1.3$  pu to  $x_d = 1.6$  pu.

Therefore, for frequencies close to 50 Hz, the synchronous reactance may take larger values than with conventional designs which additionally reduces the cost of the generator design for FSC operation. Hence, the synchronous reactance could be included directly in the generator design optimization tool as an optimization variable while setting the minimum air-gap length as an optimization constraint.

## 4.5 Power Factor

As per Section 4.1, the synchronous generator does not have to provide reactive power when operated by an FSC (considering an AC-DC-AC voltage-source converter arrangement), since the reactive power is provided by the FSC independently to the grid. Therefore, so far, designs for unity power factor operation have been

considered and compared in Sections 4.2 - 4.4. However, the optimum design power factor of the synchronous generator to achieve minimum cost does not necessarily need to be  $\cos \varphi = 1$  [44].

At unity power factor, the stator phase current  $I_{\text{ph}}$  is minimum, since

$$I_{\text{ph}} = \frac{P}{3 \cdot U_{\text{ph}} \cdot \cos \varphi}. \quad (4.9)$$

The field winding power loss and the stator iron power loss are independent of this relation. The field current  $I_f$  is directly proportional to the back-electromotive force (emf)  $U_p$

$$I_f \sim U_p. \quad (4.10)$$

Therefore, the field winding power loss decreases with reduced machine excitation. Alternatively, a conductor with a smaller cross section could be utilized for the field winding, thus reducing the rotor's mass.

The stator iron power loss depends on the main flux  $\phi_h$  and the frequency  $f$ . The latter is constant, but the former is directly proportional to the internal voltage  $U_h$

$$\phi_h \sim U_h, \quad (4.11)$$

which can be computed from the phasor diagram, and decreases with reduced excitation. Therefore, the stator iron power loss decreases with reduced machine excitation.

#### 4.5.1 Power Loss Distribution for Various Power Factors

Figure 4.7 shows the computed total power loss as well as the power loss distribution of the 150 MVA (135 MW), 50 Hz, 200 rpm,  $\cos \varphi = 0.9$  conventional directly line-connected synchronous generator that was used as a starting point for the analysis, see Section 4.1, operating at power factors between 0.9 over-excited and 0.8 under-excited. The load dependent power loss of the stator follows the power factor and has a minimum at  $\cos \varphi = 1$ . The field winding power loss decreases with reduced machine excitation, with a more drastic reduction for the over-excited side of the curve. The stator iron power loss decreases with reduced machine excitation as previously described. The mechanical power loss remains constant throughout the whole region since the rotational speed  $n$  is fixed. The minimum total power loss  $P_{\text{total}}$  occurs around  $\cos \varphi = 0.975$  under-excited.

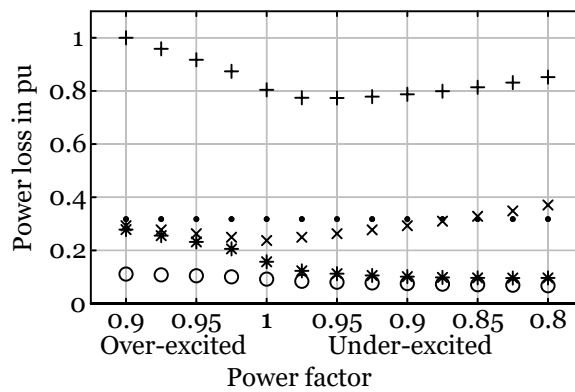


**Figure 4.7:** Power loss distribution of the 150 MVA (135 MW), 50 Hz, 200 rpm,  $\cos \varphi = 0.9$  directly line-connected synchronous generator operating at power factors between 0.9 over-excited and 0.8 under-excited; + = total power loss, × = load dependent power loss of the stator, \* = field winding power loss, o = stator iron power loss, · = mechanical power loss.

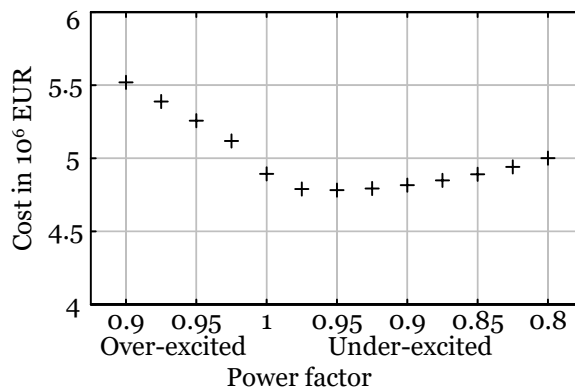


**Figure 4.8:** Total cost of the 150 MVA (135 MW), 50 Hz, 200 rpm,  $\cos \varphi = 0.9$  directly line-connected synchronous generator operating at power factors between 0.9 over-excited and 0.8 under-excited.

### Cost

Figure 4.8 shows the cost of the 150 MVA (135 MW), 50 Hz, 200 rpm,  $\cos \varphi = 0.9$  conventional directly line-connected synchronous generator operating at power factors between 0.9 over-excited and 0.8 under-excited. The total cost is evaluated for each individual operating point, because the power loss distribution changes with different power factors. Since the costs for materials are constant, because only one single generator design is operated at various power factors, the curve's shape of the total cost follows the total power loss presented in Figure 4.7. It shows that the minimum cost does not occur at  $\cos \varphi = 1$ , but somewhere around  $\cos \varphi = 0.975$  under-excited.

## 4.5.2 Generator Design for Under-Excited Operation

Table 4.7 depicts a generator design specifically optimized for the optimum under-excited power factor of 0.98 for a 135 MW, 50 Hz, 200 rpm synchronous generator and the given cost factors in Section 3.2.2, and also compares the results with the earlier presented unity power factor design in Table 4.2.

The 135 MW, 50 Hz, 200 rpm,  $\cos \varphi = 0.98$  under-excited generator design has larger volume and mass compared to the design for unity power factor because of the increased apparent power  $S$ . The efficiency is increased by 0.05 percentage points which is obtained by an increase of the amount of materials used. The reduced operating costs of the generator outweigh the increase of material costs. This leads to a cost reduction of 2% which represents a decent improvement. Note that the under-excited power factor of 0.98 is the optimum for this particular parameter set and the cost factors given in Section 3.2.2. For different parameters and cost factors, the optimum power factor for the generator design needs to be determined anew. Hence, the power factor could be included directly in the generator design optimization tool as an optimization variable.

**Table 4.7:** Comparison of the generator design for unity power factor and the design for under-excited operation.

Motor-generator design	Unity power factor design	Under-excited design
$S$ in MVA	135	138
$P$ in MW	135	135
$Q$ in Mvar	0	27
$\cos \varphi$	1.00	0.98
$f$ in Hz	50	50
$V$ in pu	1.00	1.03
$V_i$ in pu	1.00	1.02
$m_s$ in pu	1.00	1.07
$m_r$ in pu	1.00	1.03
$\eta$ in %	99.09	99.14
Cost in $10^6$ EUR	4.67	4.58

## 4.6 Summary of the Generator Design Aspects for FSC Operation

Operating the synchronous motor-generator of a PSPP with an FSC instead of operating it directly line-connected at the grid provides additional aspects and degrees of freedom for the machine's design process. One powerful aspect to reduce the generator's total cost is the free choice of the power factor. The machine's design frequency can also be chosen freely since it is no longer fixed to the grid frequency. The operating profile including partial load is also an interesting aspect to consider in the design process as is the opportunity to adjust the synchronous reactance.

### 4.6.1 Power Factor

The synchronous generator does not need to provide reactive power to the grid, as this part is taken over by the FSC. Therefore, the machine can be designed for operation at unity power factor only in a first optimization step. This results in a smaller and more efficient machine compared to the conventional directly line-connected synchronous generator. Table 4.2 shows a cost reduction of the unity power factor generator design of 15.4%, including both the costs for material as well as the costs for power loss during operation, compared to the conventional design. However, the minimum total cost of the generator does not necessarily occur at unity power factor where the apparent power of the machine is at its minimum. The minimum for the total power loss of the synchronous machine can be found for slightly under-excited operating points, as illustrated in Figure 4.7. As per Table 4.7, optimizing the generator for a slightly under-excited operating point results in a further cost reduction of 2% of the synchronous motor-generator for FSC operation. This, of course, increases the stator current compared to unity power factor operation and hence, increases the power loss of the FSC, which is investigated in Section 6.2.3.

### 4.6.2 Design Frequency

The free choice of the design frequency is possible due to the decoupling of the synchronous machine via the FSC from the grid. The optimum design frequency results from the trade-off between required material, which decreases for higher design frequencies, and power loss during operation, which increases for higher

design frequencies. Depending on the power loss evaluation cost factors, the optimum design frequency shifts between 50 Hz and 80 Hz, as shown in Figure 4.5. The rotational speed does not affect the optimum design frequency, see Figure 4.3, and the utilization factor has only a marginal influence, see Figure 4.4.

### 4.6.3 Operation at a Load Profile

The main advantage of the FSC operation of synchronous motor-generators in PSPPs is the ability to adapt the absorbed power by adjusting the machine's rotational speed in pumping mode which allows the PSPP to also participate in the balancing energy market and hence, increases the achievable earnings. Therefore, this topology operates at partial load for a substantial part of the time. Although the partial load profile leads to changes in the machine design when the overall cost is minimized, the savings related to the motor-generator for a realistic partial load profiles, design frequencies between 40 Hz and 80 Hz, and common power loss evaluation cost factors are negligible.

### 4.6.4 Synchronous Reactance

As described in [11], an FSC operated synchronous generator is not subject to the requirement for the static stability of a directly line-connected machine. Therefore, the synchronous reactance can be increased which results in a smaller air-gap length and, in turn, reduces the machine's excitation demand. This leads to a more efficient, and therefore, cheaper synchronous generator. However, because of the manufacturing of the synchronous generator and the pole shoe surface power loss, a minimum air-gap length needs to be maintained.

## 4.7 Suggested Generator Design for FSC Operation

Table 4.8 shows the conventional example-case directly line-connected 150 MVA, 50 Hz, 200 rpm,  $\cos \varphi = 0.9$  motor-generator, the motor-generator designed for active power only, i.e.,  $\cos \varphi = 1$ , for 50 Hz, as presented in Table 4.2, the unity power factor design for 60 Hz, and the suggested generator design for FSC operation. All the designs operate at the same machine utilization and have the same start-up time constants. The suggested generator design combines the free choice of the design frequency  $f$  presented in Section 4.2, the reduced requirements for the synchronous

reactance presented in Section 4.4, as well as the adjustment of the power factor for rated under-excited operation presented in Section 4.5. The information on the operating profile including partial load operation presented in Section 4.3 is not used for the design process. The reason for this is that, as previously discussed, the influence on the total generator cost for the utilized cost factors given in Section 3.2.2 is negligible. The optimization process to create the suggested generator design for full-size converter operation is carried out step-by-step. The performed steps are outlined in the following:

1. Set the design specifications for the generator design.
2. Run the optimization to minimize the total cost for each individual design frequency for unity power factor.
3. Select the design frequency which results in the minimum total cost.
4. Run the optimization to minimize the total cost for various power factors.
5. Select the power factor which results in the minimum total cost.
6. Run the optimization to minimize the total cost for a range of values for the synchronous reactance.
7. Select the design with the minimum total cost which maintains the minimum required air-gap length.

The 60 Hz design would result in minimum costs for the unity power factor design approach, as illustrated in Figure 4.1. Compared to the reference design for unity power factor for 50 Hz, the 60 Hz design shows a reduced construction volume  $V$  and stator mass  $m_s$  because of the reduced flux at higher design frequencies. The inner machine volume  $V_i$  is the same for both machines because of the same machine utilization and the same apparent power. The rotor mass  $m_r$  decreases slightly for the 60 Hz design, since a larger inside diameter of the machine allows for a smaller rotor mass to obtain an equal mass moment of inertia  $J$ .

Compared to the unity power factor operation 135 MVA design for 50 Hz, which represents the reference for this comprehensive analysis, the suggested generator design for FSC operation is designed for a larger apparent power of  $S = 138$  MVA. This results in a larger construction volume  $V$ , a larger inner machine volume  $V_i$ ,

**Table 4.8:** Comparison of a conventional directly line-connected motor-generator design, the reference design for unity power factor for 50 Hz, the design for unity power factor for 60 Hz, and the suggested generator design for FSC operation.

Motor-generator design	Conventional design	Unity power factor design	Unity power factor design	Suggested design
$S$ in MVA	150	135	135	138
$P$ in MW	135	135	135	135
$Q$ in Mvar	65	0	0	27
$\cos \varphi$	0.90	1.00	1.00	0.98
$f$ in Hz	50	50	60	60
$x_d$ in pu	1.1	1.1	1.1	1.2
$V$ in pu	1.11	1.00	0.98	1.01
$V_i$ in pu	1.11	1.00	1.00	1.02
$m_s$ in pu	1.09	1.00	0.88	0.97
$m_r$ in pu	1.14	1.00	0.99	1.03
$\eta$ in %	98.87	99.09	99.08	99.14
Cost in $10^6$ EUR	5.52	4.67	4.64	4.54

and therefore, larger stator and rotor masses  $m_s$  and  $m_r$  compared to the 60 Hz unity power factor design. The synchronous reactance for the suggested generator design is set to  $x_d = 1.2$ , compared to  $x_d = 1.1$  for the reference design. The suggested design has a significantly higher efficiency  $\eta$ , which directly results in overall minimum total cost.

Compared to the conventional directly line-connected synchronous generator design for 50 Hz  $\cos \varphi = 0.9$  over-excited, the suggested generator design for FSC operation for 60 Hz  $\cos \varphi = 0.98$  under-excited shows a total cost reduction of 18 %, which is significant and represents a valuable advantage.

## Chapter 5

# Power Converter Topologies for Medium-Voltage High-Power Applications

*This Chapter discusses the particularities of today's power converter topologies when operating large electrically excited salient-pole synchronous motor-generators in pumped storage power plants, which is a medium-voltage high-power application. First, the ratings and characteristics of the available and commonly utilized semiconductor power switches are analyzed. Then, the limitations of established multilevel voltage source converters are reviewed, particularly the individual maximum achievable operating voltage, and the usability of direct AC-AC converters is discussed. Next, modular multilevel converter topologies are given special attention, because of their arbitrary scalability and excellent performance. The characteristics of the two main arrangements, the modular multilevel converter and the modular multilevel matrix converter, are analyzed with respect to the torque-speed characteristic of the installed reversible-speed pump-turbines. A review of commercially available power converters for medium-voltage high-power drive applications and their specifications as well as the identification of promising power converter topologies for operation in large pumped storage power plants complete this comprehensive analysis.<sup>1</sup>*

---

<sup>1</sup>Selected material of this Chapter has also been published in [13].

## 5.1 Particularities of Power Converter Application in Large Pumped Storage Power Plants

The full-size converter (FSC) operation of large hydropower generators corresponds to a medium-voltage ( $\geq 13.5$  kV) high-power ( $\geq 100$  MW) regenerative power (bidirectional power flow) application. These particularities of application in large pumped storage power plants (PSPPs) represent a challenging task for today's commercially available power converters. Especially the scalability of the power converters towards higher voltages is problematic. The power converters used in large PSPPs so far have been specifically designed and produced for each application [5]. Several reviews of power converter topologies for medium-voltage applications are available. Reference [45] specifically addresses 2.3 kV line-to-line voltage applications, reference [46] provides a more general overview including low-power and high-power converters ranging from about 2.3 kV to 13.8 kV. Reference [47] offers a good overview of the recent developments of modular multilevel power converter topologies. Many details about high-power converters can also be found in [48]. However, these do not specifically deal with the required voltage and power rating and generally do not allow for bidirectional power flow.

This Chapter closes this gap by providing an overview of the possible choices of power converter topologies for driving large synchronous motor-generators in PSPPs as well as by identifying their individual advantages and disadvantages.

Special attention is paid to the practical limitation given by the maximum achievable voltage rating of the individual power converter topologies, since, as already mentioned, a medium-voltage rating of  $\geq 13.5$  kV is required for application of synchronous motor-generators in large PSPPs.

Note that only voltage source converters (VSCs) are considered in this analysis because of their relevance in today's industrial drive and high-power applications. The current source converter for application in large PSPPs would be another aspect of extensive research, which is beyond the scope of this thesis.

The bidirectional power flow requires the AC-DC-AC VSCs, presented in Section 5.3, to utilize an active front-end (back-to-back configuration), see Section 5.3.5. The second option to allow for bidirectional power flow is to utilize a direct AC-AC power converter topology, see Section 5.4.

In general, when choosing the power converter topology for a given application, the following components are subject to a design trade-off of the power converter:

The number and rating of the semiconductor power switches, power diodes, flying capacitors, and DC-link capacitors, the necessity of a phase-shifting transformer, as well as the filter requirements.

## 5.2 Review of Semiconductor Power Switches for High-Power Applications

Today's power converter market is dominated by VSCs. For voltages of some kV, integrated gate commutated thyristors (IGCTs) and insulated gate bipolar transistors (IGBTs) are used.

Reference [49] offers a good comparison of the properties, advantages, and disadvantages of IGBTs and IGCTs. Compared to IGCTs, IGBTs offer snubber-less operation, a simple parallel connection of devices, as well as low gate drive power loss. However, they have higher on-state power loss. The maximum achievable power of a single IGBT is less than that of a single IGCT because of the higher on-state resistance and the lower silicon utilization [50,51].

Table 5.1 presents an overview of the voltage and current ratings of exemplarily chosen IGBTs from Infineon [52] which represent a good general market overview. The Table illustrates that choosing an IGBT always presents a trade-off between high voltage and high current.

Table 5.2 shows currently available exemplary high-voltage semiconductor power switches from Mitsubishi [53] and ABB [54,55]. It also illustrates that IGCTs are a powerful semiconductor power switch technology for medium-voltage high-power applications due to the high voltage and current rating of one single power switch.

**Table 5.1:** Ratings of IGBT modules available from data-sheets from Infineon [52], as per August 2019.

Blocking Voltage	6.5 kV	4.5 kV	3.3 kV	1.7 kV
Current	0.75 kA	1.2 kA	1.5 kA	3.6 kA

In medium-voltage high-power converter applications it is mandatory to only utilize about 50 % of the semiconductor power switches' blocking voltage capability [56,57], i.e., 50 % of the data-sheet values for the blocking voltages presented in

**Table 5.2:** Ratings of IGCTs available from data-sheets from Mitsubishi [53] and ABB [54,55], as per August 2019.

	Mitsubishi	ABB	ABB
Blocking Voltage	6 kV	6.5 kV	4.5 kV
Current	6 kA	3.8 kA	5 kA

Tables 5.1 and 5.2, to ensure the required reliability.

Both Tables 5.1 and 5.2 show that high blocking voltages, as necessary for the application in large PSPPs, can only be obtained by a series connection of semiconductor power switches.

A series connection of semiconductor power switches, which would require them to operate simultaneously imitating a single switch, impedes achieving high power quality and is hardly possible. This is due to the unequal distribution of the blocking voltage between the semiconductors, resulting from the different static and dynamic characteristics of the semiconductor power switches and their gate drives [58], which requires additional measures. Equal voltage sharing in blocking mode requires an additional circuit which adds to the total number of components and produces additional power loss. Therefore, the conventional two-level (half-bridge) VSC (see Figure 5.1 (a)) cannot be used when the application requires high blocking voltages.

This problem does not occur with multilevel power converter topologies, see Section 5.3, because the semiconductor power switches are not connected in series directly and hence, they operate individually.

Today's commercially available industrial drives (see Section 5.6) both use multilevel power converter topologies and a series connection of two (or even three) semiconductor power switches to increase the maximum operating voltage, which can be usually achieved with a specific multilevel power converter topology, see Section 5.3, even further.

Modular multilevel converters (MMCs), see Section 5.5, can be scaled arbitrarily to meet the desired operating voltage without connecting semiconductor power switches directly in series. This scaling is achieved by simply increasing the number of voltage levels by adding a certain number of identical building blocks [59], i.e., to build 15 levels as for the MMC presented in Chapter 6. Although switches capable of blocking 6.5 kV are commercially available, the trend for the MMC topology is moving towards the use of low-voltage (1.7 kV) IGBTs because they are significantly

more mature and less costly [60]. Therefore, high-power MMCs are built from these low-voltage IGBTs [61], utilizing a high number of voltage steps.

## 5.3 Multilevel Voltage Source Converter Topologies

Most established conventional power converter topologies do not allow for meeting the requirements for medium-voltage ( $\geq 13.5$  kV) high-power ( $\geq 100$  MW) bidirectional power flow and hence, as already mentioned, they have been specifically designed for each individual application in PSPPs so far. This Section reviews the conventional multilevel power converter topologies and their limits.

Multilevel power converter topologies not only allow achieving high blocking voltages. Utilizing a multilevel topology also reduces the total harmonic distortion, lowers the  $du/dt$  of the voltage waveform, reduces the common-mode voltage, and allows for operation at lower switching frequencies [62].

### 5.3.1 Neutral Point Clamped and Flying Capacitor Voltage Source Converters

The most established multilevel topologies are the neutral point clamped (NPC) VSC and the flying capacitor (FC) VSC. Figure 5.1 (b) shows a 3-level NPC VSC and Figure 5.1 (c) shows a 4-level FC VSC, respectively. In principle, these multilevel power converter topologies can be extended to a higher number of voltage levels and therefore, a higher operating voltage without putting semiconductor devices directly in series. However, the number of power switches and diodes or flying capacitors increases significantly. (I.e., the number of switches and clamping diodes required for a three-phase 3-level NPC is 12 and 6 respectively, while the number of switches and clamping diodes required for a three-phase 5-level NPC is 24 and 36 respectively, assuming equal voltage rating of the components [62].) In addition, the capacitor voltage balancing becomes challenging. Therefore, the NPC and FC VSCs are not commercially available with a high number of voltage levels. The NPC VSC for high-power applications is typically limited to a 3-level configuration, while the FC VSC is rarely seen, see Table 5.3. The 3-level NPC is commercially used for a voltage range of 2.3-4.16 kV without series connection of devices, realized with IGBTs with the maximum blocking voltage of 6.5 kV [58].

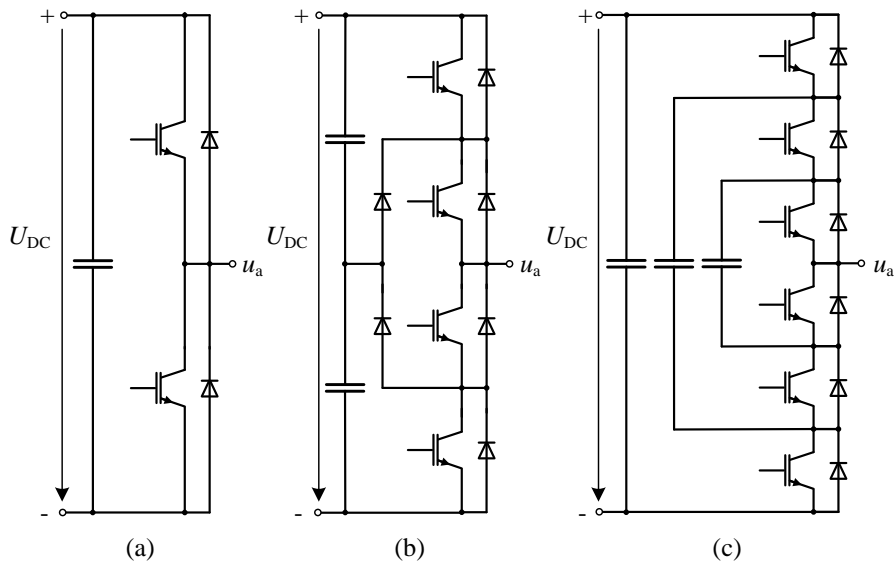


**Figure 5.1:** Per-phase diagrams of VSC topologies: (a) half-bridge, (b) neutral point clamped, and (c) flying capacitor.

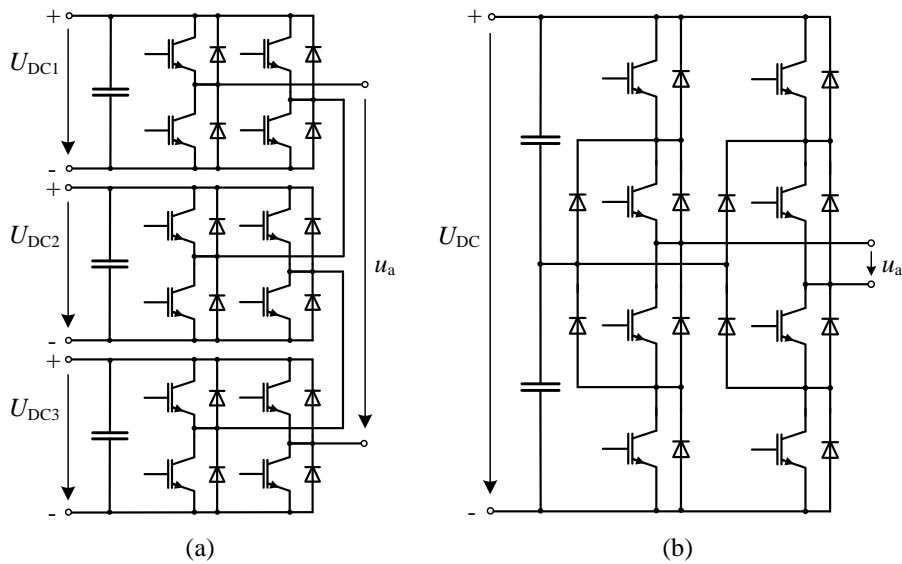


**Figure 5.2:** Per-phase diagrams of VSC topologies: (a) cascaded H-bridge and (b) H-bridge NPC.

### 5.3.2 Cascaded H-Bridge Voltage Source Converter

The cascaded H-bridge (CHB) VSC (see Figure 5.2 (a)) consists of a number of H-bridges which are all fed by individual DC-link voltages. This usually requires a phase-shifting transformer (see Section 5.3.5) to produce the individual isolated voltages. By adding additional H-bridges with individual DC-links, the number of voltage levels and therefore the operating voltage can be increased [63]. Due to the size and the cost of the phase-shifting transformer, the operating voltage is limited to a maximum of 13.8 kV [47].

### 5.3.3 H-Bridge Neutral Point Clamped Voltage Source Converter

The H-bridge NPC (HNPC) VSC is a further development of the CHB VSC which utilizes 3-level NPCs instead of H-bridges. Therefore, the number of output levels is increased as well as the maximum operating voltage. Although it is possible to cascade this power converter topology like the CHB, due to the complex control this is not seen in commercially available industrial drives, and the topology is therefore limited to the configuration shown in Figure 5.2 (b). Without a series connection of semiconductor power devices, this topology is limited to 7.2 kV [58].

### 5.3.4 Advanced Multilevel Topologies

Power converter topologies for medium-voltage drive applications are continuously developed, notably, with the aim to reduce the number of required components (semiconductor power switches, diodes, capacitors) and to eliminate the phase-shifting transformer [64]. However, such as the NPC VSC and FC VSC, these topologies are not arbitrarily scalable due to economic constraints. They are only developed for one specific voltage rating, such as the 5-level converter presented in [65] for a 6.6 kV application and thus, they are not considered for application in large PSPPs, and hence, preclude the scope of this Chapter.

### 5.3.5 Bidirectional Power Flow of Multilevel Voltage Source Converters

Most of the commercially available power converters for high-power drive applications utilize a diode front-end (DFE) which only allows for motor operation (unidirectional power flow). DFEs normally come as multi-pulse diode rectifiers with

a phase-shifting transformer which leads to advantages like reduced grid-side harmonics to meet the standards, increased input power factor, and low-order harmonic cancellation [48].

Figure 5.3 shows an example of a 24-pulse diode rectifier. The required phase-shifting transformer has four secondary windings in different configurations (star, delta, and zig-zag) and phase-shifts. This allows for different resulting phase-shifts for all the secondary side windings feeding the 6-pulse diode rectifiers. The number of windings on the secondary side differ to obtain equal output voltages for all four secondary windings.

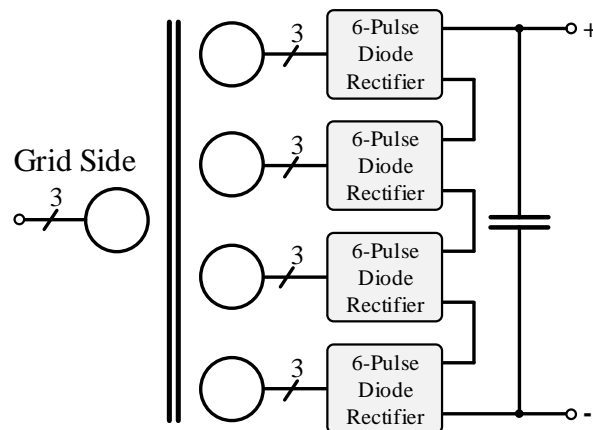


**Figure 5.3:** 24-pulse series-type diode rectifier.

Supplying a reversible-speed pump-turbine also requires a regenerative power capability (bidirectional power flow) which makes an active front-end (AFE) at the grid side necessary, when an AC-DC-AC power conversion is taken into consideration. An AFE is normally achieved with a back-to-back arrangement where the grid-side converter has the same topology as the motor-side converter, i.e., a 3-level NPC VSC, see Figure 5.1. The second option to allow for bidirectional power flow is to utilize a direct AC-AC power converter topology (no intermediate DC-link), as discussed in the following Section.

## 5.4 Direct AC-AC Power Converters

### 5.4.1 Matrix Converter

The matrix converter (MC) is a direct AC-AC converter (see Figure 5.4 (a)) and therefore, it has no intermediate DC-link. It offers bidirectional power flow capability and has a fast dynamic response due to its single-stage energy conversion [58]. A grid-side filter is required to reduce the high-frequency switching harmonics [66].

The core element of the MC are the bidirectional switches which can each both carry the current and block the voltage in both directions. (E.g., Figure 5.4 (b), where two IGBTs are used as one bidirectional switch.) At any time of operation, the filter capacitor must not be short-circuited, and the inductive load current must not be interrupted. Therefore, a complex multi-step commutation technique needs to be implemented, and only three switches must be turned on each time [67].

### 5.4.2 Multi-Modular Matrix Converter

To increase the MC's voltage and power rating, a phase-shifting transformer can be utilized to obtain a multi-modular matrix converter, see Figure 5.5 (a). The multi-modular matrix converter also requires a complex multi-step commutation technique where the same constraints as already identified for the MC are applicable. At the time of writing, the largest commercially available multi-modular matrix converter, the "FSDrive MX1S" by Yaskawa, has a power rating of 6 MVA and a voltage rating of 6.6 kV. It comprises a phase-shifting transformer supplying 18 3x1 MC modules (see Figure 5.5 (b)) and allows for bidirectional power flow [48, 68].

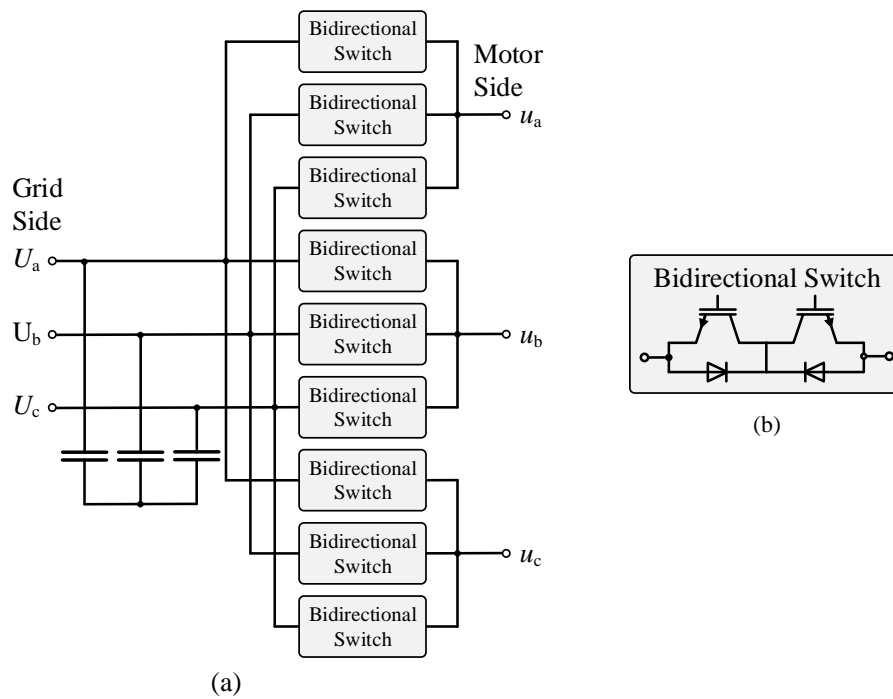


**Figure 5.4:** Direct AC-AC converters and their building blocks: (a) MC topology and (b) bidirectional power switch.

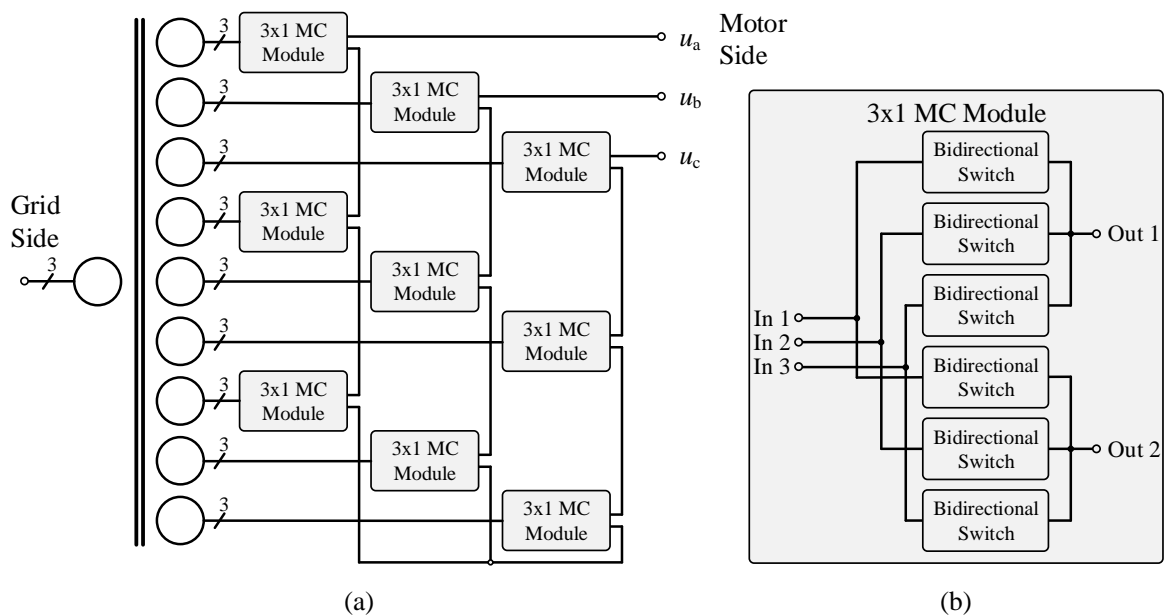


**Figure 5.5:** Direct AC-AC converters and their building blocks: (a) multi-modular matrix converter and (b) 3x1 MC module.

## 5.5 Fully Scalable Modular Multilevel Converter Topologies

In addition to the medium-voltage ( $\geq 13.5$  kV) high-power ( $\geq 100$  MW) bidirectional power flow requirements for the application in large PSPPs, the realized voltage waveform is critical. The lower the number of voltage levels, the higher the voltage stress on the motor-generator winding insulation, and the higher the total harmonic distortion which leads to additional power loss in the synchronous machine. Therefore, an additional filter is often required. The same applies to the grid-side power converter when it comes to a back-to-back arrangement to fulfill the grid requirements regarding the harmonic content.

Two power converter topologies are given special attention in this Chapter due to their arbitrary scalability to higher voltages: the modular multilevel converter (MMC) which is already commercially available and the modular multilevel matrix converter (MMMC) which has been proposed recently for FSC operation in PSPPs [69].

### 5.5.1 Modular Multilevel Converter

Originally developed for application in high-voltage DC transmission (HVDC) [16, 70], the MMC has been adapted for application in medium-voltage drives. Figure 5.6 (a) shows the topology of a single DC-AC stage of an MMC. It consists of three legs which are each split into two arms. Each arm consists of  $n$  submodules of half-bridge type, see Figure 5.8 (b). The corresponding number of levels of the output phase voltage of the MMC is  $n + 1$ .

Each submodule consists of two IGBTs with built-in anti-parallel diodes and a capacitor. Thus, in contrast to the direct placement of the capacitors in the DC-link of conventional multilevel VSCs, the capacitors are distributed over the entire power converter topology. Furthermore, no isolated DC supplies, which are needed in other multilevel topologies, are required in the MMC topology. Each submodule voltage  $U_{SM}$  can either be zero ( $Q_2$  conducts) or take on the capacitor voltage  $U_{C,SM}$  ( $Q_1$  conducts) [58]. The combination of voltages inserted in the upper and the lower arm of the MMC results in the output voltage.

Due to the modular multilevel structure, the voltage ratings of the components in the submodules can be relatively small, which presents an immense benefit. Therefore, cost-effective and reliable low-voltage (1.7 kV) IGBTs can be used to realize

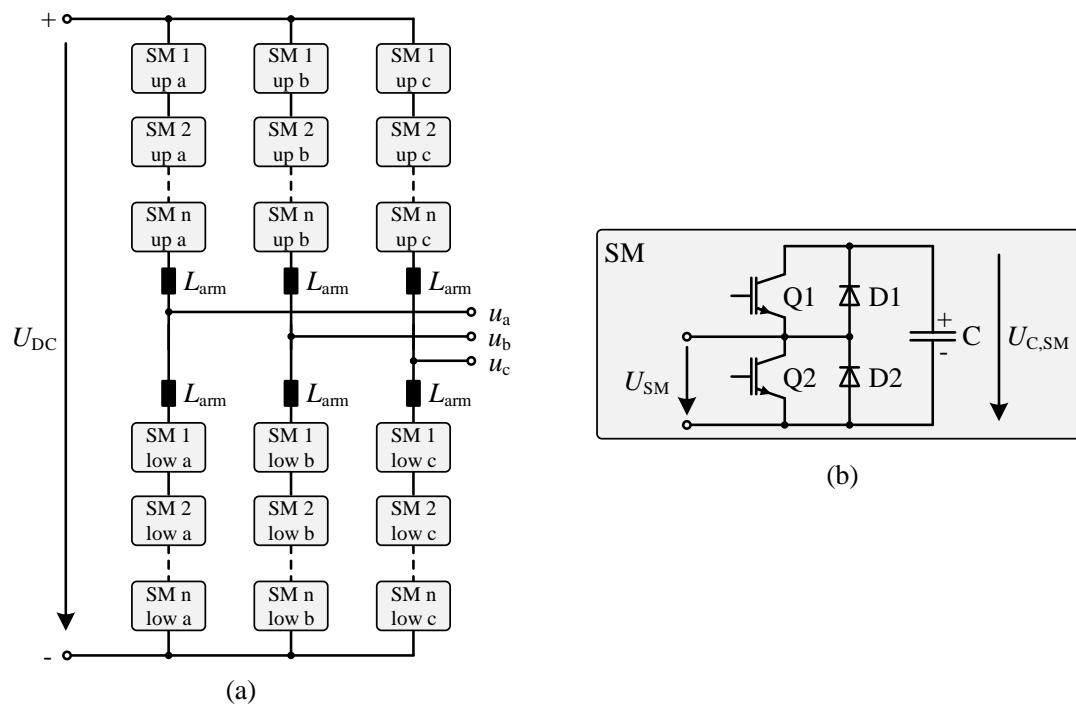


**Figure 5.6:** Modular multilevel converter: (a) topology for DC-AC conversion and (b) half-bridge submodules.

this power converter topology.

The challenge of operation is the proper capacitor voltage balancing of the submodules during operation. Due to the different voltage levels of the submodules during operation, currents between the phase legs may occur, also known as circulating currents. These currents cause additional power loss in the MMC. So-called arm inductors  $L_{arm}$  are installed in each arm to limit these circulating currents. However, the implementation of a proper circulating current control to further reduce these circulating currents is of utmost importance [58].

In addition, especially at low-frequency operation of the MMC, the capacitor voltage ripple may exceed the capacitor voltage ratings if no counter measures are taken, since at constant load torque, the capacitor voltage ripple is inversely proportional to the output frequency. One option is to choose higher rated capacitors which requires additional space and is costly. Another possibility to keep the capacitor voltages within the required limits is to implement special control strategies. For this approach, circulating currents and common-mode voltage are usually injected

to reduce the capacitor voltage ripple during low-frequency operation. However, injecting these additional circulating currents at low-frequency operation exceeds the current ratings of the MMC for nominal frequency operation (50 Hz or 60 Hz) and hence, the current rating of the MMC needs to be increased [71]. Another option is to operate the MMC with a reduced DC-link voltage [72]. This could be realized, e.g., with a silicon controlled rectifier [48]. However, to obtain the required bidirectional power flow for pumped storage applications, the power converter topology utilizes MMCs both for the grid side and the motor side (back-to-back configuration). The common MMC with half-bridge submodules is not capable of reducing the DC-link voltage. Therefore, to enable reduction of the DC-link voltage with the MMC, H-bridge submodules would be required. This approach doubles the number of semiconductor power switches and therefore adds significantly to the power converter's cost.

Pumped storage applications have an  $T \sim n^2$  characteristic in pumping mode and therefore need less current at low-frequency operation compared to constant torque applications. However, the start-up torque might be considerably high for pumped storage applications to start-up the pump directly in water. Reference [73] shows that a start-up torque of 40 % of the nominal torque  $T_n$  can be achieved with an MMC without exceeding any ratings of the devices.

Summarizing, because of the arbitrary scalability to higher voltages, the low voltage stress on the winding insulation, as well as the low total harmonic distortion, and the possibility to operate the synchronous motor-generator at variable-speed without exceeding the component ratings compared to nominal frequency operation, the MMC is a good choice for medium-voltage ( $\geq 13.5$  kV) high-power ( $\geq 100$  MW) PSPP applications. (Figure 5.7 shows the block diagram of FSC operation of the SG in a PSPP utilizing two single MMC DC-AC stages.)

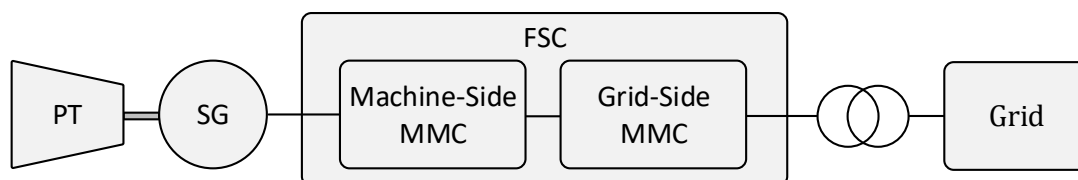


**Figure 5.7:** Block diagram of FSC operation of the SG in a PSPP utilizing two single MMC DC-AC stages (PT = Pump-Turbine, SG = Synchronous Motor-Generator, and FSC = Full-Size Converter).

Therefore, the MMC is further analyzed in Chapter 6 for application in PSPPs and the voltage waveforms of the MMC are used for the investigations carried out at the test bench presented in Chapters 7 and 8.

### 5.5.2 Modular Multilevel Matrix Converter

The MMMC is a more recent development in direct AC-AC power converters. Figure 5.8 (a) shows the schematic of this topology. It utilizes a number of H-bridge cells (see Figure 5.8 (b)) depending on the supply voltage and the ratings of the used semiconductor power switches. It is fully scalable to higher voltages which is a significant difference to conventional AC-AC converters, like MCs and multi-modular MCs. It also offers the bidirectional power flow required for operation in PSPPs. Each of the grid phases is connected via an inductor and a series connection of cells with each phase of the machine.

Capacitor voltage ripple balancing also has to be encountered with the MMMC. In contrast to the MMC, the MMMC suffers from increased cell capacitor voltage ripple for output frequencies close to the feeding frequency (grid frequency). Therefore, capacitor voltage ripple mitigation is required for high operating frequencies, i.e., 50 Hz or 60 Hz [74].

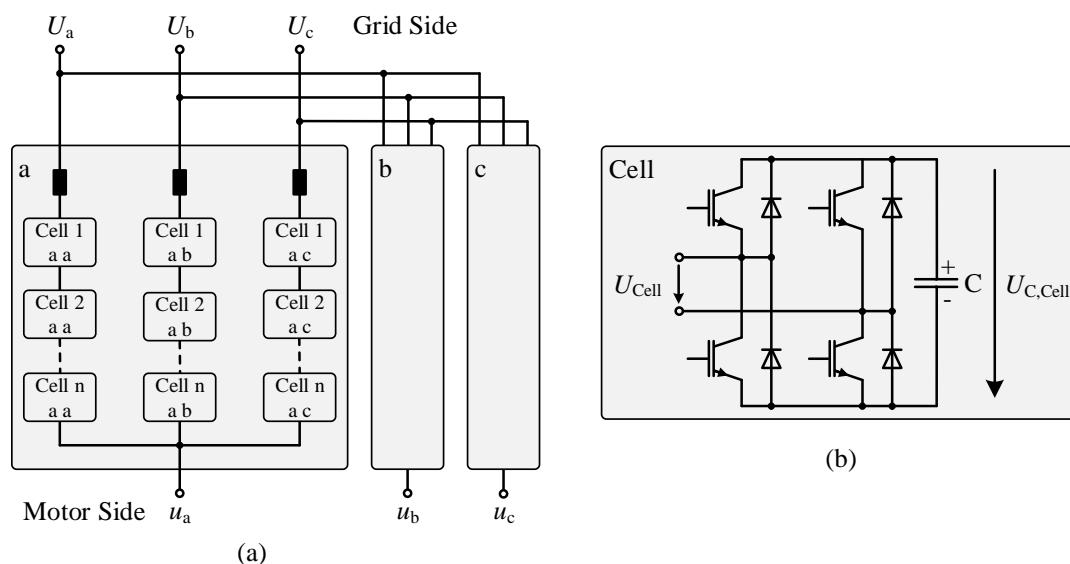


**Figure 5.8:** Modular multilevel matrix converters: (a) circuit configuration and (b) H-bridge cells.

Reference [69] proposes the MMC for application in large PSPPs and suggests an upper limit for the generator design frequency of 35 Hz for reasonable operation of the MMC. However, the analysis presented in Chapter 4 shows that the optimum design frequency for FSC operated synchronous motor-generators in large PSPPs is around 60 Hz. Therefore, considering this comprehensive analysis, the MMC is not the recommended choice for FSC operation of large PSPPs and hence, it is not further investigated.

## 5.6 Power Converter Manufacturer Overview

This Section shows currently commercially available power converters for operation in PSPPs at lower power than investigated here. Even though they do not meet the requirements for medium-voltage ( $\geq 13.5$  kV) high-power ( $\geq 100$  MW) bidirectional power flow, a few classical multilevel topologies are reviewed as well in this Section to show their previously discussed limitations with respect to voltage and power ratings. Table 5.3 gives an overview of commercially available power converters for medium-voltage high-power applications.

**Table 5.3:** Ratings of commercially available power converters for medium-voltage high-power application.

Name	Voltage	Power	Topology	Front-end	Manufacturer
Sinamics SM150	3.3 kV	26.7 MVA	3-level NPC	AFE	SIEMENS [75]
MV7000	10 kV	26.7 MVA	3-level NPC	AFE	GE [76]
MV7000	10 kV	101 MVA	3-level NPC	DFE	GE [76]
MV7	13.8 kV	100 MW	5-level	AFE	GE [77]
TMdrive-XL85	7.2 kV	100 MW	5-level HNPC	DFE	TMEIC [78]
M2L 3000	7.2 kV	12 MVA	MMC	DFE	BENSHAW [61]
Sinamics Perfect Harmony GH150	11 kV	47 MVA	MMC	DFE	SIEMENS [79]

### 5.6.1 Details on the Individual Power Converters

The “Sinamics SM150” from Siemens is a 3-level NPC power converter and available for 3.3 kV, 26.7 MVA with an AFE (3-level NPC for bidirectional power flow). It utilizes IGCTs as semiconductor power switches and achieves an efficiency of 99 % [75].

The “MV7000” from GE is a 3-level NPC power converter and available for up to 10 kV, 26.7 MVA with an AFE, and therefore bidirectional power flow. A version that only allows for unidirectional power flow (i.e., that does not have an AFE but only DFE) is available for up to 10 kV, 101 MVA. The “MV7000” utilizes a series connection of IGBTs as semiconductor power switches and achieves an efficiency of up to 99 % [76].

The “MV7” from GE is a 5-level VSC with an AFE (bidirectional power flow) capable of 13.8 kV and up to 100 MW. It is, therefore, fully applicable for the operation of large synchronous generators in PSPPs. It uses a series connection of IGBTs to achieve the high blocking voltage [77, 80].

The “TMdrive-XL85” from TMEIC is a 5-level HNPC power converter and available for 7.2 kV, 100 MW (4 parallel 25 MW banks) with a DFE (no bidirectional power flow). The power converter has an efficiency of 98.6 % [78].

The “M2L 3000” from Benshaw is an MMC and available for 7.2 kV, 12 MVA with a DFE (no bidirectional power flow). It utilizes low-voltage (1.7 kV) IGBT power cells, and it achieves a converter system (DFE + transformer + MMC inverter stage) efficiency of 97 % [61].

The “Sinamics Perfect Harmony GH150” from SIEMENS is an MMC and available for 11 kV, 47 MVA with a DFE (no bidirectional power flow) [79].

### 5.6.2 Evaluation for Application in Large PSPPs

From the presented commercially available power converters, the “MV7” from GE fulfills the requirements for application in large PSPPs, particularly the medium-voltage rating of  $\geq 13.5$  kV and the bidirectional power flow.

The MMC topologies “M2L 3000” and “Sinamics Perfect Harmony GH150” are promising as well, even though they do not meet the aforementioned requirements. As the MMC topology is not limited to a specific voltage and power level it can be adjusted to meet the requirements. The challenges with MMCs for use in drive applications, i.e., the start-up and low-frequency operation of the motor side, have already been addressed for these power converters.

The 3-level NPC VSC ([75, 76]) and the 5-level HNPC VSC ([78]) are the common power converter topologies used in industrial applications. They are conventionally limited to 4.16 kV and 7.2 kV, respectively without a series connection of power semiconductor devices and thus not suitable for application in large PSPPs.

At the time of writing, the MMMC topology is not commercially available.

## 5.7 Summary of Power Converter Topologies for Application in Large PSPPs

The power converter operation of large PSPPs refers to a medium-voltage ( $\geq 13.5$  kV) high-power ( $\geq 100$  MW) bidirectional power flow application. This cannot be easily achieved with today's commercially available power converter topologies. The topologies commonly used for industrial medium-voltage drives are the 3-level NPC VSC and the 5-level HNPC VSC which cannot achieve the required operating voltage without a series connection of semiconductor power switches. In addition, the DC-link is often supplied by multi-pulse diode rectifiers which do not allow for bidirectional power flow.

The MMC and the MMMC do allow for bidirectional power flow and can be adopted to high operating voltages because of their modular structure consisting of a single building block. Particularly, the MMC is identified as suitable topology for application in large PSPPs because of its operational behavior. Due to the high number of voltage levels, i.e., 15 levels for the MMC presented in Chapter 6, the total harmonic distortion as well as the  $du/dt$  of the voltage waveforms supplied to the motor-generator are very small and thus, the potential additional stress on the synchronous machine at FSC operation is possibly negligible.



# Chapter 6

## Analysis of the Modular Multilevel Converter for Application in Large Pumped Storage Power Plants

*This Chapter analyzes the modular multilevel converter topology and describes its components as well as the characteristic voltage waveforms. For further investigation, a pulse width modulation voltage waveform generation tool, a simulation model, as well as an analytic average loss model are presented. These are used to compute the total harmonic distortion of the output voltage waveforms, the switching frequency of the semiconductor power devices, and the efficiency of the modular multilevel converter during operation.<sup>1</sup>*

### 6.1 Analysis of the Modular Multilevel Converter - Tools

#### 6.1.1 Model Parameters of the MMC

The modular multilevel converter (MMC) has been identified as a promising power converter topology for operation of synchronous motor-generators in large pumped storage power plants in Section 5.5.1. This Section describes the parameters of the MMC that are used for modeling a single DC-AC stage, see Figure 6.1.

The IGBT-module “FZ800R33KF2C” from Infineon [81] is used for this analysis. The overall findings do not change with a different module, because the detailed design with all the power loss in the inductors and capacitors is beyond the scope of this

---

<sup>1</sup>Selected material of this Chapter has also been published in [33] and [34].

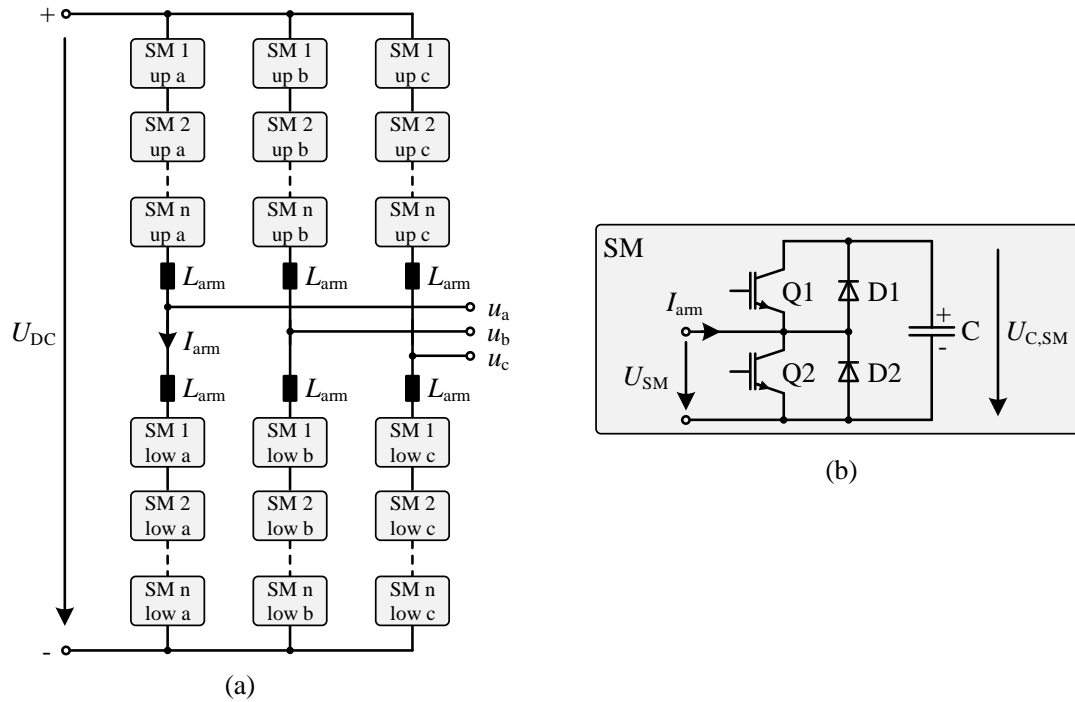


**Figure 6.1:** Modular multilevel converter: (a) topology for DC-AC conversion and (b) half-bridge submodules.

thesis. The IGBT-module has a maximum collector-emitter voltage of  $U_{CES} = 3.3$  kV, of which 50% are used during normal operation, see Section 5.2, thus 1.65 kV. The number of submodules  $n$  required to block the DC-link voltage of  $U_{DC} = 24$  kV necessary for a machine voltage of 13.5 kV line-to-line is determined as

$$n = \frac{U_{DC}}{U_{CES} \cdot 0.5}. \quad (6.1)$$

For the here investigated case, it is

$$n = \frac{U_{DC}}{U_{CES} \cdot 0.5} = \frac{24 \text{ kV}}{1.65 \text{ kV}} = 14.5. \quad (6.2)$$

Next, the IGBT has a maximum continuous DC collector current  $I_C$  of 1300 A and 800 A at 25 °C and 80 °C, respectively. To carry the rated phase current of the synchronous generator of  $I_{ph} = 5.77$  kA,  $n_{IGBT}$  IGBTs in parallel are required (rather than one single IGBT):

$$n_{IGBT} = \frac{I_{ph}}{I_C}. \quad (6.3)$$

Estimating from the data-sheet  $I_C = 1.05 \text{ kA}$ , it is

$$n_{\text{IGBT}} = \frac{I_{\text{ph}}}{I_C} = \frac{5.77 \text{ kA}}{1.05 \text{ kA}} = 5.5. \quad (6.4)$$

For the implemented MMC simulation model, the number of submodules per arm  $n$  is 14, which leads to a 15-level phase voltage waveform, and the number of IGBTs in parallel  $n_{\text{IGBT}}$  is 6. It is assumed that the 6 IGBT-modules are turned on and off simultaneously and carry the same current.

### 6.1.2 Objectives for the MMC Analysis Tools

The values of interest of the MMC are as follows:

- The total harmonic distortion (THD) of the output voltage waveforms  $U_{\text{ph,MMC}}$ .
- The switching frequency  $f_s$  of the semiconductor power switches.
- The efficiency of the DC-AC stage of the MMC  $\eta_{\text{DC-AC}}$ .

The THD on the machine side causes additional power loss in the synchronous motor-generator, and the THD on the grid side is subject to certain requirements of the grid code and should be  $\leq 5\%$  at the point of common coupling (PCC) for the phase voltage [82]. The actual switching frequency of each individual semiconductor power device is of interest, since for high-power applications the switching frequency should be  $f_s \leq 1000 \text{ Hz}$  to reduce the switching power loss and the stress on the semiconductor power switches. For full-size converter operation of large hydropower generators, the total efficiency of the MMC reduces the overall efficiency of the power plant, since it is in operation all the time, see Section 2.4.

### 6.1.3 MMC PWM Voltage Waveform Generation Tool

#### Implementation

The MMC pulse width modulation (PWM) voltage waveform generation tool implemented in MATLAB uses triangle-shaped carrier signals to enable a level-shifted carrier modulation [58] and the parameters identified in Section 6.1.1. Figure 6.2 illustrates an example of a 5-level PWM utilizing 4 level-shifted carrier signals. If the reference signal (positive half-wave) is higher than the respective carrier signal, the corresponding voltage level is set to high (see lower graph in Figure 6.2). For the negative half-wave, the same procedure with negative signs is applied.

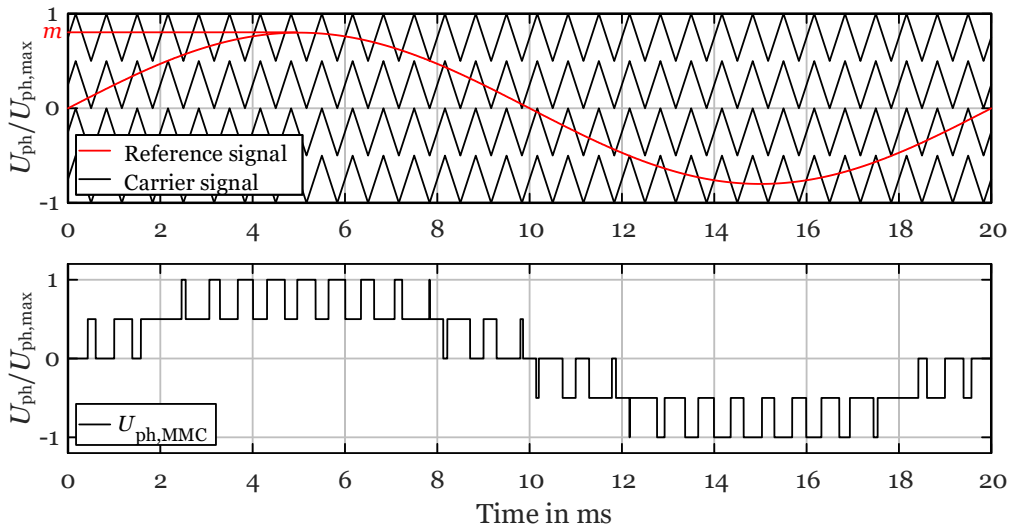
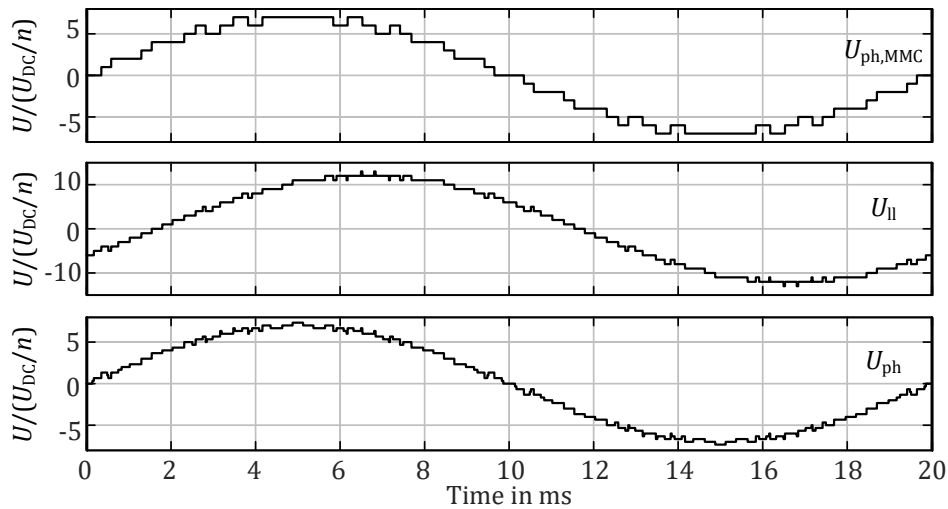


**Figure 6.2:** Reference signal, carrier signals, and corresponding output phase voltage waveform of a 5-level PWM.

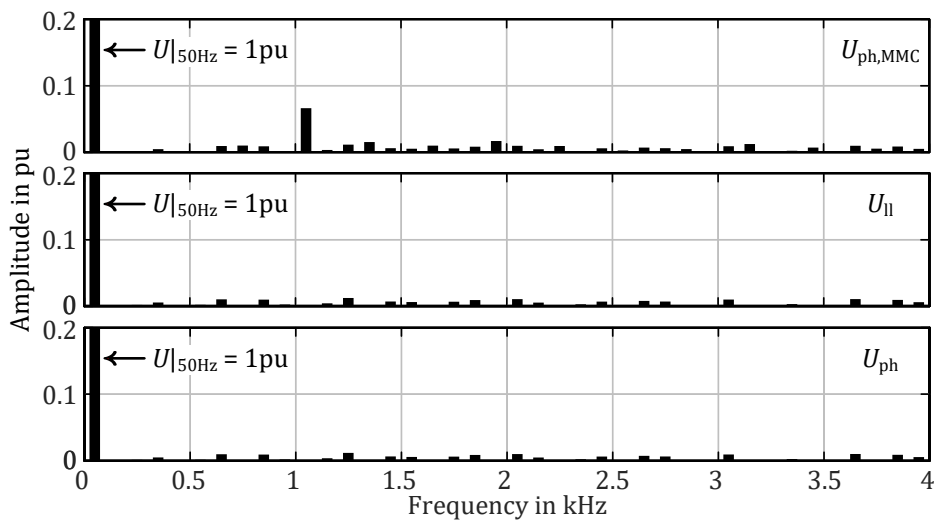
## Results

Figure 6.3 displays the computed waveforms utilizing the MMC PWM voltage waveform generation tool to represent a 15-level MMC suitable for supplying the synchronous motor-generators presented in Chapter 4 with a modulation index of  $m = 1$  (ratio between the peak value of the reference signal and the maximum value of the carrier signals, see Figure 6.2).  $U_{\text{ph,MMC}}$  is the phase voltage generated by the MMC.  $U_{\text{ll}}$  is the resulting line-to-line voltage applied to the synchronous machine.  $U_{\text{ph}}$  is the phase voltage at the synchronous machine terminals which results from a superimposition of  $U_{\text{ll}}$  and the floating neutral point of the synchronous machine with respect to the ground. This neutral-to-ground voltage is also referred to as common-mode voltage. This common-mode voltage causes additional stress for the motor winding [48] as well as bearing currents [83]. Strategies for mitigating this common-mode voltage are well described in [48].

Figure 6.4 shows the harmonic spectra derived by discrete Fourier transform of the voltage waveforms presented in Figure 6.3 for a 15-level MMC. The carrier frequency of  $f_c = 1050$  Hz is the only dominant peak in the harmonic spectrum of  $U_{\text{ph,MMC}}$  which is very low due to the multilevel topology. The carrier frequency has been chosen because it can be divided by three and hence, due to the three-phase transmission, it is no longer present in  $U_{\text{ll}}$ . Figure 6.4 shows that the harmonic spectrum of  $U_{\text{ph}}$  provided by a 15-level MMC has almost no harmonic content.



**Figure 6.3:** Computed voltage waveforms for a 15-level MMC for a carrier frequency of 1050 Hz: phase voltage of the MMC, line-to-line voltage at the motor supply line, and phase voltage at the machine terminals.



**Figure 6.4:** Computed voltage harmonics for a 15-level MMC for a carrier frequency of 1050 Hz: phase voltage of the MMC, line-to-line voltage at the motor supply line, and phase voltage at the machine terminals.

## Post-Processing

From this computed harmonic content the THD can be derived as follows [84]:

$$THD = \frac{\sqrt{\sum_{v=2}^{v_{\max}} U_v^2}}{U_1}, \quad (6.5)$$

where,  $v$  is the harmonic order,  $U_v$  is the magnitude of the individual harmonic, and  $U_1$  is the magnitude of the fundamental voltage. As per [82], harmonics up to  $v_{\max} = 50$  are taken into account for the computation of the THD.

### 6.1.4 Simulation Model of the MMC for Analysis of the Switching Behavior

To compute the switching power loss of the MMC, the switching frequency of the individual semiconductor power switches is required. The sinusoidal PWM waveform does not directly transfer to a switching procedure of the individual submodules, because the voltage levels of the MMC result from the combination of upper and lower arm submodules, and thus several combinations may be chosen. Hence, a certain switching state requires a certain amount of submodules being inserted within one arm. But the choice of the specific submodules can be used for the capacitor voltage balancing [58]. Therefore, the individual submodules of the MMC, and also the semiconductor power devices, have different individual switching frequencies. Hence, certain submodules are turned on and off more often than others. Investigating all the individual semiconductor power devices in the MMC, the maximum switching frequency  $f_{s,\max}$  that occurs during operation as well as the average switching frequency  $f_s$  can be derived. Note, that the average switching frequency  $f_s$  is not linked to the carrier frequency but depends on the utilized capacitor voltage balancing control scheme which can be used to reduce  $f_s$  [85]. As per [86], it is even possible to reduce  $f_s$  further while keeping the magnitude of the capacitor voltage ripple  $\Delta U_{C,SM}$ .

#### Implementation

To analyze the switching behavior of the submodules, a model of a single DC-AC conversion stage of a 15-level MMC with the parameters identified in Section 6.1.1 has been implemented in MATLAB / Simulink. It utilizes ideal models for the IGBTs

with anti-parallel diodes. The DC-link is modeled with an ideal voltage source. A three-phase series RLC load is used to set the desired apparent power. As stated in Section 5.5.1, a proper capacitor voltage balancing control is critical for the MMC operation and was implemented in the MATLAB / Simulink model of the MMC.

## Results

Figure 6.5 depicts the capacitor voltages of the upper arm submodules of phase a under load with implemented capacitor voltage balancing control.

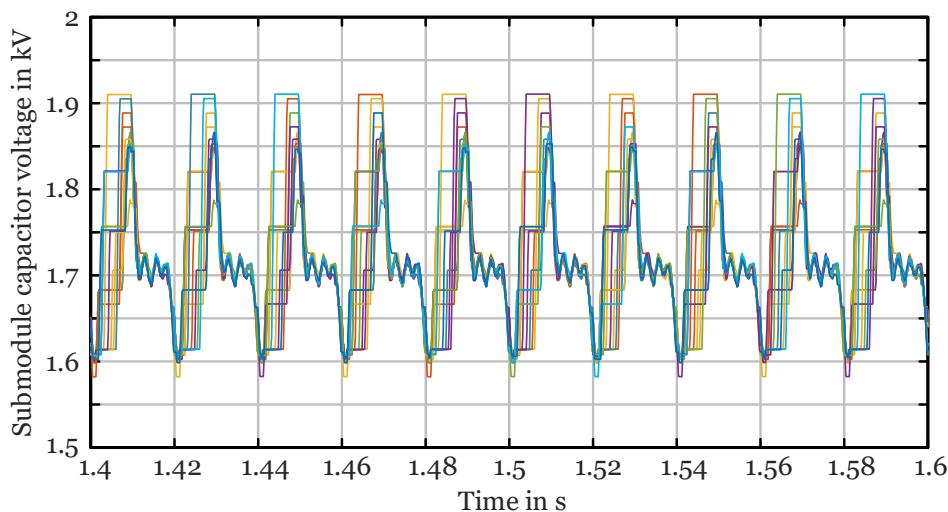


**Figure 6.5:** Capacitor voltages of the 14 submodules of the upper arm of phase a with capacitor voltage balancing implemented in the MMC simulation model, nominal load.

The capacitor voltages of the submodules  $U_{C,SM}$  (see Figure 6.1) shown in Figure 6.5 spread over a certain band with  $\Delta U_{C,SM} = 330$  V. The size (capacity) of the submodule capacitors is a design criteria of the MMC and is selected to meet a desired capacitor voltage ripple for nominal load operation, see Section 5.5.1. The voltage does not drift over time, and each submodule voltage remains in the same voltage band.

## Post-Processing

From the switching patterns of the individual semiconductor power switches the average switching frequency  $f_s$  can be derived, which can be used to compute the

switching power loss of the MMC during operation utilizing the analytic average loss model presented in the next Section.

### 6.1.5 Analytic Average Loss Model of the MMC

The analytic average loss model allows computing the efficiency of the two single DC-AC stages of the MMC for both rectifier and inverter modes. Note that for turbine operation of the synchronous motor-generator, the motor-side DC-AC conversion stage operates in rectifier mode, while for pumping operation, the motor-side DC-AC conversion stage operates in inverter mode.

#### Implementation

The calculation method for the analytic average loss model described in [16] has been implemented in MATLAB using the parameters identified in Section 6.1.1.

Note that this calculation approach does not depend on the output frequency  $f$  of the MMC but on the average switching frequency of the IGBT-modules  $f_s$ , which is derived from the simulation model of the MMC implemented in MATLAB / Simulink, see Section 6.1.4.

The analytic average loss model of the MMC is reviewed in Appendix D. It utilizes average currents through the individual semiconductor power devices, assuming sinusoidal waveforms [16], to compute the on-state power loss  $P_{\text{on}}$  as well as the switching power loss  $P_s$ . The former requires the output characteristics of the IGBT and the diode given in the data-sheet. The latter requires the turn-on and turn-off energy loss per pulse of the IGBT and the reverse recovery energy of the diode, which are also given in the data-sheet.

#### Post-Processing

The total power loss of a single DC-AC conversion stage of the MMC  $P_{\text{d,DC-AC}}$  is computed with

$$P_{\text{d,DC-AC}} = P_{\text{on}} + P_s. \quad (6.6)$$

Note that for the presented power loss evaluation the passive components (submodule capacitors and arm inductors) are neglected.

The efficiency of a single DC-AC conversion stage of the MMC  $\eta_{DC-AC}$  results from  $P_{d,DC-AC}$  and the active power  $P$  delivered:

$$\eta_{DC-AC} = \frac{P - P_{d,DC-AC}}{P}. \quad (6.7)$$

The total efficiency of the MMC  $\eta_{MMC}$  results from the product of one DC-AC conversion stage operating as a rectifier and one DC-AC conversion stage operating as an inverter:

$$\eta_{MMC} = \eta_{DC-AC,rectifier} \cdot \eta_{DC-AC,inverter}. \quad (6.8)$$

## 6.2 Analysis of the Modular Multilevel Converter - Results

### 6.2.1 Analysis of the THD of the MMC

Figure 6.6 shows the computed PWM phase voltages for the 15-level MMC for 50 Hz and 100 Hz, respectively. At constant carrier frequency  $f_c$  the number of step changes per period becomes smaller for a higher frequency, which has a negative influence on the THD.

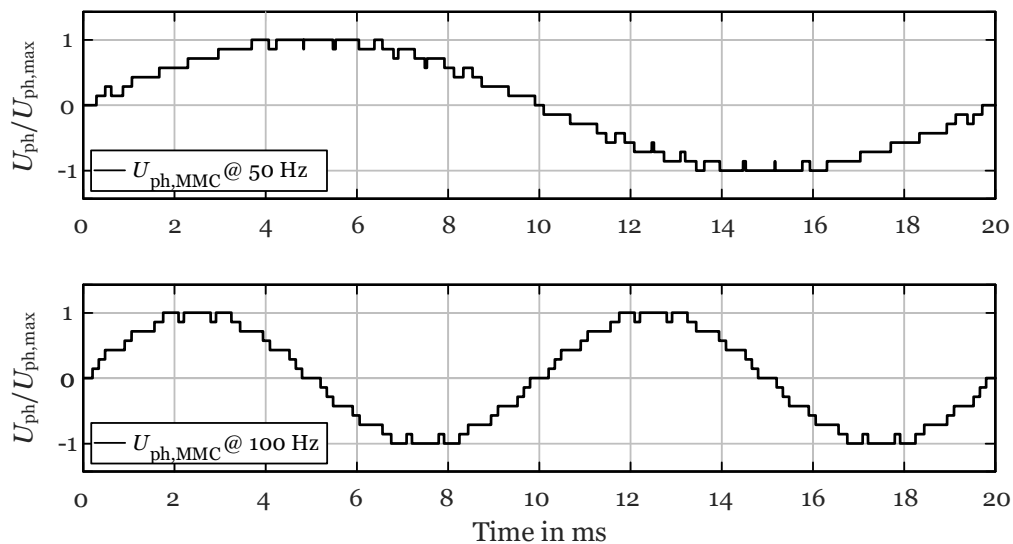


**Figure 6.6:** 15-level MMC phase voltages for operation at 50 Hz and 100 Hz at constant carrier frequency.

Table 6.1 shows the computed THD for the phase voltage of the MMC  $U_{\text{ph,MMC}}$ , the line-to-line voltage  $U_{\text{ll}}$ , and the phase voltage at the machine terminals  $U_{\text{ph}}$  up to the 50<sup>th</sup> order, see (6.5), for operating frequencies  $f$  of 25 Hz, 50 Hz, and 100 Hz. In contrast to the earlier analyses, the carrier frequency for the analysis presented in this Section is set to  $f_c = 1500$  Hz, since  $f_c$  is typically an integer multiple of the operating frequency  $f$  and needs to be divisible by three. Therefore, the carrier frequency of  $f_c = 1050$  Hz used throughout this Chapter would not meet the criteria because of the analysis of operating frequencies including  $f = 100$  Hz. For constant carrier frequency  $f_c$ , the THD increases with the operating frequency  $f$ .

However, the values of the THD of the MMC are extremely low in general. Section 8.2.2 shows that no additional power consumption (which could be attributed to additional power loss) is measured at the machine terminals of a synchronous machine when operating at an MMC supply compared to a purely sinusoidal supply.

**Table 6.1:** THD of the phase voltage of the MMC  $U_{\text{ph,MMC}}$ , the line-to-line voltage  $U_{\text{ll}}$ , and the phase voltage at the machine terminals  $U_{\text{ph}}$  at constant carrier frequency for operating frequencies of 25 Hz, 50 Hz, and 100 Hz.

$f$ Hz	$f_c$ Hz	THD( $U_{\text{ph,MMC}}$ ) %	THD( $U_{\text{ll}}$ ) %	THD( $U_{\text{ph}}$ ) %
25	1500	1.90	1.31	1.31
50	1500	6.51	2.81	2.81
100	1500	7.63	2.93	2.92

## 6.2.2 Analysis of the Efficiency of the MMC at Nominal Load

Utilizing the MMC simulation model presented in Section 6.1.4, the maximum switching frequency  $f_{s,\text{max}}$  as well as the average switching frequency  $f_s$  of the semiconductor power devices can be determined, where  $f_s = 300$  Hz  $\pm$  5 %. Therefore, in the following analysis the average switching frequency is kept constant at  $f_s = 300$  Hz.

Table 6.2 shows the computed power loss distribution and the efficiency for the single DC-AC stages of the MMC for a 135 MW, 50 Hz,  $\cos \varphi = 1$  MMC operating with a carrier frequency of  $f_c = 1050$  Hz in inverter (I) and rectifier (R) modes.

**Table 6.2:** Maximum switching frequency, average switching frequency, power loss distribution, and efficiency of the single DC-AC stages of the MMC for 50 Hz nominal load inverter and rectifier operation.

Mode	$P$	$\cos \varphi$	$f$	$f_c$	$f_{s,\max}$	$f_s$	$P_{\text{on}}$	$P_s$	$\eta_{\text{DC-AC}}$
-	MW	-	Hz	Hz	Hz	Hz	kW	kW	%
I	135	1.00	50	1050	360	300	1135	312	98.93
R	135	1.00	50	1050	360	300	1047	312	98.99

Table 6.2 also shows the on-state power loss  $P_{\text{on}}$ , the switching power loss  $P_s$ , and the efficiency of a single DC-AC conversion stage  $\eta_{\text{DC-AC}}$  for inverter and rectifier modes at nominal load which are computed utilizing the analytic average loss model presented in Section 6.1.5. For these computations, the average switching frequency  $f_s$  is used.  $P_s$  is the same for both inverter and rectifier modes, since  $f_s$  is constant.  $P_{\text{on}}$  differs by approximately  $\pm 4\%$  because of the different current distributions between the semiconductor power devices in inverter and rectifier modes and the different output characteristics of the IGBTs and the diodes. This results in a slightly increased efficiency in rectifier mode by 0.06 percentage points for a single DC-AC conversion unit. This power loss distribution and therefore, the difference in efficiency of the inverter and the rectifier stage, of course, depends on the utilized IGBT-modules.

### 6.2.3 Efficiency of the Full-Size Converter and the Synchronous Motor-Generator at Nominal Load and Partial Load

#### Efficiencies of the Suggested Motor-Generator, the Full-Size Converter, and the Overall System

Table 6.3 shows the computed efficiencies of the suggested synchronous motor-generator design for FSC operation presented in Section 4.7 (138 MVA, 60 Hz, 200 rpm,  $\cos \varphi = 0.98$ ), of the FSC comprising two single MMC DC-AC stages, as well as of the FSC operated synchronous motor-generator for nominal and partial load operation, both for turbine (T) and pumping (P) modes. The individual efficiencies of the two single MMC DC-AC stages, see Figure 5.7, and their modes of operation, namely inverter mode (I) and rectifier mode (R), are listed as well. The grid-side MMC

**Table 6.3:** Computed efficiencies of the suggested SG and the FSC (comprising two MMC stages) for nominal load and partial load operation of the PSPP.

	Operating point	T100	T75	T50	P100	P75	P50
PSPP	Mode of operation	T	T	T	P	P	P
	Load in pu	1.00	0.75	0.50	1.00	0.75	0.50
SG ( $\cos \varphi = 0.98$ )	$U$ in pu	1.00	1.00	1.00	1.00	0.91	0.79
	$f$ in Hz	60	60	60	60	54.5	47.6
	$\eta$ in %	99.14	99.05	98.77	99.14	99.11	99.05
Machine-Side MMC ( $\cos \varphi = 0.98$ )	Mode	R	R	R	I	I	I
	$U$ in pu	1.00	1.00	1.00	1.00	0.91	0.79
	$f$ in Hz	60	60	60	60	54.5	47.6
	$\eta$ in %	98.97	99.07	99.18	98.91	98.92	98.92
Grid-Side MMC ( $\cos \varphi = 0.9$ )	Mode	I	I	I	R	R	R
	$U$ in pu	1.00	1.00	1.00	1.00	1.00	1.00
	$f$ in Hz	50	50	50	50	50	50
	$\eta$ in %	98.81	98.93	99.07	98.88	98.98	99.11
FSC	$\eta$ in %	97.79	98.01	98.26	97.80	97.91	98.04
SG+FSC	$\eta$ in %	96.95	97.08	97.05	96.96	97.04	97.11

operates with a power factor of 0.9 to supply reactive power to the grid, as would be the case for a conventional directly line-connected synchronous machine in PSPPs.

Preliminary studies have shown, that the increase of the SG's efficiency, when designing the SG for a power factor of 0.98 under-excited compared to unity power factor, outweigh the reduction of the motor-side MMC's efficiency caused by the increased current at power factor 0.98 compared to unity power factor. Hence, operating the SG at a power factor of 0.98 results in an overall efficiency improvement of the system comprising SG and FSC in this particular analysis.

The efficiency of the SG decreases by 0.37 percentage points for partial load operation at half the nominal load in turbine mode. The efficiency reduction is less pronounced in pumping mode due to  $U \sim f$  operation, hence 0.09 percentage points at half the nominal load. The efficiency of the FSC increases by 0.47 percentage

points for partial load operation at half the nominal load in turbine mode and increases by 0.24 percentage points for partial load operation at half the nominal load in pumping mode. Therefore, the overall efficiency including both the SG and the FSC (SG+FSC) increases slightly for partial load operation, namely 0.10 percentage points for partial load operation at half the nominal load in turbine mode and 0.15 percentage points for partial load operation at half the nominal load in pumping mode.

### Comparison with the Conventional Directly Line-Connected Synchronous Motor-Generator

Table 6.4 shows the computed efficiencies of the FSC operated SG from Table 6.3 (SG+FSC) and of the conventional directly line-connected synchronous motor-generator presented in Section 4.1 (150 MVA, 50 Hz, 200 rpm,  $\cos \varphi = 0.9$ ) for nominal and partial load operation for turbine mode (T) and nominal load operation in pumping mode (P) (see Figure 2.3 for the conventional fixed-speed PSPP topology).<sup>2</sup>

**Table 6.4:** Computed efficiencies of the suggested SG and the FSC (comprising two MMC stages) for nominal load and partial load operation of the PSPP.

	Operating point	T100	T75	T50	P100
PSPP	Mode of operation	T	T	T	P
	Load in pu	1.00	0.75	0.50	1.00
SG+FSC	$\eta$ in %	96.95	97.08	97.05	96.96
Line-Connected SG	$\eta$ in %	98.87	98.81	98.57	98.87
	$\Delta\eta$ in %-points	-1.92	-1.73	-1.52	-1.91

The FSC operated SG has a smaller overall efficiency compared to the directly line-connected SG, namely -1.92 percentage points in turbine mode and -1.91 percentage points in pumping mode. The efficiency of the conventional directly line-connected SG decreases by 0.30 percentage points for partial load operation at half the nominal load in turbine mode. Since the efficiency of the FSC operated SG is quite constant for

<sup>2</sup>It is not possible to operate the conventional directly line-connected synchronous motor-generator at partial load in pumping mode because of the fixed frequency.

partial load operation, the difference in efficiency between these two topologies  $\Delta\eta$  decreases for partial load operation, namely from -1.92 percentage points to -1.52 percentage points at half the nominal load in turbine mode.

### 6.3 Summary

With the tools created to analyze the operational behavior of the MMC operating as an FSC supplying large synchronous motor-generators in PSPPs, the THD, the switching frequency, and the efficiency can be computed. The THD increases with increased operating frequency at constant carrier frequency. However, the values of the THD of the MMC are extremely low in general (i.e., the THD of the line-to-line voltage is  $< 3\%$  for the example presented in Table 6.1).

The individual switching frequency of the semiconductor power devices needs to be evaluated utilizing the MMC simulation model, since the PWM voltage waveform does not directly transfer to the switching states of the submodules. With the resulting average switching frequency of the semiconductor power devices, the efficiency of the individual DC-AC stages of the MMC (machine-side and grid-side) can be computed utilizing the analytic average loss model. For the MMC, the efficiency increases for partial load operation which counteracts the reduced efficiency of the synchronous motor-generator at partial load operation, see Table 6.3. Hence, the efficiency of the overall system comprising synchronous motor-generator and FSC increases slightly for partial load operation, i.e., it increases by 0.10 percentage points in turbine mode and by 0.15 percentage points in pumping mode at half the nominal load compared to nominal load.

Compared to the conventional directly line-connected synchronous machine, the overall efficiency of the FSC operated synchronous machine is 1.92 percentage points lower at nominal load, see Table 6.4. However, it is not possible to realize partial load operation in pumping mode with the conventional directly line-connected synchronous motor-generator. However, this mode of operation is required to also participate in the balancing energy market and thus, increasing the earnings of the PSPP, which is enabled by a variable-speed technology like the FSC operated synchronous motor-generator.

# Chapter 7

## Damper Winding Harmonics Analysis at Full-Size Converter Supply - Techniques

*The damper winding is subject to the additional harmonics in the air-gap field when operating the synchronous motor-generator with a full-size converter. This Chapter describes the test bench setup for measuring the harmonic content of a custom-built electrically excited synchronous machine during operation. With this aim, the machine can be supplied by various voltage waveforms of typical power converter topologies via a power amplifier. The three different voltage waveforms chosen for the analysis are presented in this Chapter as well. Next, the shielding and the damping effects of the two damper circuits (i.e., the built-in damper cage and the solid rotor) are analyzed numerically using a two-dimensional finite element analysis by assessing the induced voltage in the field winding. These results are then compared to the experimental results obtained from the test bench.<sup>1</sup>*

### 7.1 Test Bench Setup

A custom-built electrically excited synchronous machine (SM) is mounted on a test bench to analyze the harmonic content during operation when the machine is supplied by various power converter topologies simulated with a power amplifier. Figures 7.1 and 7.2 show the test bench setup, the motor geometry is displayed in Figure 7.3, and selected machine parameters are provided in Table 7.1. More details on the utilized equipment and the measurement system can be found in Appendix E.

---

<sup>1</sup>Selected material of this Chapter has also been published in [87].

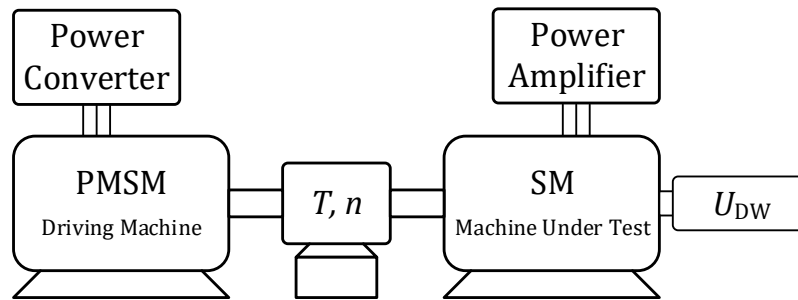


**Figure 7.1:** Block diagram of the test bench for evaluation of the damper bar voltages (PMSM = Permanent Magnet Synchronous Machine, SM = custom-built electrically excited Synchronous Machine).

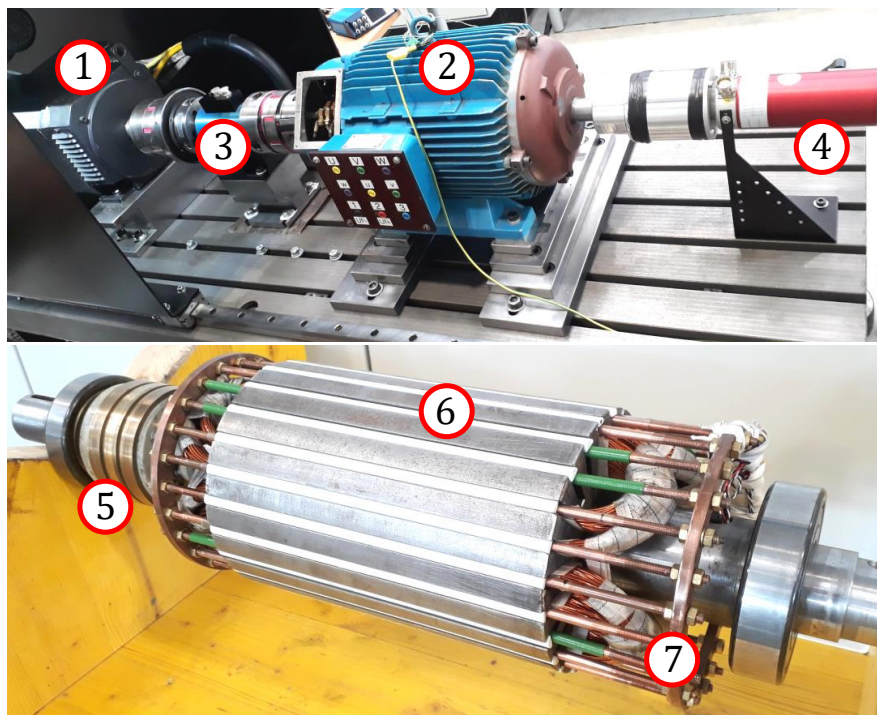


**Figure 7.2:** Test bench for evaluation of the damper bar voltages (1 = PMSM = Permanent Magnet Synchronous Machine, 2 = SM = custom-built electrically excited Synchronous Machine, 3 = torque measurement system, 4 = slip ring transducer, 5 = slip rings for excitation, 6 = solid rotor, and 7 = damper winding = built-in damper cage).

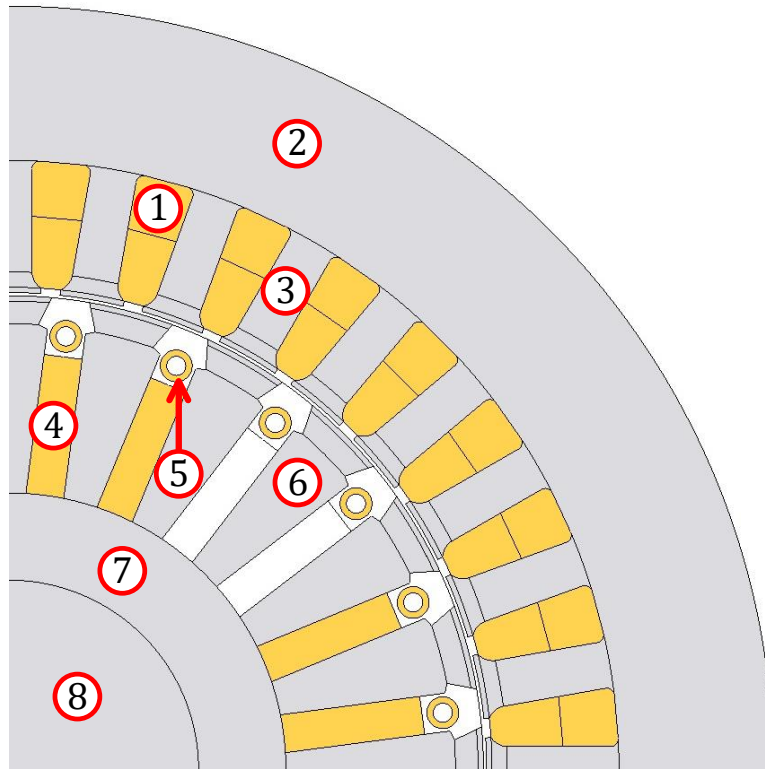


**Figure 7.3:** Geometry of the SM utilized for the 2D-FEA full model (1 = two-layer stator winding, 2 = stator yoke, 3 = stator teeth, 4 = field winding, 5 = damper winding, 6 = rotor teeth, 7 = rotor yoke, 8 = shaft).

**Table 7.1:** Selected parameters of the custom-built electrically excited SM.

$T$	$U_{ll}$	$f$	$n$	$p$	$d$	$l$	$\delta$	$Q_s$	$Q_r$
Nm	V	Hz	rpm	-	mm	mm	mm	-	-
25	230	50	1500	2	150	216	0.5	36	24

The SM allows the voltage drops to be measured at six damper bars corresponding to one pole of the four-pole machine. The voltage drops are transmitted to the measurement system via the slip ring transducer. To accommodate the modular damper cage in the rotor, the electromagnetic utilization of the SM under test is much smaller compared to standard machines of the same size. Hence, the machine operates at a reduced voltage of  $U_{ll} = 230$  V (instead of  $U_{ll} = 400$  V). However, this does not affect the measurement results.

Measurements for the electrical and mechanical quantities of the SM are implemented at the test bench as well, namely the stator phase voltages  $U_{ph}$ , the stator

currents  $I_{ph}$ , the field current  $I_f$ , the rotational speed  $n$ , as well as the torque  $T$ . A permanent magnet synchronous machine (PMSM) drives the SM via the torque measurement system and can also be used to apply a load to the SM. The data are collected with a DEWE-5000 measurement system. Both the driving PMSM and the power amplifier are easily capable of powering the custom-built SM under nominal load conditions.

## 7.2 Theoretical Analysis of the Synchronous Machine's Harmonics

The harmonic content present in the SM's windings results from a combination of the harmonics caused by both the machine geometry itself and the full-size converter supply. Therefore, the SM's harmonic content will be analyzed both for a purely sinusoidal supply as well as for an FSC supply. For the latter, two different power converter topologies are investigated.

### 7.2.1 Harmonics Caused by the Synchronous Machine's Geometry

The stator magnetomotive force (mmf) harmonic orders can be computed utilizing [39]:

$$\nu = 1 + 2 \cdot m \cdot g, \quad (7.1)$$

where  $m$  is the number of phases and  $g = 0, \pm 1, \pm 2, \pm 3$ , etc. Therefore, the harmonic orders of a three-phase winding are  $\nu = +1, -5, +7, -11, +13$ , etc. The sign of the ordinal number specifies the direction of the rotation of the corresponding wave, which can be either in positive or negative direction [39].

Especially for large hydropower generators, the stator slot harmonics and the rotor slot harmonics are decoupled from each other by a large air-gap. However, the custom-built SM under test has a very small air-gap  $\delta$  of only 0.5 mm and no skewed slots. It does have open rotor slots which vary the magnetic conductance along the circumference. These design features result in a somewhat worst-case more pronounced harmonic response. Hence, the harmonics are measurable, particularly in the damper winding. In addition, when exploiting additional generator design possibilities for full-size converter operation, particularly adjusting the requirement for the synchronous reactance, see Section 4.4, the air-gap becomes smaller compared

to a conventional directly line-connected synchronous motor-generator. Hence, the harmonic response behavior increases for the FSC operated synchronous motor-generator as well.

The slot harmonics for the stator and the rotor can be computed utilizing [39]:

$$\mu = 1 + \frac{Q}{p} \cdot g, \quad (7.2)$$

where  $Q$  is the number of slots,  $p$  is the number of pole pairs, and  $g = \pm 1, \pm 2, \pm 3$ , etc.

When the machine rotates with its synchronous speed, the slips for the higher harmonics can be computed utilizing [39]:

$$s_\nu = 1 - \nu. \quad (7.3)$$

Therefore, the harmonics -5, +7, -11, +13, and -17, +19, which result from (7.1) for a three-phase winding, transfer to the following slips:

$$s_{-5} = 6, s_{+7} = -6, s_{-11} = 12, s_{+13} = -12, s_{-17} = 18, s_{+19} = -18.$$

These harmonics should be present to certain extents in the SM during operation, which is discussed in Chapter 8.

## 7.2.2 Harmonics Caused by the Full-Size Converter Supply

For the investigated motor operation of the SM under test, the SM is supplied by a power amplifier which can generate arbitrary voltage waveforms. The voltage harmonics caused by the switching pattern and the level count of the different power converter topologies lead to additional harmonics in the SM's main stator winding and subsequently also in the different rotor windings.

### 15-Level Modular Multilevel Converter Supply

As stated in Section 5.5.1, the modular multilevel converter (MMC) is a good choice for medium-voltage ( $\geq 13.5$  kV) high-power ( $\geq 100$  MW) applications in pumped-storage power plants (PSPPs). This is because of its arbitrary scalability to higher voltages without the need of putting the semiconductor power switches directly in series. The resulting high level count for blocking the required voltage results in very smooth sinusoidal waveforms. Hence, the voltage stress for the motor winding insulation and the total harmonic distortion are extremely low, which should result in little to no difference for the SM during operation compared to a purely sinusoidal voltage supply. This aspect is investigated in Section 8.2.

Figure 7.4 displays the computed sinusoidal PWM scheme as it is applied to the SM at the test bench utilizing the power amplifier. Especially the phase voltage waveform at the machine terminals  $U_{ph}$  is very sinusoidal.

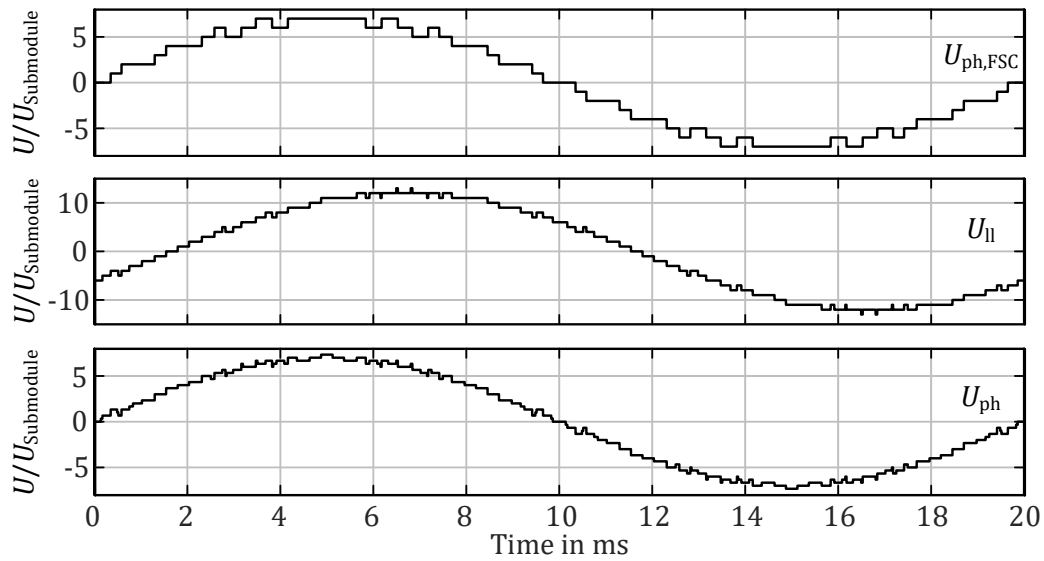
Figure 7.5 illustrates the harmonic spectra of the voltage waveforms presented in Figure 7.4. The carrier frequency of 1050 Hz is the only dominant peak in the harmonic spectrum of  $U_{ph,FSC}$ , which corresponds to the carrier frequency. The carrier frequency is purposely chosen to be 1050 Hz, as this is a multiple of three, and thus does not occur in  $U_{ll}$ . A different carrier frequency, however, such as 1000 Hz, would transfer directly to the machine terminals, as discussed in Section 6.1.3. The harmonic spectrum of  $U_{ph}$  provided by a 15-level MMC has almost no harmonic content.

### 3-Level Neutral Point Clamped Voltage Source Converter Supply

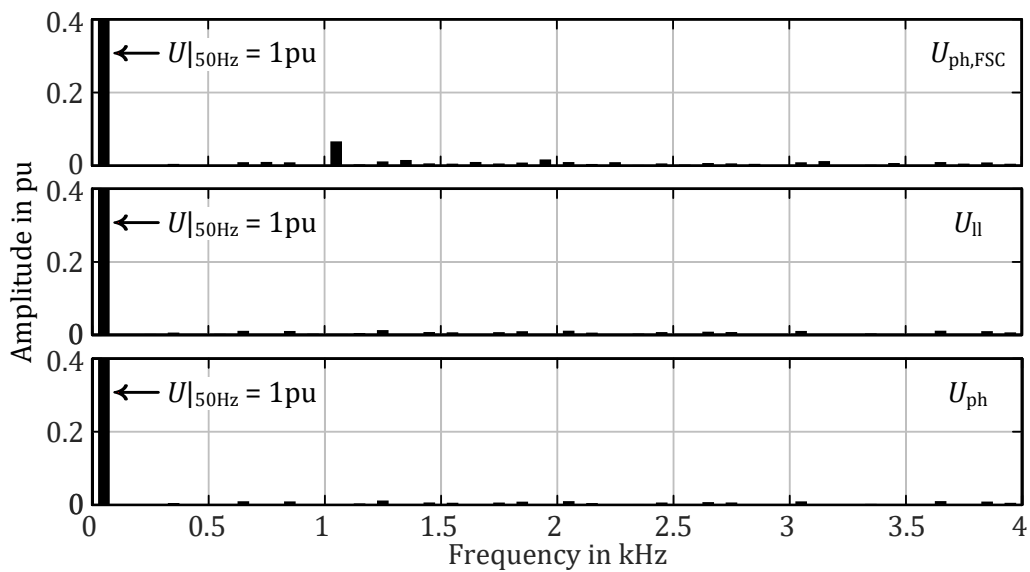
Although the 3-level NPC VSC is not commercially available for the medium-voltage high-power requirements for large PSPP applications ( $\geq 13.5$  kV and  $\geq 100$  MW), it is still the preferred power converter topology for traction applications. Without a series connection of semiconductor power devices, this topology is limited to 4.16 kV, see Section 5.3.1. Utilizing a series connection of devices, as realized by some manufacturers, could bring this state-of-the-art power converter topology for large drive applications close to the operating voltage requirements for large PSPPs, see Table 5.3. Therefore, the 3-level NPC VSC is chosen to represent the worst-case power converter topology for application in large PSPPs resulting in a quite stressful supply voltage waveform for a large synchronous hydropower generator.

Figure 7.6 displays the computed sinusoidal PWM scheme as it is applied to the test bench utilizing the power amplifier. Each phase of the 3-level NPC VSC can become  $U_{DC}/2$ , 0, or  $-U_{DC}/2$ , where  $U_{DC}$  is the DC-link voltage of the 3-level NPC VSC.  $U_{ll}$  comprises 5 levels while  $U_{ph}$  entails even 9 levels.

Figure 7.7 illustrates the harmonic spectra of the voltage waveforms presented in Figure 7.6. The carrier frequency of 1050 Hz is quite dominant in the harmonic spectrum of  $U_{ph,FSC}$ . However, due to the three-phase transmission, this dominant harmonic is no longer present in the line-to-line voltage at the supply line  $U_{ll}$ , nor in the phase voltage at the machine terminals  $U_{ph}$ .



**Figure 7.4:** Computed voltage waveforms for a 15-level MMC for a carrier frequency of 1050 Hz: simulated phase voltage of the power converter  $U_{ph,FSC}$ , resulting line-to-line voltage at the motor supply line  $U_{ll}$ , and phase voltage at the SM terminals  $U_{ph}$ .



**Figure 7.5:** Computed voltage harmonics for a 15-level MMC for a carrier frequency of 1050 Hz: simulated phase voltage of the power converter  $U_{ph,FSC}$ , resulting line-to-line voltage at the motor supply line  $U_{ll}$ , and phase voltage at the SM terminals  $U_{ph}$ .

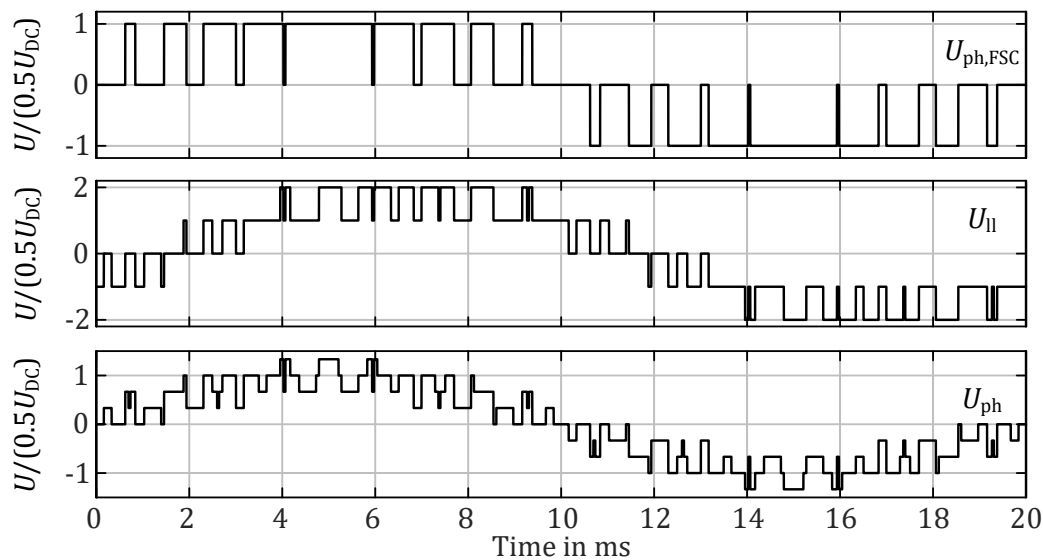


**Figure 7.6:** Computed voltage waveforms for a 3-level NPC VSC for a carrier frequency of 1050 Hz: simulated phase voltage of the power converter  $U_{ph,FSC}$ , resulting line-to-line voltage at the motor supply line  $U_{ll}$ , and phase voltage at the SM terminals  $U_{ph}$ .

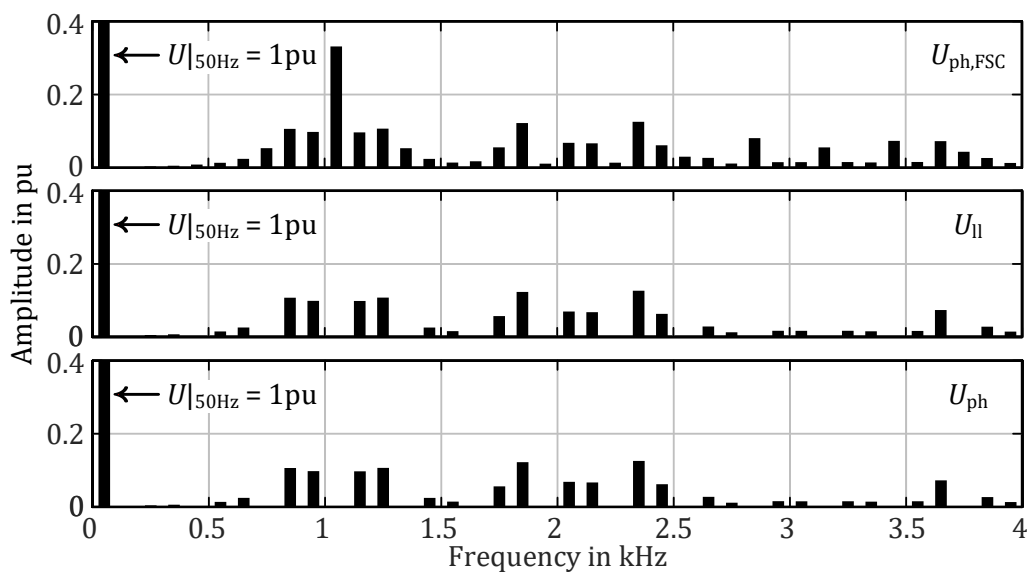


**Figure 7.7:** Computed voltage harmonics for a 3-level NPC VSC for a carrier frequency of 1050 Hz: simulated phase voltage of the power converter  $U_{ph,FSC}$ , resulting line-to-line voltage at the motor supply line  $U_{ll}$ , and phase voltage at the SM terminals  $U_{ph}$ .

## 7.3 Damper Winding Characterization

The rotor of the SM under test has two independent damper circuits. (See Figure 7.3 for the SM's geometry.)

- The first one is the built-in damper cage which consists of copper pipes screwed to a copper end ring on each side. The voltage induced in the damper winding is measured as voltage drops along these copper pipes. With this measurement system, the damper winding current distribution of one pole can be determined.
- The second damper circuit of the SM under test is the solid steel rotor. This rotor increases all damping effects of the built-in damper cage. The analysis given in [88] shows that the solid rotor can be described by a second individual damper circuit. The penetration depth, the electric conductivity of the material, and the dimensions are the most important parameters for computing the equivalent winding. According to [88], for small motors such as the SM under test, the equivalent winding resulting from the solid rotor has comparable parameters as the built-in damper cage. Such eddy currents, and hence damping effects, hardly occur with synchronous motor-generators in large PSPPs with a laminated rotor.

According to [89], the effects of an SM's damper winding should be analyzed for two operating points: The damper winding's shielding effect can be observed at standstill, while its damping effect can be analyzed when the machine operates close to the synchronous speed. The current distribution of the damper winding depends on the mmfs caused by all the other active windings.

In this Section, the damper winding's effectiveness is analyzed utilizing two-dimensional finite element analysis (2D-FEA) by supplying the machine with a symmetrical three-phase 50 Hz system at standstill. The 2D-FEA allows the two damper circuits to be deactivated, i.e., the built-in damper cage and the solid rotor, individually by either removing the built-in damper cage or disabling the eddy currents in the pole face of the solid rotor, respectively. Therefore, the damper circuit effectiveness can be evaluated for all combinations of active and inactive damper circuits. For this analysis, the custom-built damper cage is modeled assuming ideal conductivity of the copper end rings.

### 7.3.1 Damper Winding Shielding Effect Analysis

Table 7.2 shows the shielding effect of the two damper circuits, namely, the built-in damper cage and the solid rotor.

#### Only Built-In Damper Cage Active

The built-in damper cage alone decreases the induced voltage in the field winding  $U_f$  down to 61 %.

#### Only Solid Rotor with Eddy Currents Active

When the built-in damper cage is disabled, and the eddy currents in the solid rotor are enabled, i.e., the damper circuit due to the solid rotor,  $U_f$  decreases down to 66 %. In the 2D-FEA, it is assumed that the eddy currents flow uniformly in the axial direction along the entire machine's length. However, this is not the case in reality due to return points of the conductor loops at the ends of the machine. Hence, the 2D-FEA simulation neglects these end-effects, and the shielding effect caused by the eddy currents in the solid rotor is computed as larger than in reality. Thus, the true shielding effect of the solid rotor due to eddy currents is more pronounced than in reality.

#### Both Built-In Damper Cage and Solid Rotor Active

The induced voltage in the field winding  $U_f$  decreases down to 44 % when both damper circuits are active.

**Table 7.2:** Voltage induced in the field winding for the fundamental frequency at standstill of the synchronous machine.

2D-FEA model configuration		$U_f$
Built-in damper cage	Pole-face eddy currents	%
OFF	OFF	100
ON	OFF	61
OFF	ON	66
ON	ON	44

### Conclusion

The results obtained from 2D-FEA for standstill of the synchronous machine show that the built-in damper cage and the solid steel rotor have a similar shielding effect for the fundamental frequency.

### 7.3.2 Damper Winding Damping Effect Analysis

To visualize the damping effect for the higher harmonics, the SM operates close to its synchronous speed. For this investigation, the stator is fed with a symmetrical three-phase 50 Hz system, and the machine operates with a slip of  $s = 1/15 = 0.067$ , and therefore, 1400 rpm.

#### No Damper Circuits Active

Figure 7.8 shows the computed harmonic spectrum including the higher harmonics caused by the slots and the flux distribution due to the stator winding distribution. For this simulation, both damper circuits are disabled. Therefore, the higher harmonics are very present in comparison to the magnitude of the harmonic corresponding to the slip frequency of 3.33 Hz.

#### Only Built-In Damper Cage Active

Figure 7.9 shows the harmonic spectrum including the higher harmonics caused by the slots and the flux distribution due to the stator winding distribution when the built-in damper cage is enabled. In this case, the magnitudes of the higher harmonics are reduced by a factor of 10 for the 556.7 Hz - component and by a factor of 40 for the 1683.3 Hz - component when compared to Figure 7.8, where no damper circuit is enabled.

#### Only Solid Rotor with Eddy Currents Active

Figure 7.10 demonstrates that the slip frequency's magnitude decreases by about 19 % when only the eddy currents are enabled in the 2D-FEA, and therefore, the solid rotor becomes effective. The higher harmonics are not affected as much by the solid rotor as by the built-in damper cage, since the solid rotor's damper circuit consists of many separate conductor loops which are not connected directly to each other.

### Both Built-In Damper Cage and Solid Rotor Active

When both damper circuits are enabled, the largest magnitude of the higher harmonics is only about 5% of the slip frequency's magnitude, see Figure 7.11, which is in line with the experimental results obtained for this operating point, presented in Figure 7.12. The additional 100 Hz - component present in the measured harmonic spectrum in Figure 7.12 will be discussed in Section 8.1.2.

### Conclusion

The results obtained from 2D-FEA for rotation of the synchronous machine close to synchronous speed, i.e., 1400 rpm, show that the low-order harmonics are mainly reduced by the solid steel rotor while the higher-order harmonics are mainly reduced by the built-in damper cage.

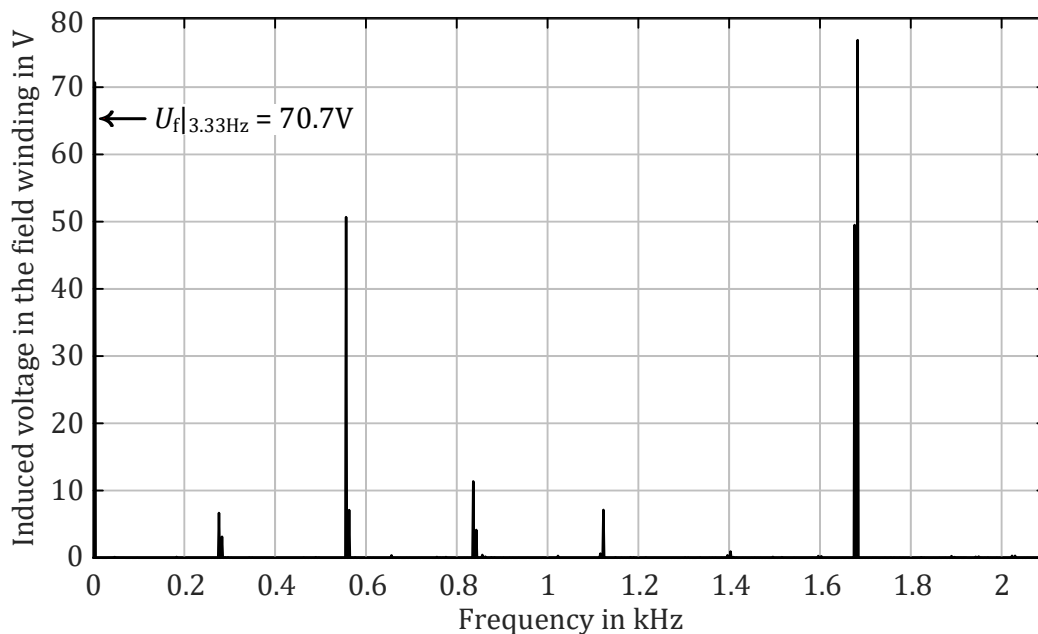


**Figure 7.8:** Simulated harmonic spectrum of the induced voltage in the field winding for operation of the SM at 1400 rpm when both damper circuits are disabled.

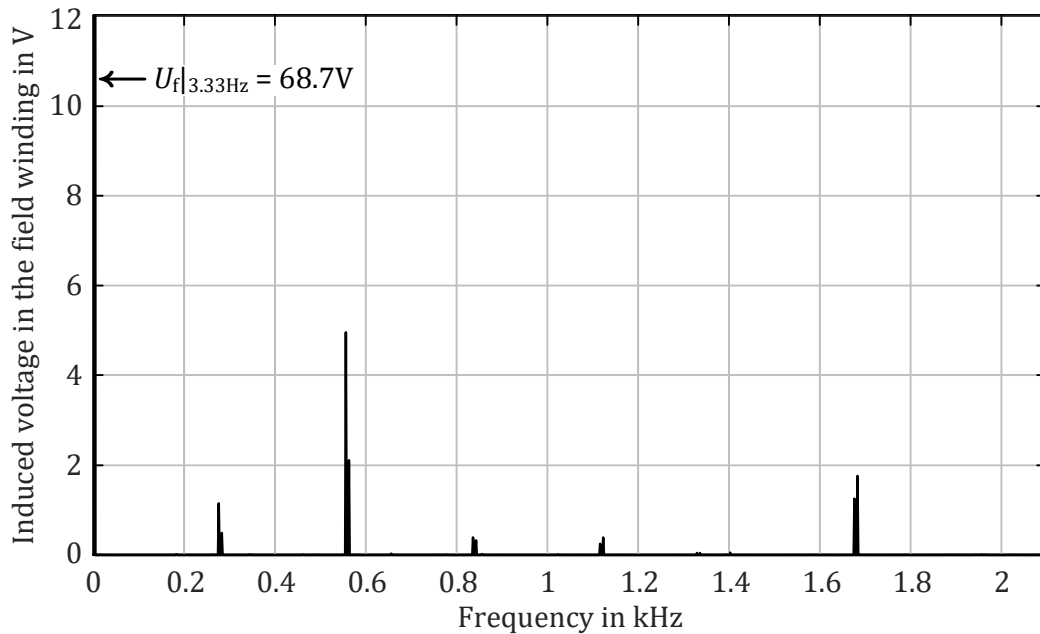


**Figure 7.9:** Simulated harmonic spectrum of the induced voltage in the field winding for operation of the SM at 1400 rpm when the built-in damper cage is enabled and the pole face eddy currents are disabled.

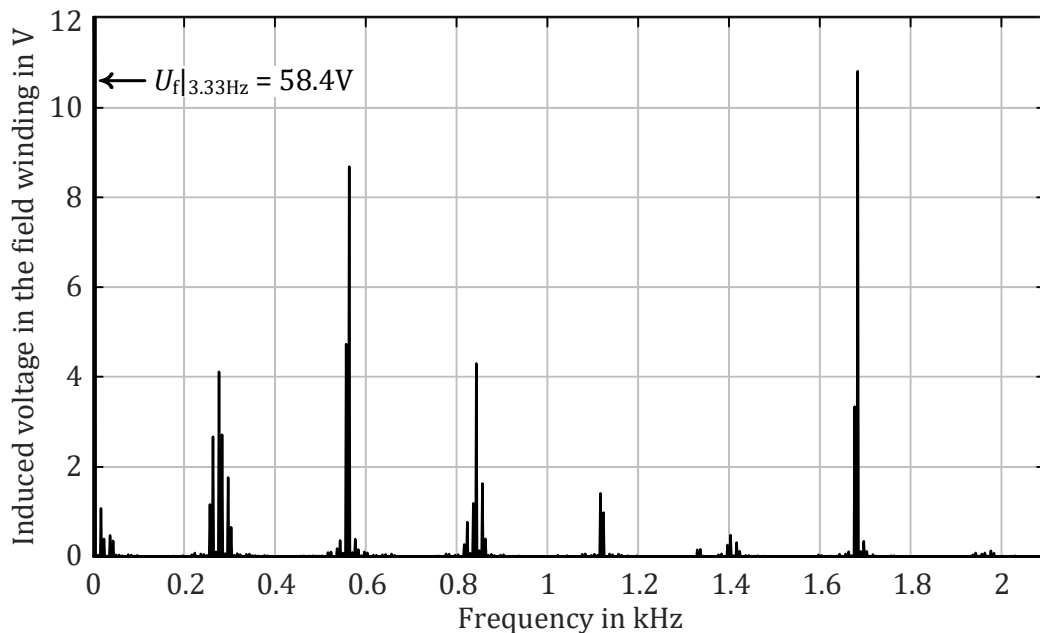


**Figure 7.10:** Simulated harmonic spectrum of the induced voltage in the field winding for operation of the SM at 1400 rpm when the built-in damper cage is disabled and the pole face eddy currents are enabled.

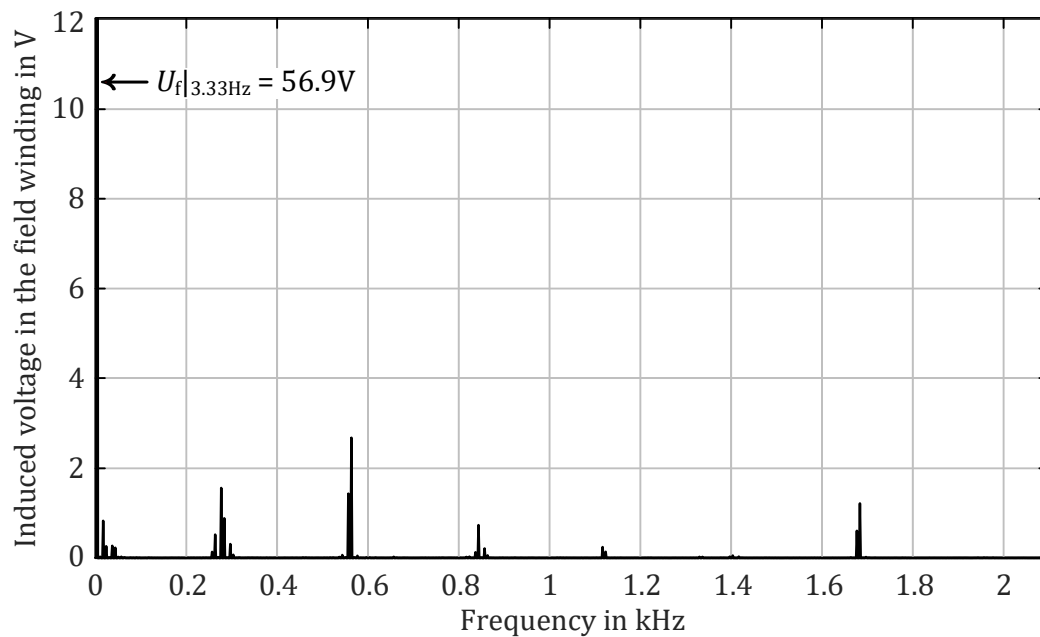


**Figure 7.11:** Simulated harmonic spectrum of the induced voltage in the field winding for operation of the SM at 1400 rpm when both damper circuits are enabled. The corresponding experimental results are shown in Figure 7.12.

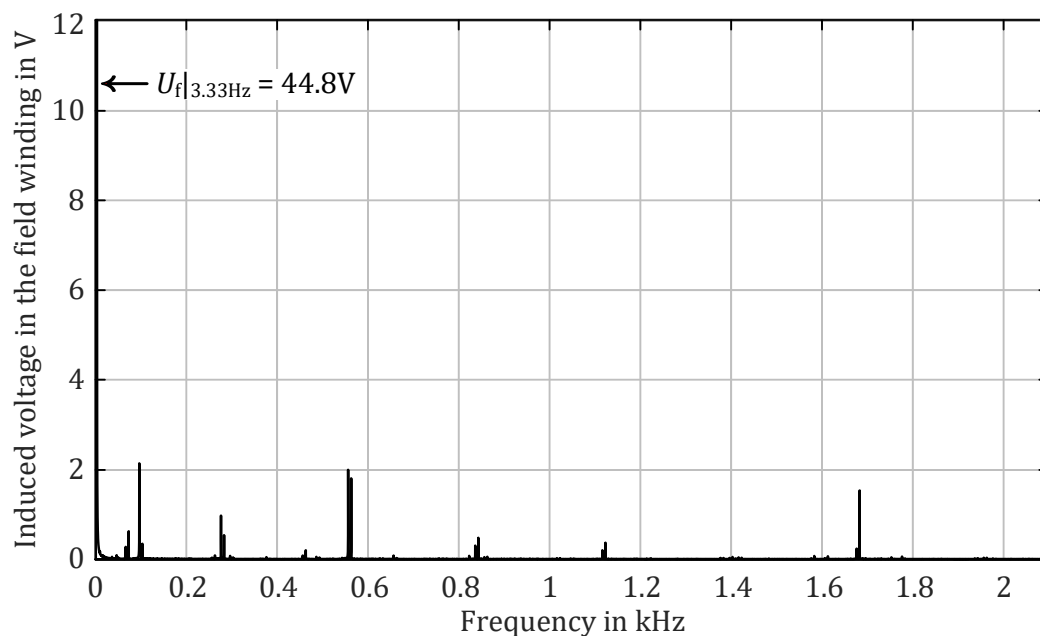


**Figure 7.12:** Measured harmonic spectrum of the induced voltage in the field winding for operation of the SM at 1400 rpm. The corresponding theoretical results are shown in Figure 7.11.

# Chapter 8

## Damper Winding Harmonics Analysis at Full-Size Converter Supply - Results

*This Chapter investigates the harmonic content occurring within the stator and the damper windings for unexcited no-load operation as well as the harmonic content occurring within the stator, damper, and field windings for load operation. The harmonics caused by the synchronous machine's geometry during operation at a purely sinusoidal supply, as per the theory shown in Section 7.2.1, are analyzed utilizing two-dimensional finite element analysis as well as measurements at the custom-built synchronous machine at the test bench. Next, the additional harmonic contents caused by operating the synchronous machine under load with the various full-size converter topologies of Section 7.2.2 are measured and analyzed.<sup>1</sup>*

### 8.1 Harmonic Spectrum Analysis of the SM at Line-Connected No-Load Operation

To analyze the harmonic content of the stator winding, the damper winding, i.e., the built-in damper cage, and the field winding of the synchronous machine (SM) at full-size converter (FSC) supply, it is important to know the harmonic content at line-connected no-load operation with a purely sinusoidal voltage supply. This should represent the baseline for further investigations at load operation with FSC supply presented in Section 8.2. The investigations in this Section are carried out utilizing both two-dimensional finite element analysis (2D-FEA) as well as measurement results obtained at the test bench.

For this test, the SM rotates at constant 1500 rpm which can be set directly in the

---

<sup>1</sup>Selected material of this Chapter has also been published in [87].

2D-FEA and is realized by driving the SM under test with the permanent magnet synchronous machine (PMSM) at the test bench. The SM's stator winding is supplied by a three-phase 50 Hz purely sinusoidal voltage waveform with a nominal voltage of  $U_{ll} = 230$  V. The field winding is not excited.

### 8.1.1 2D Finite Element Analysis

Figure 8.1 depicts the computed harmonic content of the stator winding, the damper winding, and the field winding utilizing 2D-FEA. The present harmonics are caused by the stator mmf harmonics as well as the slot harmonics as described in Section 7.2.1. Here, the harmonic contents of the stator winding, the damper winding, and the field winding are analyzed.

#### Stator Voltage

The SM's stator phase voltage  $U_{ph}$  has a single peak at 50 Hz because of the purely sinusoidal voltage supply. No other significant harmonics are present in the harmonic spectrum of  $U_{ph}$ .

#### Stator Current

The stator current  $I_{ph}$  of the SM has a dominant peak at 50 Hz because of the purely sinusoidal voltage supply.

As per (7.2), the 24 rotor slots  $Q_r$  in combination with the two pole pairs of the SM result in the harmonic orders -11, +13, -23, +25, -35, +37 etc. Multiplying these harmonic orders with the fundamental frequency of 50 Hz results in the harmonic frequencies of 550 Hz, 650 Hz, 1150 Hz, 1250 Hz, 1750 Hz, 1850 Hz, etc. These frequencies are present to various extents in the measured harmonic spectrum of  $I_{ph}$  shown in Figure 8.1. The expected 550 Hz component is the dominant higher-order harmonic and is quite present in the spectrum of the phase current. The 650 Hz component does not exist because of the short-pitching of the stator winding by two slots and the resulting winding factors.

#### Damper Bar Voltage

Multiplying the slips for the higher harmonics  $s_{-5} = 6$ ,  $s_{+7} = -6$ ,  $s_{-11} = 12$ ,  $s_{+13} = -12$ ,  $s_{-17} = 18$ ,  $s_{+19} = -18$  (see Section 7.2.1) with the fundamental frequency of 50 Hz results

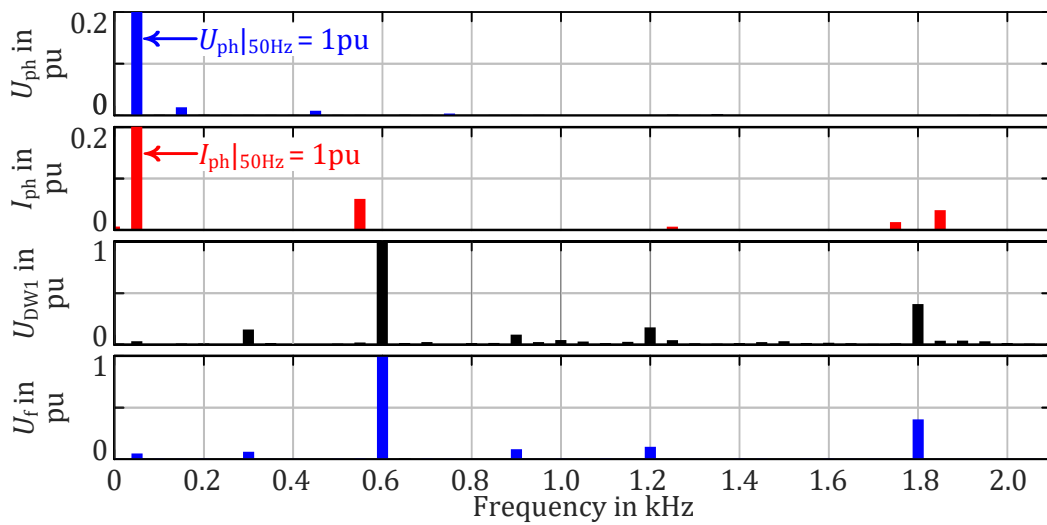


**Figure 8.1:** Computed harmonic spectrum of the stator phase voltage  $U_{ph}$ , the stator current  $I_{ph}$ , the voltage drop at damper bar one  $U_{DW1}$ , and the induced voltage in the field winding  $U_f$  utilizing 2D-FEA; magnitudes are each normalized to their respective maximum values.

in the 300 Hz, 600 Hz, and 900 Hz - components. These frequencies are present to different extents in the measured harmonic spectrum of  $U_{DW1}$  in Figure 8.1.

According to Table 7.1 and (7.2), the stator slot harmonics of the SM under test are -17, +18, -35, +37, etc. These slot harmonics result in the 900 Hz and 1800 Hz - components, etc., which are present to various extents in the measured harmonic spectrum of  $U_{DW1}$  in Figure 8.1 as well.

The 600 Hz - component is the dominant harmonic in this spectrum followed by the 1800 Hz - component. Both harmonics are mainly caused by the dominant harmonics -11 (550 Hz) and +37 (1850 Hz) present in the stator current  $I_{ph}$ .

### Field Voltage

The damper winding's main purpose is to protect the field winding from large induced voltages. However, even at a purely sinusoidal supply, the harmonics penetrate through the damper winding resulting in harmonics in the field winding. These harmonics in the field voltage  $U_f$  are distributed analogously to the harmonic content present in the damper winding (illustrated as the voltage drop at damper bar one  $U_{DW1}$ ). The 600 Hz - component and the 1800 Hz - component are the dominant harmonics in the harmonic spectrum of  $U_f$ .

## 8.1.2 Experimental Analysis

The harmonic content at line-connected no-load operation with a purely sinusoidal voltage supply is analyzed at the test bench analogously to the results presented in Section 8.1.1 utilizing 2D-FEA.

Figure 8.2 depicts the computed harmonic content of the stator winding, the damper winding, and the field winding which are caused by stator mmf harmonics as well as slot harmonics as described in Section 7.2.1. Here, the harmonic contents of the stator winding, the damper winding, and the field winding are analyzed.

### Stator Voltage

The SM's stator phase voltage  $U_{ph}$  has a single peak at 50 Hz because of the purely sinusoidal voltage supply. No other significant harmonics are present in the harmonic spectrum of  $U_{ph}$ .

### Stator Current

The stator current  $I_{ph}$  of the SM under test has a dominant peak at 50 Hz because of the purely sinusoidal voltage supply and the dominant higher-order harmonic occurs at 550 Hz, which is in line with the results presented in Section 8.1.1 obtained from 2D-FEA.

### Damper Bar Voltage

The harmonic orders present in the spectrum of  $U_{DW1}$  are in line with the theoretical analysis presented in Section 7.2.1 and the results displayed in Section 8.1.1 obtained from 2D-FEA. In contrast to the results obtained from 2D-FEA in Figure 8.1, the 900 Hz - component is the dominant harmonic in this measured spectrum. In addition, the magnitudes of the harmonics are distributed more evenly across the harmonic spectrum and, particularly, the 600 Hz - component and the 1800 Hz - component are less pronounced in the measured voltage drop at damper bar one  $U_{DW1}$  compared to the results obtained from 2D-FEA for this operating point. Note that the built-in damper cage utilizes screw connections between the damper bars and the short-circuit rings. Therefore, the contact resistance might not be uniform for all the individual damper bars, which is not implemented in the

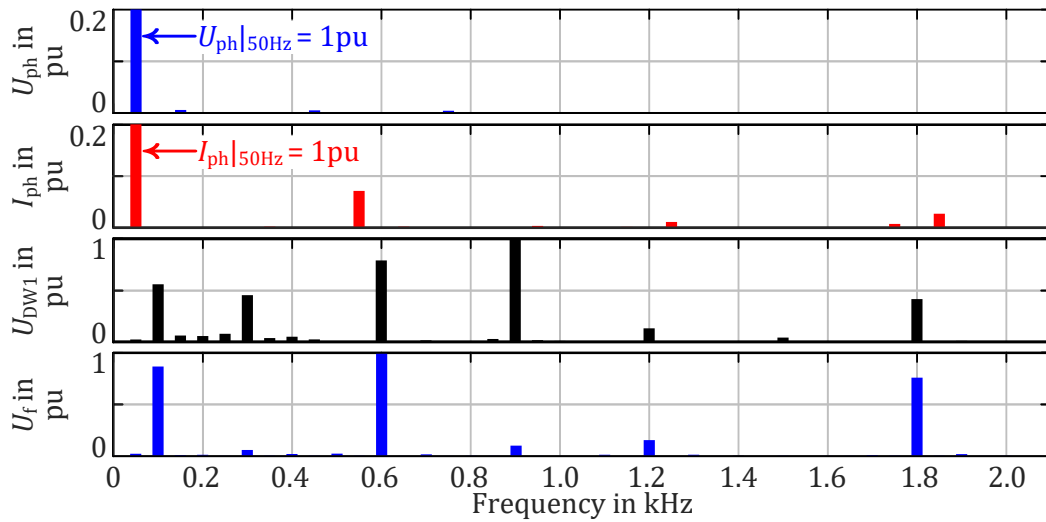


**Figure 8.2:** Measured harmonic spectrum of the stator phase voltage  $U_{ph}$ , the stator current  $I_{ph}$ , the voltage drop at damper bar one  $U_{DW1}$ , and the induced voltage in the field winding  $U_f$ ; magnitudes are each normalized to their respective maximum values.

2D-FEA. This could potentially lead to the mismatch between the results obtained from 2D-FEA and the performed measurements.

A stator current unbalance measured at the machine terminals of the SM under test, which might be caused by an eccentricity of the rotor, causes the additional 100 Hz - component present in the harmonic spectrum of  $U_{DW1}$ .

### Field Voltage

The 600 Hz - component and the 1800 Hz - component are the dominant higher-order harmonics in the harmonic spectrum of  $U_f$ , which is in line with the results for  $U_f$  obtained from 2D-FEA presented in Figure 8.1.

The 100 Hz - component caused by a stator current unbalance is also present in the harmonic spectrum of  $U_f$ .

## 8.2 Motor Operation of the SM at Various Supply Voltages Under Load Condition

Operating the custom-built SM at various supply voltage waveforms under load condition provides insights into the expected additional stress and power loss for the stator winding, the damper winding, and the field winding of a large hydropower motor-generator operating at various FSC topologies. In this Section, the operating point under load condition is analyzed via 2D-FEA for a purely sinusoidal supply and compared to the unexcited no-load operation presented in Section 8.1. The various selected FSC voltage waveforms, namely for the 15-level modular multilevel converter (MMC) and for the 3-level neutral point clamped voltage source converter (NPC VSC), as discussed in Section 7.2.2, will be applied to the custom-built SM under test directly at the test bench via the power amplifier, see Figure 7.1.

For this test, the SM operates as a motor at constant 1500 rpm. A load of 16.6 Nm is applied to the SM which corresponds to 2/3 of the nominal load of the custom-built SM at  $U_{ll} = 230$  V, see Table 7.1. This allow for enough reserve when supplying the machine with the worst-case power converter supply. Applying the load is realized via setting the proper load angle in the 2D-FEA. The load is applied to the SM under test with the PMSM at the test bench. The analysis in this Section is carried out for operation at unity power factor.

### 8.2.1 2D Finite Element Analysis

Figure 8.3 depicts the computed harmonic content of the stator winding, the damper winding, and the field winding utilizing 2D-FEA. The present harmonics are caused by the stator mmf harmonics as well as the slot harmonics as described in Section 7.2.1. Next, the harmonic contents of the stator winding, the damper winding, and the field winding are analyzed.

#### Stator Voltage

The SM's stator phase voltage  $U_{ph}$  has a single peak at 50 Hz because of the purely sinusoidal voltage supply. No other significant harmonics are present in the harmonic spectrum of  $U_{ph}$ .

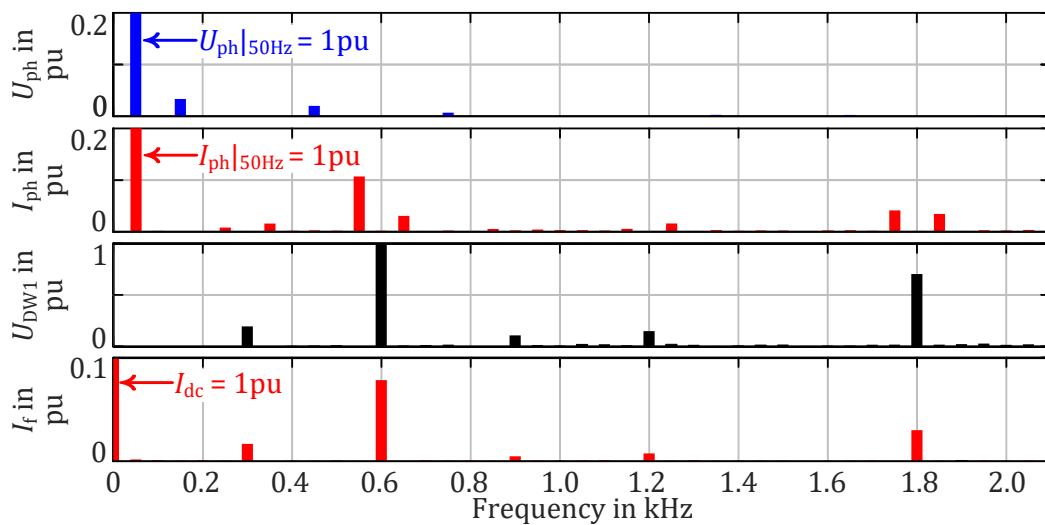


**Figure 8.3:** Computed harmonic spectrum of the stator phase voltage  $U_{ph}$ , the stator current  $I_{ph}$ , the voltage drop at damper bar one  $U_{DW1}$ , and the field current  $I_f$  utilizing 2D-FEA.

### Stator Current

The stator current  $I_{ph}$  of the SM under test has a dominant peak at 50 Hz because of the purely sinusoidal voltage supply. Compared to the harmonic spectrum for unexcited no-load operation presented in Figure 8.1, more of the harmonics described in Section 7.2.1 appear under load condition. However, the dominant higher-order harmonic still occurs at 550 Hz.

### Damper Bar Voltage

The harmonic orders present in the spectrum of  $U_{DW1}$  for load operation are in line with the theoretical analysis presented in Section 7.2.1. However, compared to the unexcited no-load operation illustrated in Figure 8.1, the characteristic harmonics are more distinct for load operation due to the larger magnitudes of the harmonics in the stator current  $I_{ph}$ , and particularly the 1800 Hz - component is significantly larger.

### Field Current

The harmonics penetrate through the damper winding resulting in harmonics in the field winding which are superimposed on the DC current. These harmonics present

in the field current  $I_f$  are distributed analogously to the harmonic content present in the damper winding (illustrated as the voltage drop at damper bar one  $U_{DW1}$ ). The largest magnitude of a higher-order harmonic present in  $I_f$  is 7.8 % of the DC current and can be found at 600 Hz.

## 8.2.2 Experimental Analysis

This Section shows the measurement results for load operation of the custom-built electrically excited SM at the test bench. In line with the earlier analysis, the SM under test is supplied by a purely sinusoidal voltage supply. In addition, it is supplied by a 15-level MMC supply as well as a 3-level NPC VSC supply by the power amplifier, see Section 7.1.

Again, a load of 16.6 Nm is applied to the SM under test, utilizing the PMSM at the test bench, which corresponds to 2/3 of the nominal load of the custom-built SM at  $U_{ll} = 230$  V, see Table 7.1. To obtain comparable results when using the various supply voltage waveforms, the rms value of the phase voltage is kept constant at  $U_{ph} = 130$  V. The SM's excitation current is adjusted to allow for unity power factor operation.

The instantaneous values as well as the harmonic spectra of the stator phase voltage  $U_{ph}$ , the stator current  $I_{ph}$ , the damper bar voltage drop at damper bar one  $U_{DW1}$ , and the field current  $I_f$  are analyzed in the subsequent Sections.

### Sinusoidal Supply

A purely sinusoidal voltage supply is applied to the terminals of the SM under test for the reference measurement. The measured instantaneous values are presented in Figure 8.4.  $U_{ph}$  shows a purely sinusoidal waveform,  $I_{ph}$  reveals a dominant 550 Hz - component, as described in Section 7.2.1, and the harmonics penetrate through the damper circuits, resulting in oscillations of the field current  $I_f$ .

The harmonic spectra for this purely sinusoidal supply are illustrated in Figure 8.5. The harmonic content of  $U_{DW1}$  for the purely sinusoidal voltage supply has been described in Section 8.1.2. The magnitudes of the individual harmonics slightly differ compared to Figure 8.2 since the SM is now excited and operating under load condition, and hence, the current distribution between the individual damper bars differs. The highest peak in the spectrum of  $U_{DW1}$  is at 600 Hz with a magnitude of 9.7 mV. The field current  $I_f$  shows the same harmonics as  $U_{DW1}$ . However, the

100 Hz - component caused by the stator current unbalance of the SM under test is the dominant harmonic in this measured spectrum.

The total power consumption measured at the stator terminals for operation at 2/3 of the nominal load at unity power factor with a purely sinusoidal voltage supply is  $S = 3.24$  kVA. This figure is compared to the values at FSC supply below in Section 8.3.

### 15-Level Modular Multilevel Converter Supply

The instantaneous values for load operation at the 15-level MMC supply, which is the proposed FSC topology for application in large PSPPs, are presented in Figure 8.6.  $U_{ph}$  shows a very sinusoidal waveform, which is perfectly in line with the computed voltage waveform of  $U_{ph}$  in Figure 7.4, and  $I_{ph}$  reveals a dominant 550 Hz - component, as already analyzed for a purely sinusoidal voltage supply.

The harmonic spectra for the 15-level MMC supply are illustrated in Figure 8.7. The harmonic content of  $U_{DW1}$  shows the same harmonics as the harmonic spectrum of the purely sinusoidal voltage supply. However, the magnitudes are slightly higher for the 15-level MMC supply. The 600 Hz - component has a magnitude of 11.8 mV and is therefore increased by a factor of 1.21 compared to the purely sinusoidal voltage supply. The field current  $I_f$  shows the same harmonics as  $U_{DW1}$ . For the 15-level MMC supply, the 600 Hz - component has the largest magnitude in the spectrum of  $I_f$ .

The total power consumption measured at the stator terminals for operation at 2/3 of the nominal load at unity power factor with the 15-level MMC supply is  $S = 3.22$  kVA, which is the same as for the purely sinusoidal voltage supply.

Therefore, utilizing the MMC topology, which comes with the advantage of a high level count, for the FSC, results only in a very small increase of the harmonic content in the damper winding and the field winding. Meanwhile, the power consumption measured at the machine terminals is identical with the power consumption measured for a purely sinusoidal voltage supply.

### Conclusion

Hence, the MMC topology is well suited for operating synchronous motor-generators in large PSPPs, when analyzing the aspects of the harmonic content and the additional power consumption compared to conventional directly line-connected operation.

### 3-Level Neutral-Point Clamped Voltage Source Converter Supply

The stator phase voltage  $U_{ph}$  presented in Figure 8.8 matches the computed voltage waveform  $U_{ph}$  in Figure 7.6 for a 3-level NPC VSC perfectly.

The harmonic spectra for the 3-level NPC VSC supply are illustrated in Figure 8.9. The harmonic spectrum of  $U_{ph}$  shows high order harmonics at 850 Hz, 950 Hz, 1150 Hz, 1250 Hz, 1750 Hz, and 1850 Hz, as discussed theoretically in Section 7.2.2 and presented in Figure 7.7. These harmonics transfer directly to the stator current  $I_{ph}$ . Therefore, the magnitudes of the harmonics present in the voltage drop at damper bar one  $U_{DW1}$  are higher compared to operation at a purely sinusoidal supply. The highest peak can be found at 900 Hz with a magnitude of 20.0 mV which is increased by a factor of 2.65 compared to the purely sinusoidal voltage supply. The harmonics at 1200 Hz and 1800 Hz are intensified compared to a purely sinusoidal voltage supply because of the harmonic content of  $I_{ph}$ . The field current  $I_f$  shows the same harmonics as  $U_{DW1}$ . For the 3-level NPC VSC supply, the 600 Hz - component has the largest magnitude in the spectrum of  $I_f$ .

The total power consumption measured at the stator terminals for operation at 2/3 of the nominal load at unity power factor with the 3-level NPC VSC supply is  $S = 3.46$  kW, which results in an increase of 6.8 % compared to the purely sinusoidal voltage supply. These are attributed to additional power losses due to the power converter supply.

### Conclusion

Therefore, utilizing a power converter topology with a low level count, such as the 3-level NPC VSC supply, results in a severe increase of the magnitudes of the harmonic content present in the damper winding and the field winding. Hence, these components are exposed to additional stress and power loss. In addition, the power consumption measured at the machine terminals increases significantly, which must be taken into consideration when supplying a large hydropower motor-generator with this type of FSC topology.

## 8.2 Motor Operation of the SM at Various Supply Voltages Under Load Condition

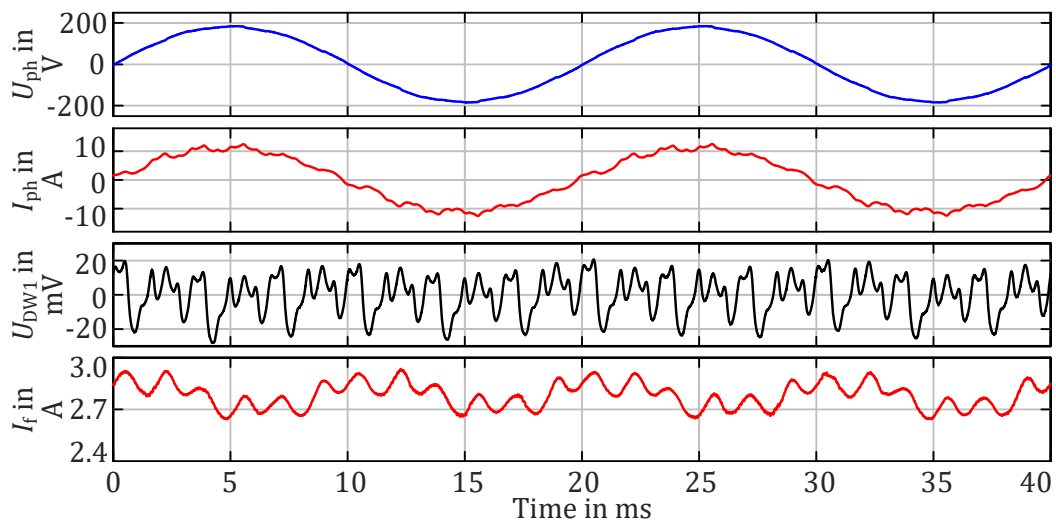


**Figure 8.4:** Measured instantaneous phase voltage  $U_{ph}$ , phase current  $I_{ph}$ , damper bar voltage drop  $U_{DW1}$ , and field current  $I_f$  for operation at 2/3 of the nominal load with a purely sinusoidal voltage supply.

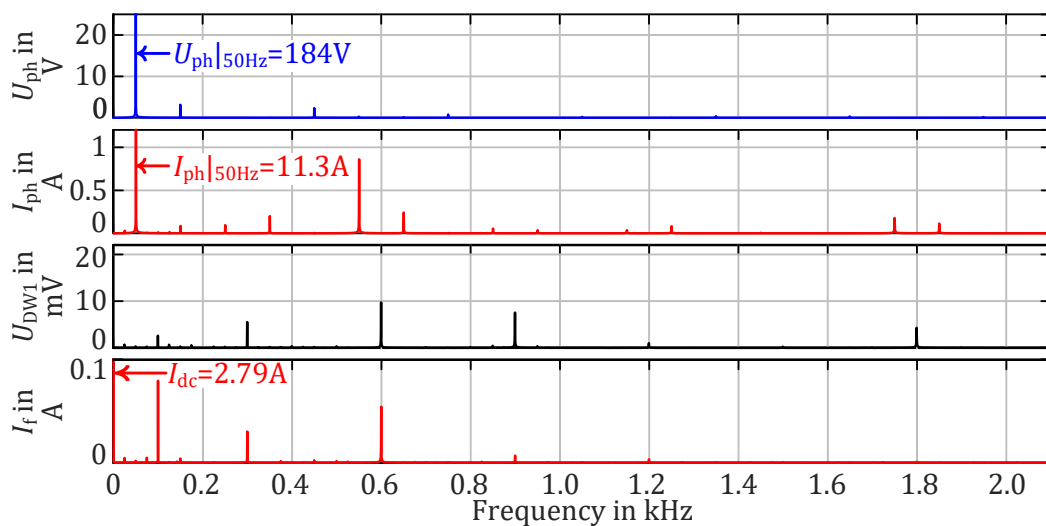


**Figure 8.5:** Measured harmonic spectra of the phase voltage  $U_{ph}$ , phase current  $I_{ph}$ , damper bar voltage drop  $U_{DW1}$ , and field current  $I_f$  for operation at 2/3 of the nominal load with a purely sinusoidal voltage supply.

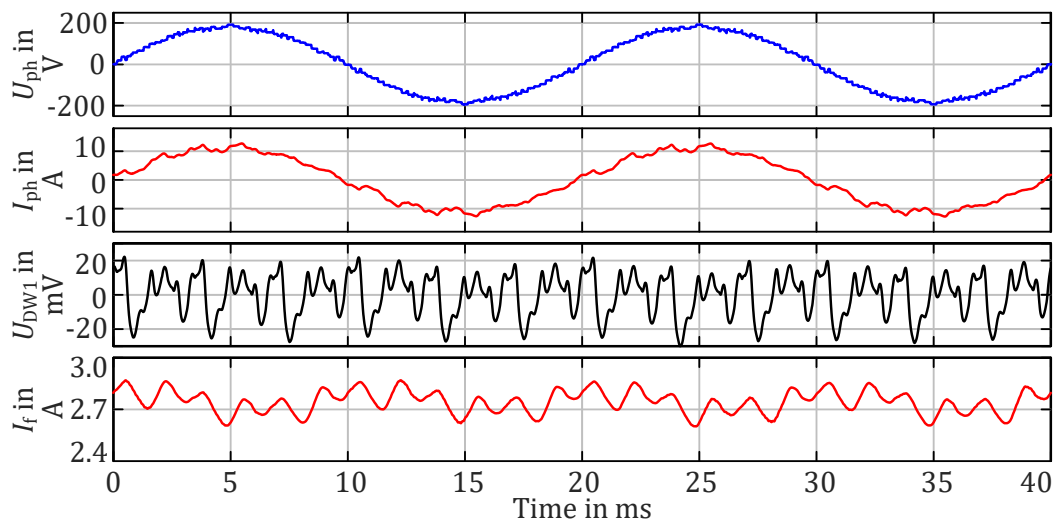


**Figure 8.6:** Measured instantaneous phase voltage  $U_{ph}$ , phase current  $I_{ph}$ , damper bar voltage drop  $U_{DW1}$ , and field current  $I_f$  for operation at 2/3 of the nominal load with a 15-level MMC supply.

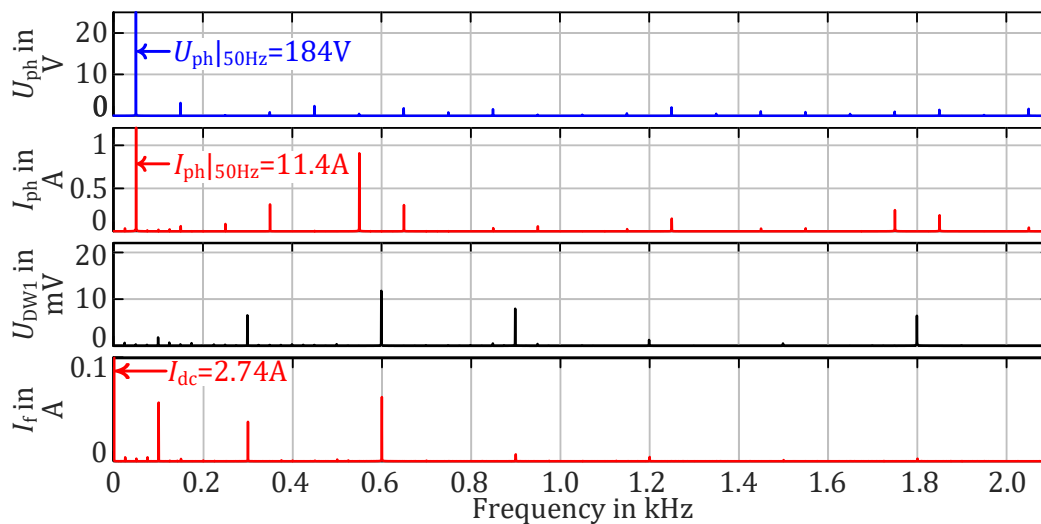


**Figure 8.7:** Measured harmonic spectra of the phase voltage  $U_{ph}$ , phase current  $I_{ph}$ , damper bar voltage drop  $U_{DW1}$ , and field current  $I_f$  for operation at 2/3 of the nominal load with a 15-level MMC supply.

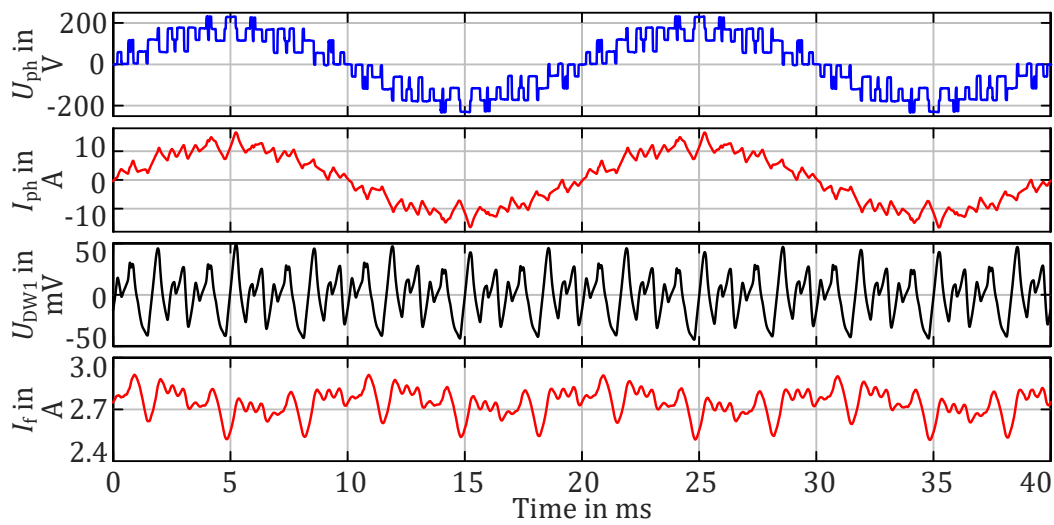


**Figure 8.8:** Measured instantaneous phase voltage  $U_{ph}$ , phase current  $I_{ph}$ , damper bar voltage drop  $U_{DW1}$ , and field current  $I_f$  for operation at 2/3 of the nominal load with a 3-level NPC VSC supply.

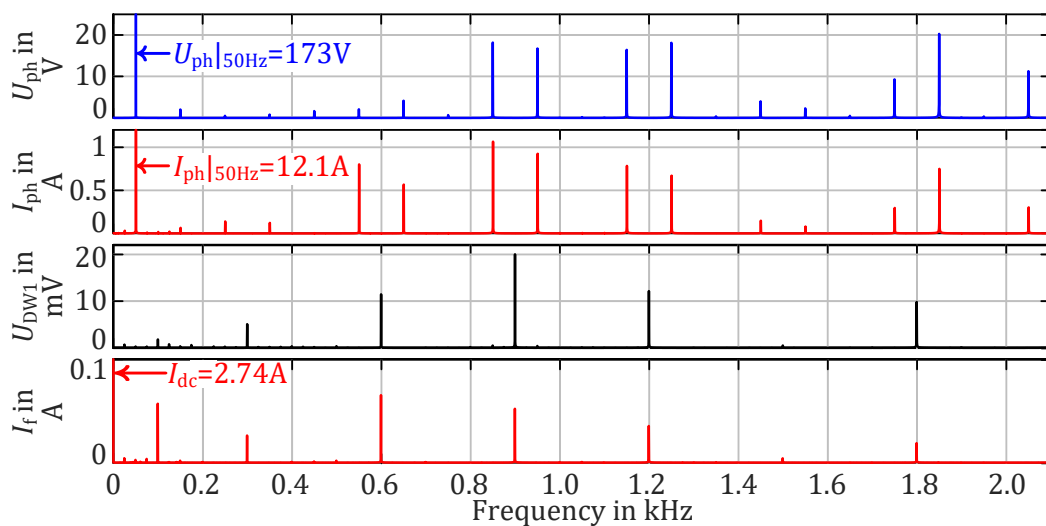


**Figure 8.9:** Measured harmonic spectra of the phase voltage  $U_{ph}$ , phase current  $I_{ph}$ , damper bar voltage drop  $U_{DW1}$ , and field current  $I_f$  for operation at 2/3 of the nominal load with a 3-level NPC VSC supply.

### 8.3 Summary

The MMC topology is the proposed power converter topology for the FSC operation of large PSPPs, as discussed in Section 5.5.1. This is due to its arbitrary scalability to achieve medium-voltage ( $\geq 13.5$  kV) high-power ( $\geq 100$  MW) operation, which is required to supply large hydropower motor-generators. The MMC's main benefit is the very smooth sinusoidal waveform. Hence, the voltage stress for the motor winding insulation and the total harmonic distortion are extremely low.

#### Evaluation of the Power Consumption Measured at the Machine Terminals

The measurements presented in this Section show that supplying the custom-built SM under test with a 15-level MMC supply results in little to no difference for the SM during operation compared to a purely sinusoidal voltage supply. Hence, no additional power consumption was measured at the machine terminals, see Table 8.1.

The measurements presented in this Section utilizing the 3-level NPC VSC topology should represent the worst-case power converter topology for application in large PSPPs resulting in a quite stressful supply voltage waveform for a large synchronous motor-generator. The power consumption measured at the machine terminals is increased by 6.8% when compared to the measurements for a purely sinusoidal voltage supply, see Table 8.1, which is attributed to additional power losses due to the FSC supply.

**Table 8.1:** Power consumption of the SM under test measured at the machine terminals for various supply voltages.

Supply voltage waveform	$S$	$S/S_{\text{sine}}$
Purely sinusoidal supply	3.24 kVA $\pm$ 0.4 % (k=2)	100.0 %
15-level MMC supply	3.22 kVA $\pm$ 0.4 % (k=2)	99.5 %
3-level NPC VSC supply	3.46 kVA $\pm$ 0.4 % (k=2)	106.8 %

Even though this increase in power consumption is already significant for the SM under test, the impact on the power loss of a conventionally manufactured large hydropower motor-generator might be even more pronounced, because of the strand thickness of the stator winding, which is conventionally optimized for 50 Hz or 60 Hz directly line-connected operation. In such case, as stated in [40], which

shows a numerical analysis of the increase of the stator AC copper power loss when utilizing a 3-level NPC VSC supply for a 105 MVA hydropower generator, the stator AC copper power loss increases by a factor of 16 compared to a purely sinusoidal supply. Hence, it is advisable to adjust the strand thickness of the stator winding accordingly, depending on the utilized FSC topology.

### Evaluation of the Harmonics Present in the Damper and Field Winding

Table 8.2 shows the magnitudes of the relevant harmonics of the voltage drop at damper bar one  $U_{DW1}$  and the field current  $I_f$  in comparison to the respective magnitudes measured at the purely sinusoidal voltage supply.

For the 15-level MMC supply, the harmonic content present in the damper winding and the field winding is slightly higher compared to the purely sinusoidal voltage supply. The only harmonic present in the spectrum of  $I_f$  that is significantly larger (times 2.71) compared to the purely sinusoidal voltage supply can be found at 1800 Hz. However, this harmonic is quite low for the purely sinusoidal voltage supply, see Figure 8.5. Hence, no significant additional power loss in the damper winding and the field winding is expected.

**Table 8.2:** Comparison of the harmonics present in the measured harmonic spectra for various supply voltages. The measured magnitudes for the FSC supplies are presented in relation to the measured magnitudes for the purely sinusoidal supply.

$f$ Hz	Sinusoidal supply		15-level MMC		3-level NPC VSC	
	$ U_{DW1} $ mV	$ I_f $ mA	$ U_{DW1} $ pu	$ I_f $ pu	$ U_{DW1} $ pu	$ I_f $ pu
300	5.5	30.2	1.19	1.26	0.92	0.87
600	9.7	54.2	1.21	1.15	1.18	1.20
900	7.6	6.9	1.05	0.97	2.65	7.59
1200	1.0	3.3	1.28	1.24	12.22	10.59
1800	4.3	0.9	1.51	2.71	2.29	20.48

In contrast, the magnitudes of the harmonic spectrum of  $U_{DW1}$  are intensified when operating the SM under test with the 3-level NPC VSC supply. Particularly the 900 Hz - component and the 1800 Hz - component are more than doubled compared to the purely sinusoidal voltage supply. The 1200 Hz - component is only present

in the measured harmonic spectrum for the 3-level NPC VSC supply, which is illustrated in Table 8.2 with the large multiplier for the magnitude of this harmonic of 12.22 compared to the purely sinusoidal voltage supply.

The 900 Hz - component, the 1200 Hz - component, and the 1800 Hz - component become dominant in the spectrum of  $I_f$  basically only for the 3-level NPC VSC supply. This is illustrated in Table 8.2 with the large multipliers of 7.59, 10.59, and 20.48 for the magnitudes of the respective harmonics. The 300 Hz - component and the 600 Hz - component do not increase significantly since the FSC supply does not cause any additional harmonics in this frequency range, see Figure 8.8.

The drastic increase of the magnitudes of the harmonics present in the spectrum of  $U_{DW1}$  and  $I_f$  results in a significant increase of the power loss in the damper winding and the field winding. The analysis presented in [40] also depicts that the power loss in the damper winding increases by a factor of 3.9 when operating the machine with a 3-level NPC VSC supply instead of a purely sinusoidal supply. This is due to the additional harmonic content caused by the FSC, which is in line with the experimental results reported on here.

As a result, choosing a suitable FSC topology is a key aspect for obtaining a high system performance of the FSC operated synchronous motor-generators in large PSPPs. Then, the benefits for utilizing the MMC topology, which are presented in detail in Section 5.5.1, can lead to a superior performance of the synchronous motor-generator at FSC operation with little to no additional stress for the motor windings and no measurable additional power consumption at the machine terminals, like in the case of the measurement results obtained for the custom-built SM at the test bench, and hence, possibly no additional power loss in the damper winding.

# Conclusion

The full-size converter operated electrically excited salient-pole synchronous motor-generator for application in large pumped storage power plants represents a highly flexible energy storage technology to enable further integration of renewable energy sources like wind and solar. This is due to the achievable active power range both in turbine and pumping modes enabled by the variable-speed capability.

This thesis proposes an improved design for electrically excited salient-pole synchronous motor-generators for application in large pumped storage power plants utilizing full-size converter operation. A 150 MVA, 50 Hz, 200 rpm,  $\cos \varphi = 0.9$  conventional directly line-connected synchronous motor-generator is defined as the starting point for this comprehensive analysis. The particularities for the design criteria derived from the decoupling of the synchronous machine from the grid due to the full-size converter operation are identified within this thesis as well. Particularly, the free choice of the power factor for the machine design results in significant savings, since the reactive power can be provided to the grid by the full-size converter independently. The cost evaluation of large hydropower generators considers both the costs for materials as well as the costs for power loss during operation. Therefore, the possible design frequency range to optimize the generator design is quite limited because of the large amount of construction material of low-frequency designs and the poor efficiency of high-frequency designs. Hence, Section 4.2 shows that the optimum design frequency is around 60 Hz. The main parameters that affect the optimum design frequency are the cost evaluation factors, which depend largely on the specific project and the customer's requirements. The utilization coefficient only has a marginal influence on the optimum design frequency while the rotational speed, which depends on the specific project due to the pump-turbine design, has no impact on the choice of the optimum design frequency. Since the full-size converter operated synchronous machine in large pumped storage power plants is utilized to adapt quickly to the current grid requirements, it operates at partial load for a signif-

icant amount of time. However, knowing the partial load profile already during the generator design stage does not lead to significant changes for a further optimization of the design as has been investigated in this thesis also.

All things considered, Section 4.7 shows that it is possible to achieve a cost reduction for the synchronous motor-generator specifically for full-size converter operation of 18% compared to a conventional directly line-connected synchronous machine.

The choice of the power converter topology is key to achieve high performance with the full-size converter operated synchronous motor-generator. The main requirements for the full-size converter for application in large pumped storage power plants are medium-voltage ( $\geq 13.5$  kV) high-power ( $\geq 100$  MW) regenerative power capability (bidirectional power flow). In addition, smooth sinusoidal voltage waveforms should be supplied to the machine so as to not cause additional stress on the winding insulation and to not cause additional power loss. These requirements are difficult to achieve with today's power converter topologies used for industrial applications. Because of its arbitrary scalability and excellent performance, the modular multilevel converter topology is investigated intensively throughout this thesis for application in large pumped storage power plants. With the implemented analysis tools for the modular multilevel converter, the supply voltage waveforms can be generated, the switching frequency of the individual power semiconductor devices can be derived, and the efficiency can be computed utilizing an analytic average loss model including the on-state power loss and the switching power loss of the semiconductor power devices. The overall efficiency of the system comprising the full-size converter and the synchronous motor-generator is analyzed in Section 6.2.3 for a pumped storage application operating at nominal load and partial load for both turbine and pumping modes. The results show that the overall efficiency increases for operating points at partial load. In contrast, the efficiency of the directly line-connected synchronous motor-generator decreases for operating points at partial load.

Measurements carried out at the test bench for a custom-built synchronous machine, which allows for the measurement of the induced voltage in the damper winding as the voltage drops at the individual damper bars, show that no additional power consumption is measured at the machine terminals for a 15-level modular

---

multilevel converter supply compared to a purely sinusoidal supply, which could be attributed to additional power loss, see Section 8.3. The additional harmonic content measured in the damper winding and the field winding is very low for the 15-level modular multilevel converter and hence, possibly negligible.

Operating the synchronous machine at the test bench with the 3-level neutral point clamped voltage source converter, which is the state-of-the-art in today's large drive applications, results in quite stressful operation. Compared to operation at purely sinusoidal supply, this power converter supply increases the power consumption at the machine terminals by 6.8 % for the custom-built synchronous machine under test. Also, the harmonic content measured in the damper winding and the field winding increases significantly for operation at the 3-level neutral point clamped voltage source converter compared to operation at a purely sinusoidal supply or the 15-level modular multilevel converter supply, and hence, leads to additional stress in the rotor which needs to be considered.

## Future Work

The potential cost savings due to the additional degrees of freedom for the synchronous motor-generator design at full-size converter operation have been analyzed for a 135 MW, 13.5 kV, 200 rpm machine in Chapter 4. Further analysis should evaluate the potential cost savings for higher power machines as well.

The utilized simplified power loss model presented in Section 3.2.1 is used to identify the relationship between the sources of power loss in the machine. It is assumed that the additional power loss due to a non-sinusoidal power supply can be neglected when utilizing a multilevel power converter topology with a high number of levels. Implementing a power loss model that considers the harmonic spectrum of the machine supply would allow analyzing the impact of power converter topologies with a lower number of levels on the motor-generator design. To this aim, also the damper winding power loss and the pole-shoe surface power loss should be included for further analysis.

The overall efficiency of the system comprising the synchronous motor-generator and the full-size converter is analyzed in Section 6.2.2 for operation at a load profile for both turbine and pumping modes. It would be a great addition to also include the efficiency of an appropriate combined reversible-speed pump-turbine to investigate the total efficiency of the entire system. For this analysis, efficiency curves for the pump-turbine depending on the mode of operation, the water flow rate, the

hydraulic head, and the rotational speed would be required.

The control of the full-size converter operated synchronous motor-generator is another interesting research field of further research. Particularly the opportunity to provide synthetic inertia to the grid via the full-size converter while still having real inertia in the form of the rotating synchronous motor-generator should open up many options regarding the enhanced support of the grid. A simulation model comprising the pump-turbine, the synchronous motor-generator, the full-size converter, the grid, as well as the control should allow for investigating the opportunities for operation of the pumped storage power plant. In this context, the additional common-mode voltage at the machine terminals caused by the full-size converter, possible resulting parasitic effects, as well as mitigation strategies should be analyzed.

For the modeling of the custom-built electrically excited synchronous machine at the test bench, additional non-ideal properties of the machine could be implemented, i.e., a potential eccentricity and a stator current unbalance. A parameter study regarding the damper cage, which utilizes screw connections between the damper bars and the short-circuit rings, should be carried out as well. Particularly varying the contact resistance in the model, which might not be uniform for all the individual damper bars in reality due to the screw connections, might help to obtain a better agreement between the measured harmonics in the damper winding and the results obtained from the finite element analysis. Setting up a three-dimensional model for carrying out the finite element analysis to also consider additional effects in the end-winding region could be valuable as well.

# Symbols and Abbreviations

## Symbols

SYMBOL	UNIT	NAME
$A$	A/m	linear current density
$A_{\text{cu}}$	m <sup>2</sup>	copper cross section
$A_{\text{max}}$	A/m	maximum allowed linear current density of the stator
$A_{\text{s}}$	m <sup>2</sup>	stator slot cross section
$A_{\text{y,r}}$	m <sup>2</sup>	rotor yoke cross section
$a$	-	number of parallel paths
$a_{\text{sc}}$	-	number of subconductors
$a_{\text{x}}$	-	number of strands arranged side by side
$a_{\text{y}}$	-	number of strands stacked on top of each other
$B_{\text{t,max}}$	T	maximum allowed flux density at the smallest cross section of the stator teeth
$B_{\text{h}}$	T	main flux density
$B_{\text{t}}$	T	stator tooth flux density
$B_{\text{y,s}}$	T	stator yoke flux density
$B_{\delta}$	T	air-gap flux density
$B_{\delta 1}$	T	fundamental air-gap flux density
$C$	VAs/m <sup>3</sup>	Esson utilization coefficient
$C$	F	capacitor
$C_{\text{const}}$	EUR/W	costs for constant power losses
$C_{\text{cu}}$	EUR/kg	material cost for copper
$C_{\text{fe,r}}$	EUR/kg	material cost for rotor iron
$C_{\text{fe,s}}$	EUR/kg	material cost for stator iron
$C_{\text{load}}$	EUR/W	costs for load dependent power losses
$C_{\text{total}}$	EUR	total cost
$\cos \varphi$	-	power factor

$D$	-	power diode
$d$	m	stator inside diameter (air-gap diameter)
$d_o$	m	stator outside diameter
$f$	Hz	electrical frequency
$f_c$	Hz	carrier frequency
$f_s$	Hz	switching frequency
$f_{s,max}$	Hz	maximum switching frequency
$g$	-	counting variable
$H$	m	hydraulic head
$H_n$	m	nominal hydraulic head
$h_{cu}$	m	height of the conductor
$h_{pb}$	m	pole body height
$h_{pt}$	m	pole tip height
$h_s$	m	stator slot height
$h_{y,r}$	m	rotor yoke height
$h_{y,s}$	m	stator yoke height
$I$	A	current
$I_C$	A	maximum continuous DC collector current
$I_f$	A	field current
$I_{on}^*$	A	equivalent on-state current
$I_{ph}$	A	phase current
$I_W$	A	MMC phase current
$i_{arm}$	A	MMC arm current
$i_D, i_Q$	A	currents through the power semiconductor devices
$J$	$kg \cdot m^2$	mass moment of inertia
$J_{cu}$	$A/m^2$	current density
$k_{fe}$	-	iron fill factor
$k_J$	$kg/m^3$	inertia coefficient
$k_w$	-	winding factor
$k_{w1}$	-	fundamental winding factor
$L_{arm}$	H	arm inductor
$l$	m	total axial length
$l_{ew}$	m	length of the end-winding

$l_f$	m	average coil length of the field winding
$l_w$	m	total length of a winding turn
$m$	-	number of phases
$m$	kg	total machine mass
$m$	-	modulation index
$m_{cu,r}$	kg	rotor copper mass
$m_{cu,s}$	kg	stator copper mass
$m_{fe,r}$	kg	rotor iron mass
$m_{fe,s}$	kg	stator iron mass
$m_r$	kg	rotor mass
$m_s$	kg	stator mass
$n$	rpm	mechanical speed (rotational speed)
$n$	-	number of submodules
$n_{IGBT}$	-	number of IGBTs in parallel
$P$	W	active power
$P_{cu}$	W	resistive power loss
$P_{cu,f}$	W	resistive power loss of the field winding
$P_{cu,s}$	W	resistive power loss of the stator winding
$P_{cu,s,skin}$	W	power loss due to the skin effect
$P_{cu,s,add}$	W	additional power loss of the Roebel bars
$P_{d,DC-AC}$	W	power loss of a single DC-AC conversion stage
$P_{fe}$	W	stator iron power loss
$P_{fe,t}$	W	power loss in the stator teeth
$P_{fe,y}$	W	power loss in the stator yoke
$P_{load}$	W	load dependent power loss
$P_{mech}$	W	mechanical power loss
$P_{on}$	W	on-state power loss
$P_{ref}$	W	reference power for the data-sheet values
$P_s$	W	switching power loss
$P_{total}$	W	total power loss
$p$	-	number of pole-pairs
$Q$	var	reactive power
$Q$	-	number of slots

$Q$	-	semiconductor power switch
$Q$	$\text{m}^3/\text{s}$	water flow rate
$Q_n$	$\text{m}^3/\text{s}$	nominal water flow rate
$Q_r$	-	number of rotor slots
$Q_s$	-	number of stator slots
$q$	-	number of slots per pole and phase
$R_{\text{cu},f}$	$\Omega$	resistance of the field winding
$R_{\text{ph}}$	$\Omega$	resistance of a single stator phase
$S$	VA	apparent power
$s$	-	slip
$T$	Nm	torque
$T_a$	s	acceleration time constant
$T_n$	Nm	nominal torque
$t$	s	time
$U$	V	voltage
$U_{\text{CE}}$	V	collector-emitter voltage
$U_{\text{CES}}$	V	maximum collector-emitter voltage
$U_{\text{C,SM}}$	V	submodule capacitor voltage
$U_{\text{DC}}$	V	DC-link voltage
$U_{\text{DW1}}$	V	voltage drop at damper bar one
$U_{\text{F}}$	V	diode forward voltage
$U_{\text{f}}$	V	induced voltage in the field winding
$U_{\text{ll}}$	V	line-to-line voltage
$U_{\text{h}}$	V	internal voltage
$U_{\text{p}}$	V	back-electromotive force
$U_{\text{ph}}$	V	phase voltage
$U_{\text{ph,FSC}}$	V	phase voltage of the FSC
$U_{\text{ph,MMC}}$	V	phase voltage of the MMC
$U_{\text{SM}}$	V	submodule voltage
$U_{\text{v}}$	V	magnitude of the individual voltage harmonic
$U_{\sigma}$	V	voltage drop at the leakage reactance
$V$	$\text{m}^3$	total construction volume
$V_i$	$\text{m}^3$	inner machine volume

$v_{\max}$	m/s	maximum allowed circumferential speed of the rotor
$W_{\text{on}}$	J	turn-on energy
$W_{\text{off}}$	J	turn-off energy
$W_{\text{rec}}$	J	reverse recovery energy
$w_{\text{cu}}$	m	width of the conductor
$w_{\text{cu,f}}$	m	width of the conductor of the field winding
$w_{\text{f}}$	-	number of field winding turns per pole
$w_{\text{pb}}$	m	pole body width
$w_{\text{ph}}$	-	number of phase winding turns
$w_{\text{pt}}$	m	pole tip width
$w_{\text{s}}$	m	stator slot width
$w_{\text{t}}$	m	stator tooth width
$X_{\sigma}$	$\Omega$	leakage reactance
$x_{\text{d}}$	pu	synchronous reactance
$x_{\text{h}}$	pu	magnetizing reactance
$x_{\sigma}$	pu	leakage reactance
$y$	-	coil pitch
$z_{\text{s}}$	-	number of conductors per slot
$\beta$	-	pole field factor
$\Delta U_{\text{C,SM}}$	V	submodule capacitor voltage ripple
$\Delta \eta$	%-points	difference of energy conversion efficiencies
$\delta$	m	geometrical air-gap length
$\delta'$	m	equivalent air-gap length
$\eta$	%	energy conversion efficiency
$\eta_{\text{DC-AC}}$	%	energy conversion efficiency of a single DC-AC stage
$\eta_{\text{MMC}}$	%	energy conversion efficiency of the MMC
$\Theta_{\text{f}}$	At	rotor winding (field winding) magnetomotive force
$\Theta_{\text{m}}$	At	overall magnetomotive force
$\Theta_{\text{s}}$	At	stator winding magnetomotive force
$\kappa_{\text{cu}}$	1/ $\Omega\text{m}$	electrical conductivity of copper
$\mu_0$	Vs/Am	magnetic permeability of the vacuum
$\nu$	-	harmonic order
$\rho_{\text{fe}}$	kg/m <sup>3</sup>	density of the electric steel

$\sigma_{\max}$	N/m <sup>2</sup>	maximum allowed mechanical stress on the utilized materials of the rotor construction
$\tau_p$	m	pole-pitch
$\tau_{p,\max}$	m	maximum allowed pole-pitch to ensure mechanical feasibility of the rotor poles
$\tau_s$	m	slot-pitch
$\phi_h$	Vs	main flux
$\phi_t$	Vs	stator tooth flux
$\phi_{y,s}$	Vs	stator yoke flux
$\phi_\delta$	Vs	air-gap flux
$\phi_{\delta 1}$	Vs	fundamental air-gap flux
$\varphi$	°	phase angle
$\varphi_s$	-	slot fill factor
$\omega$	rad/s	electrical angular frequency
$\omega_{\text{mech}}$	rad/s	mechanical angular frequency

## Abbreviations

ABBREVIATION	NAME
2D	two-dimensional
AC	alternating current
AFE	active front-end
CHB	cascaded H-bridge
DC	direct current
DFE	diode front-end
DFIM	doubly-fed induction machine
EMF	electromotive force
FC	flying capacitor
FEA	finite element analysis
FSC	full-size converter
HNPC	H-bridge neutral point clamped
HP	high-power
HPP	hydropower plant
HVDC	high-voltage DC transmission

---

I	inverter mode
IGBT	insulated gate bipolar transistors
IGCT	integrated gate commutated thyristor
LVRT	low-voltage ride through
MC	matrix converter
MMC	modular multilevel converter
MMF	magnetomotive force
MMMC	modular multilevel matrix converter
MV	medium-voltage
NPC	neutral point clamped
P	pump
P	pumping mode
PC	power converter
PCC	point of common coupling
PMSM	permanent magnet synchronous machine
PSPP	pumped storage power plant
PT	pump-turbine
PWM	pulse width modulation
R	rectifier mode
RPC	rotor power converter
SM	sub-module
SM	synchronous machine
SG	synchronous motor-generator
T	turbine
T	turbine mode
THD	total harmonic distortion
VSC	voltage source converter



# Bibliography

- [1] T. Holzer and A. Muetze, "Full-size converter operation of hydro power generators: A state-of-the-art review of motivations, solutions, and design implications," *e & i Elektrotechnik und Informationstechnik*, vol. 136, no. 2, pp. 209–215, Jan 2019.
- [2] Andritz Hydro, "Neue Chancen fuer Pumpspeicherkraftwerke," *Hydro news*, 2014.
- [3] E. Schmidt, J. Ertl, A. Preiss, R. Zensch, R. Schuerhuber, and J. Hell, "Studies about the low voltage ride through capabilities of variable-speed motor-generators of pumped storage hydro power plants," in *21st Australasian Universities Power Engineering Conference (AUPEC)*, Brisbane, QLD, Australia, 2011, pp. 1–6.
- [4] M. Valavi and A. Nysveen, "Variable-speed operation of hydropower plants: A look at the past, present, and future," *IEEE Industry Applications Magazine*, vol. 24, no. 5, pp. 18–27, Sep-Oct 2018.
- [5] H. Schlunegger, "Pumping efficiency: A 100 MW converter for the Grimsel 2 pumped storage plant," *ABB review*, pp. 42–47, 2014.
- [6] J. Perez-Diaz, M. Chazarra, J. Garcia-Gonzalez, G. Cavazzini, and A. Stopato, "Trends and challenges in the operation of pumped-storage hydropower plants," *Renewable and Sustainable Energy Reviews*, vol. 44, Apr 2015.
- [7] L. Ruppert, R. Schuerhuber, B. List, A. Lechner, and C. Bauer, "An analysis of different pumped storage schemes from a technological and economic perspective," *Energy*, vol. 141, pp. 368 – 379, Sep 2017.
- [8] M. Basic, P. Silva, and D. Dujic, "High power electronics innovation perspectives for pumped storage power plants," in *Hydro*, 2018.

- [9] M. Ezzat, M. Benbouzid, S. M. Muyeen, and L. Harnefors, "Low-voltage ride-through techniques for DFIG-based wind turbines: state-of-the-art review and future trends," in *39th Annual Conference of the IEEE Industrial Electronics Society (IECON)*, Vienna, Austria, 2013, pp. 7681–7686.
- [10] J. Hell, M. Egretzberger, A. Lechner, R. Schuerhuber, and Y. Vaillant, "Full size converter solutions for pumped storage plants - a promising new technology," in *Hydro*, Bilbao, Spain, 2012.
- [11] E. L. Engevik, T. E. Hestengen, M. Valavi, and A. Nysveen, "Effects of lifting reactance requirements on the optimal design of converter-fed synchronous hydrogenerators," in *IEEE International Electric Machines and Drives Conference (IEMDC)*, Miami, FL, USA, 2017, pp. 1–8.
- [12] G. Traxler-Samek, "Analytical and numerical design methods for the electromechanical calculation of hydro-generators," habilitation, TU Darmstadt, Darmstadt, DE, 2014.
- [13] T. Holzer and A. Muetze, "A comparative survey of power converter topologies for full-size converter operation of medium-voltage hydropower generators," *e & i Elektrotechnik und Informationstechnik*, vol. 136, no. 6, pp. 263–270, Oct 2019.
- [14] P. K. Steimer, O. Senturk, S. Aubert, and S. Linder, "Converter-fed synchronous machine for pumped hydro storage plants," in *IEEE Energy Conversion Congress and Exposition (ECCE)*, Pittsburgh, PA, USA, 2014, pp. 4561–4567.
- [15] E. Schmidt, C. Grabner, and G. Traxler-Samek, "Reactance calculation of a 500 MVA hydro-generator using a finite element analysis with superelements," in *IEEE International Electric Machines and Drives Conference (IEMDC)*, Cambridge, MA, USA, 2001, pp. 838–844.
- [16] S. Allebrod, R. Hamerski, and R. Marquardt, "New transformerless, scalable modular multilevel converters for hvdc-transmission," in *IEEE Power Electronics Specialists Conference*, Rhodes, Greece, 2008, pp. 174–179.
- [17] D. Oeding and B. R. Oswald, *Elektrische Kraftwerke und Netze*. Springer Berlin Heidelberg, 2016.
- [18] J. Giesecke and E. Mosonyi, *Wasserkraftanlagen: Planung, Bau und Betrieb*. Springer Berlin Heidelberg, 2014.

- [19] J. H. Walker, *Large Synchronous Machines*. Clarendon Press Oxford, 1981.
- [20] GE, "Connecting water to wire," product presentation, 2016.
- [21] H. Schlunegger and A. Thoeni, "100-MW-Vollumrichter im Pumpspeicherwerk Grimsel 2," *Technologie Speicherung*, 2014.
- [22] H. Foerster and R. Wagnitz, "An inverter for the pump-storage power station at Forbach of the German utility Badenwerke, today EnBW," *AEG Industrial Engineering GmbH*, n.d.
- [23] A. Santolin, G. Pavesi, G. Cavazzini, and G. Ardizzon, "Variable-speed Pelton turbine for an efficient exploitation of the reserved flow: An Italian case study," in *Hydro*, 2013.
- [24] T. Hildinger and L. Koedding, "Modern design for variable speed motor-generators - asynchronous (DFIM) and synchronous (SMFI) electric machinery - options for pumped storage power plants," in *Hydro*, 2013.
- [25] C. Nicolet, O. Braun, N. Ruchonnet, A. Beguin, J. Hell, and F. Avellan, "Full size frequency converter for fast Francis pump-turbine operating mode transition," in *HydroVision*, Minneapolis, MN, USA, 2016.
- [26] J. Koutnik, M. Bruns, L. Meier, and C. Nicolet, "Pumped storage - grid requirements behaviour of large motor-generators and confirmation of compliance through simulation," in *HydroVision*, 2011.
- [27] A. Bocquel and J. Janning, "Analysis of a 300 MW variable speed drive for pump-storage plant applications," in *EPE Conference*, Dresden, DE, 2005, pp. 1–10.
- [28] J. Kahlert and U. Geiger, "Pumped storage plant Goldisthal - from planning to today's operation," presentation, VGB Conference Power Plants, Bern, CH, Sep 2011.
- [29] J. Koutnik, T. Hildinger, and M. Bruns, "A step forward - variable speed pumped storage power plant Frades II," *Wasserwirtschaft*, pp. 27–32, Jan 2015.
- [30] J. Krenn, H. Keck, and M. Sallaberger, "Small and mid-size pump-turbines with variable speed," *Energy and Power Engineering*, vol. 05, pp. 48–54, Jan 2013.

- [31] A. Vargas-Serrano, A. Hamann, S. Hedtke, C. M. Franck, and G. Hug, "Economic benefit analysis of retrofitting a fixed-speed pumped storage hydropower plant with an adjustable-speed machine," in *IEEE Manchester PowerTech*, Manchester, UK, 2017, pp. 1–6.
- [32] L. Ruppert, "Pumped-storage implementation in order to balance volatile renewable energy generation," dissertation, TU Wien, Vienna, AT, 2017.
- [33] T. Holzer and A. Muetze, "Full-size converter operation of large hydro power generators: Generator design aspects," in *2018 IEEE Energy Conversion Congress and Exposition (ECCE)*, Portland, OR, USA, 2018, pp. 7363–7368.
- [34] T. Holzer, A. Muetze, G. Traxler-Samek, M. Lecker, and F. Zerobin, "Generator design possibilities for full-size converter operation of large pumped storage power plants," *IEEE Transactions on Industry Applications*, vol. 56, no. 4, pp. 3644–3655, Jul-Aug 2020.
- [35] G. Mueller, K. Vogt, and B. Ponick, *Berechnung elektrischer Maschinen*. Wiley-VCH, 2008.
- [36] J. Bacher, "Berechnung elektrischer Maschinen," Vorlesungsskriptum, TU Graz, Graz, Austria.
- [37] K. Bonfert, *Betriebsverhalten der Synchronmaschine: Bedeutung der Kenngrößen fuer Planung und Betrieb elektrischer Anlagen und Antriebe*. Springer Berlin Heidelberg, 2013.
- [38] E. L. Engevik, M. Valavi, and A. Nysveen, "Efficiency and loss calculations in design of converter-fed synchronous hydrogenerators," in *XXII International Conference on Electrical Machines (ICEM)*, Lausanne, Switzerland, 2016, pp. 1636–1642.
- [39] A. Binder, *Elektrische Maschinen und Antriebe: Grundlagen, Betriebsverhalten*. Springer Berlin Heidelberg, 2018.
- [40] E. L. Engevik, M. Valavi, and A. Nysveen, "Analysis of additional eddy-current copper losses in large converter-fed hydropower generators," in *2018 XIII International Conference on Electrical Machines (ICEM)*, Alexandroupoli, Greece, Sep 2018, pp. 1067–1073.

- [41] S. Keller, M. T. Xuan, J. Simond, and A. Schwery, "Large low-speed hydro-generators - unbalanced magnetic pulls and additional damper losses in eccentricity conditions," *IET Electric Power Applications*, vol. 1, no. 5, pp. 657–664, Sep 2007.
- [42] E. Wiedemann and W. Kellenberger, *Konstruktion elektrischer Maschinen*. Springer Berlin Heidelberg, 1967.
- [43] *Rotating electrical machines - Part 2-1: Standard methods for determining losses and efficiency from tests (excluding machines for traction vehicles)*, IEC 60034-2-1:2014 Std., 2014.
- [44] S. Heier, *Windkraftanlagen*. B. G. Teubner, Wiesbaden, 2005.
- [45] D. Krug, S. Bernet, S. S. Fazel, K. Jalili, and M. Malinowski, "Comparison of 2.3-kV medium-voltage multilevel converters for industrial medium-voltage drives," *IEEE Transactions on Industrial Electronics*, vol. 54, no. 6, pp. 2979–2992, Dec 2007.
- [46] H. Abu-Rub, S. Bayhan, S. Moinoddin, M. Malinowski, and J. Guzinski, "Medium-voltage drives: Challenges and existing technology," *IEEE Power Electronics Magazine*, vol. 3, no. 2, pp. 29–41, 2016.
- [47] A. Dekka, B. Wu, R. L. Fuentes, M. Perez, and N. R. Zargari, "Evolution of topologies, modeling, control schemes, and applications of modular multilevel converters," *IEEE Journal of Emerging and Selected Topics in Power Electronics*, vol. 5, no. 4, pp. 1631–1656, Dec 2017.
- [48] B. Wu and M. Narimani, *High-Power Converters and AC Drives*. John Wiley & Sons, Inc., 2017.
- [49] F. Filsecker, R. Alvarez, and S. Bernet, "Comparison of 4.5-kV press-pack IGBTs and IGCTs for medium-voltage converters," *IEEE Transactions on Industrial Electronics*, vol. 60, no. 2, pp. 440–449, Feb 2013.
- [50] S. Bernet, R. Teichmann, A. Zuckerberger, and P. Steimer, "Comparison of high-power igbt's and hard-driven gto's for high-power inverters," *Industry Applications, IEEE Transactions on*, vol. 35, pp. 487 – 495, Apr 1999.

- [51] D. Jovcic, *High Voltage Direct Current Transmission: Converters, Systems and DC Grids*. Wiley, 2019.
- [52] Infineon, “IGBT-modules,” [Online], <https://www.infineon.com/cms/de/product/power/igbt/igbt-modules/>, [Accessed: Aug 2019].
- [53] Mitsubishi Electric, “GCT (Gate Commutated Turn-off) Thyristor FGC6000AX-120DS,” datasheet, 2019.
- [54] ABB Switzerland Ltd., “Asymmetric Integrated Gate-Commutated Thyristor 5SHY 42L6500,” datasheet, 2012.
- [55] —, “Asymmetric Integrated Gate-Commutated Thyristor 5SHY 55L4500,” datasheet, 2013.
- [56] J. Hossain and A. Mahmud, Eds., *Large Scale Renewable Power Generation*. Springer, Singapore, 2014.
- [57] S. Rohner, S. Bernet, M. Hiller, and R. Sommer, “Modulation, losses, and semiconductor requirements of modular multilevel converters,” *IEEE Transactions on Industrial Electronics*, vol. 57, no. 8, pp. 2633–2642, Aug 2010.
- [58] S. Du, A. Dekka, B. Wu, and N. Zargari, *Modular Multilevel Converters: Analysis, Control, and Applications*. Wiley-IEEE Press, 2018.
- [59] S. Milovanovic and D. Dujic, “On power scalability of modular multilevel converters: Increasing current ratings through branch paralleling,” *IEEE Power Electronics Magazine*, vol. 7, no. 2, pp. 53–63, Jun 2020.
- [60] M. R. Islam, Y. Guo, and J. Zhu, “A transformer-less compact and light wind turbine generating system for offshore wind farms,” in *2012 IEEE International Conference on Power and Energy (PECon)*, Kota Kinabalu, Malaysia, 2012, pp. 605–610.
- [61] Benshaw Inc., “M2L 3000 Series, Medium voltage variable frequency drive,” product brochure, 2018.
- [62] J. Rodriguez, J.-S. Lai, and F. Z. Peng, “Multilevel inverters: A survey of topologies, controls, and applications,” *IEEE Transactions on Industrial Electronics*, vol. 49, no. 4, pp. 724–738, Aug 2002.

- [63] M. Malinowski, K. Gopakumar, J. Rodriguez, and M. A. Perez, "A survey on cascaded multilevel inverters," *IEEE Transactions on Industrial Electronics*, vol. 57, no. 7, pp. 2197–2206, Jul 2010.
- [64] A. Dekka, A. Ramezani, S. Ounie, and M. Narimani, "A new 5-level voltage source inverter," in *2019 IEEE Applied Power Electronics Conference and Exposition (APEC)*, Anaheim, CA, USA, 2019, pp. 2511–2515.
- [65] D. Xiao, S. Ounie, and M. Narimani, "A new five-level T-type converter with SPWM for medium-voltage applications," in *2019 IEEE 28th International Symposium on Industrial Electronics (ISIE)*, Vancouver, BC, Canada, 2019, pp. 2015–2020.
- [66] P. Wheeler, J. Rodriguez, J. C. Clare, L. Empringham, and A. Weinstein, "Matrix converters: A technology review," *IEEE Transactions on Industrial Electronics*, vol. 49, no. 2, pp. 276–288, Apr 2002.
- [67] J. W. Kolar, T. Friedli, J. Rodriguez, and P. W. Wheeler, "Review of three-phase PWM AC-AC converter topologies," *IEEE Transactions on Industrial Electronics*, vol. 58, no. 11, pp. 4988–5006, Nov 2011.
- [68] J. Zhang, L. Li, and D. G. Dorrell, "Control and applications of direct matrix converters: A review," *Chinese Journal of Electrical Engineering*, vol. 4, no. 2, pp. 18–27, Jun 2018.
- [69] M. Vasiladiotis, R. Baumann, C. Haederli, and J. Steinke, "IGCT-based direct AC/AC modular multilevel converters for pumped hydro storage plants," in *2018 IEEE Energy Conversion Congress and Exposition (ECCE)*, Portland, OR, USA, 2018, pp. 4837–4844.
- [70] H. J. Knaak, "Modular multilevel converters and HVDC/FACTS: A success story," in *Proceedings of the 2011 14th European Conference on Power Electronics and Applications*, Birmingham, UK, 2011, pp. 1–6.
- [71] A. J. Korn, M. Winkelkemper, and P. Steimer, "Low output frequency operation of the modular multi-level converter," in *2010 IEEE Energy Conversion Congress and Exposition*, Atlanta, GA, USA, 2010, pp. 3993–3997.
- [72] S. Sau and B. G. Fernandes, "Modular multilevel converter based variable speed drives with constant capacitor ripple voltage for wide speed range," in *IECON*

- 2017 - 43rd Annual Conference of the IEEE Industrial Electronics Society, Beijing, China, 2017, pp. 2073–2078.
- [73] M. Hagiwara, I. Hasegawa, and H. Akagi, "Startup and low-speed operation of an adjustable-speed motor driven by a modular multilevel cascade inverter (MMCI)," in *2012 IEEE Energy Conversion Congress and Exposition (ECCE)*, Raleigh, NC, USA, 2012, pp. 718–725.
- [74] Y. Okazaki, W. Kawamura, M. Hagiwara, H. Akagi, T. Ishida, M. Tsukakoshi, and R. Nakamura, "Which is more suitable for MMCC-based medium-voltage motor drives, a DSCC inverter or a TSBC converter?" in *2015 9th International Conference on Power Electronics and ECCE Asia (ICPE-ECCE Asia)*, Seoul, South Korea, 2015, pp. 1053–1060.
- [75] Siemens AG, "Sinamics GM150 and SM150 Medium-Voltage Drives," product brochure, 2008.
- [76] GE, "MV7000, Reliable, high performance medium voltage drive," product brochure, 2013.
- [77] —, "MV7-Series, Ultimate waverform multi-level high power drive," product brochure, 2015.
- [78] Toshiba Mitsubishi-Electric Industrial Systems Corporation, "TMdrive - XL85 product application guide," product brochure, 2015.
- [79] Siemens AG, "Sinamics perfect harmony GH150," product brochure, 2017.
- [80] GE, "GE's MV7-5L converter with UWave technology provides compact solution enabling hydroelectric production at the heart of Ottawa," [Online], 2017, available: <https://www.gepowerconversion.com/press-releases/ge>, [Accessed: Aug 2019].
- [81] FZ800R33KF2C, Infineon Technologies AG, 2013. [Online]. Available: <http://www.infineon.com/>
- [82] "IEEE recommended practice and requirements for harmonic control in electric power systems," *IEEE Std 519-2014 (Revision of IEEE Std 519-1992)*, pp. 1–29, 2014.

- [83] A. Muetze, "Bearing currents in inverter-fed AC-motors," dissertation, TU Darmstadt, Darmstadt, DE, 2004.
- [84] S. S. Fazel, "Investigation and comparison of multi-level converters for medium voltage applications," dissertation, TU Berlin, Berlin, DE, 2007.
- [85] S. Rodrigues, A. Papadopoulos, E. Kontos, T. Todorovic, and P. Bauer, "Steady-state loss model of half-bridge modular multilevel converters," *IEEE Transactions on Industry Applications*, vol. 52, no. 3, pp. 2415–2425, May-Jun 2016.
- [86] K. B. Shah and H. Chandwani, "Reduced switching-frequency voltage balancing technique for modular multilevel converters," in *2017 International Conference on Intelligent Sustainable Systems (ICISS)*, Palladam, India, 2017, pp. 289–294.
- [87] T. Holzer, J. Bacher, and A. Muetze, "Damper winding harmonics analysis of an electrically excited synchronous machine at power converter supply," in *2020 IEEE International Conference on Electrical Machines (ICEM)*, Gothenburg, Sweden, 2020, pp. 1092–1098.
- [88] J. Bacher, "Aufteilung der Rueckwirkungsdurchflutung beim transienten Betrieb der Synchronmaschine zwischen Daempferwicklung und daempferwirkenden massiven Bauteilen," dissertation, TU Graz, Graz, Austria, 2002.
- [89] W. Schuisky, "Ueber die Stromverteilung im Anlaufkaefig eines Synchronmotors," in *Elektrotechnik und Maschinenbau*, 1940.
- [90] G. Holzer, "Allgemeines zum Entwurf elektrischer Maschinen," lecture notes, TU Wien, Vienna, Austria, n.d.
- [91] D. Zarko, "Design of synchronous permanent magnet motors," lecture notes, TU Graz, Graz, Austria, 2016.



# Appendix A

## Computation of the Power Loss of the Synchronous Generator

This Section details the computation method for the various sources of power loss of the electrically excited salient-pole synchronous motor-generator, which is used in Chapter 4 to evaluate the costs for power loss during operation of the motor-generator utilizing the power loss evaluation cost factors presented in Section 3.2.2. Based on a simplified model, the total power loss comprises the load dependent power losses  $P_{\text{load}}$  and the constant power losses  $P_{\text{const}}$ .

### A.1 Load Dependent Power Losses

The load dependent power losses  $P_{\text{load}}$  comprise the resistive power loss of the stator winding  $P_{\text{cu,s}}$ , the current dependent power loss due to skin effect  $P_{\text{cu,s,skin}}$ , the additional current dependent power loss of the Roebel bars  $P_{\text{cu,s,add}}$ , and the resistive power loss of the field winding  $P_{\text{cu,f}}$ .

#### Resistive Power Loss of the Stator Winding

The resistance of a single stator phase  $R_{\text{ph}}$  can be computed with

$$R_{\text{ph}} = \frac{w_{\text{ph}} \cdot l_w}{\kappa_{\text{cu}} \cdot A_{\text{cu}} \cdot a'} \quad (\text{A.1})$$

where  $w_{\text{ph}}$  is the number of phase winding turns,  $l_w$  is the total length of a single winding turn,  $\kappa_{\text{cu}}$  is the electrical conductivity of copper,  $A_{\text{cu}}$  is the copper cross section, and  $a$  is the number of parallel paths. The resistive power loss of the stator

winding  $P_{\text{cu,s}}$  results from

$$P_{\text{cu,s}} = m \cdot R_{\text{ph}} \cdot I_{\text{ph}}^2, \quad (\text{A.2})$$

where  $m$  is the number of phases and  $I_{\text{ph}}$  is the stator current of the synchronous machine.

### Skin Effect and Additional Current Dependent Power Loss

To accommodate the skin effect, the reduced copper height  $\xi$  can be computed [90]:

$$\xi = h_{\text{cu}} \cdot \sqrt{\omega \cdot \mu_0 \cdot \kappa_{\text{cu}} \cdot \frac{w_{\text{cu}}}{2 \cdot w_{\text{s}}}}, \quad (\text{A.3})$$

where  $h_{\text{cu}}$  is the height of the conductor,  $\omega$  is the electrical angular frequency,  $w_{\text{cu}}$  is the width of the conductor, and  $w_{\text{s}}$  is the width of the slot. With the reduced copper height  $\xi$  the following two factors can be computed [90]:

$$\varphi = \xi \cdot \frac{\sinh(2\xi) + \sin(2\xi)}{\cosh(2\xi) - \cos(2\xi)}, \quad (\text{A.4})$$

$$\psi = 2 \cdot \xi \cdot \frac{\sinh(\xi) - \sin(\xi)}{\cosh(\xi) + \cos(\xi)}. \quad (\text{A.5})$$

For consideration of the utilized Roebel bars,  $k_{\text{RN}}$  can be computed [90]:

$$k_{\text{RN}} = \varphi + \frac{a_{\text{sc}}^2 - 1}{3} \cdot \psi, \quad (\text{A.6})$$

where  $a_{\text{sc}}$  is the number of subconductors of the Roebel bar. The increase of the resistance  $k_{\text{R}}$  results from [90]

$$k_{\text{R}} = (k_{\text{RN}} - 1) \cdot \frac{l}{l + l_{\text{ew}}} + 1, \quad (\text{A.7})$$

where  $l$  is the axial length of the machine and  $l_{\text{ew}}$  is the length of the end-winding.

The current dependent power loss due to the skin effect  $P_{\text{cu,s,skin}}$  results from [90]

$$P_{\text{cu,s,skin}} = m \cdot R_{\text{ph}} \cdot (k_{\text{R}} - 1) \cdot I_{\text{ph}}^2. \quad (\text{A.8})$$

The additional current dependent power loss of the Roebel bars  $P_{\text{cu,s,add}}$  is [90]

$$P_{\text{cu,s,add}} = V_0 \cdot \left(\frac{A}{500}\right)^2 \cdot \left(\frac{d \cdot l}{0.1 \cdot 2 \cdot p}\right)^{0.8}, \quad (\text{A.9})$$

where  $V_0 = 15000$  W for Roebel bars,  $A$  is the linear current density in A/cm,  $d$  is the stator inside diameter, and  $p$  is the number of pole-pairs.

### Resistive Power Loss of the Field Winding

The average coil length of the field winding  $l_f$  is [39]

$$l_f = 2 \cdot l + 2 \cdot \left( w_{pb} - 2 \cdot \frac{w_{cu,f}}{2} \right) + 2 \cdot \pi \cdot \frac{w_{cu,f}}{2}, \quad (\text{A.10})$$

where  $w_{pb}$  is the width of the pole body and  $w_{cu,f}$  is the width of the copper area of the field winding.

After choosing a proper field current  $I_f$ , the number of field winding turns per pole  $w_f$  can be computed with

$$w_f = \frac{\Theta_f}{I_f}, \quad (\text{A.11})$$

where  $\Theta_f$  is the magnetomotive force (mmf) of the field winding. The total resistance of the field winding  $R_{cu,f}$  results from

$$R_{cu,f} = \frac{l_f \cdot w_f}{\kappa_{cu} \cdot \frac{A_{cu,f}}{w_f}} \cdot 2 \cdot p, \quad (\text{A.12})$$

where  $A_{cu,f}$  is the copper cross section of the field winding.

The resistive power loss of the field winding  $P_{cu,f}$  is

$$P_{cu,f} = R_{cu,f} \cdot I_f^2. \quad (\text{A.13})$$

## A.2 Constant Power Losses

The constant power losses  $P_{\text{const}}$  comprise the stator iron power loss  $P_{fe}$  and the mechanical power loss  $P_{\text{mech}}$ .

### Stator Iron Power Loss

The factors  $k_h$ ,  $a_h$ ,  $b_h$ , and  $k_e$  can be extracted by curve fitting the values for the core losses of the utilized electric steel, which are prepared as a function of flux density and frequency, given in the data-sheet by the manufacturer, as described in [91]. The stator tooth flux density is then computed for three different positions, namely directly at the air-gap (0), in the middle of the stator slot ( $h_s/2$ ), and directly at the connection point of the stator tooth to the stator yoke ( $h_s$ ). The flux in the stator yoke  $\phi_{y,s}$  for each individual harmonic order  $\nu$  can be computed using the harmonics of the air-gap flux density  $B_\delta$  [91]

$$\phi_{y,s,\nu} = l \cdot \frac{d}{2} \cdot B_{\delta,\nu} \cdot \frac{1}{\nu \cdot p}, \quad (\text{A.14})$$

and the corresponding flux density in the stator yoke  $B_{y,s}$  results from [91]

$$B_{y,s,\nu} = \frac{|\phi_{y,s,\nu}|}{k_{fe} \cdot h_{y,s} \cdot l'} \quad (\text{A.15})$$

where  $k_{fe}$  is the iron fill factor and  $h_{y,s}$  is the stator yoke height. The flux in the stator teeth  $\phi_t$  for each individual harmonic order  $\nu$  can be computed using the harmonics of the air-gap flux density  $B_\delta$  [91]

$$\phi_{t,\nu} = l \cdot \frac{d}{2} \cdot B_{\delta,\nu} \cdot \frac{2}{\nu \cdot p} \cdot \left| \sin \left( \nu \cdot p \cdot \frac{\pi}{Q_s} \right) \right|, \quad (\text{A.16})$$

where  $Q_s$  is the number of stator slots. The corresponding flux density in the stator teeth  $B_t$  results from [91]

$$B_{t,\nu} = \frac{|\phi_{t,\nu}|}{k_{fe} \cdot w_t \cdot l'} \quad (\text{A.17})$$

where  $w_t$  is the width of the stator tooth.

The stator iron power loss in the yoke  $P_{fe,y}$  results from [91]

$$P_{fe,y} = \left[ k_h f B_{y,s}^{a_h + b_h B_{y,s}} + k_e f^2 \sum_{\nu=1,3}^{\nu_{\max}} \nu^2 B_{y,s,\nu}^2 \right] \rho_{fe} k_{fe} (d_o^2 - (d + 2h_s)^2) \frac{\pi}{4} l, \quad (\text{A.18})$$

where  $\rho_{fe}$  is the density of the electric steel,  $d_o$  is the stator outside diameter, and  $h_s$  is the stator slot height. The stator iron power loss in the teeth  $P_{fe,t}$  results from [91]

$$\begin{aligned} P_{fe,t} = Q_s \rho_{fe} k_{fe} h_s l \frac{1}{6} \left\{ \left[ k_h f [B_t(0)]^{a_h + b_h B_t(0)} + k_e f^2 \sum_{\nu=1,3}^{\nu_{\max}} \nu^2 [B_{t,\nu}(0)]^2 \right] w_t(0) + \right. \\ \left. + 4 \left[ k_h f \left[ B_t \left( \frac{h_s}{2} \right) \right]^{a_h + b_h B_t \left( \frac{h_s}{2} \right)} + k_e f^2 \sum_{\nu=1,3}^{\nu_{\max}} \nu^2 \left[ B_{t,\nu} \left( \frac{h_s}{2} \right) \right]^2 \right] w_t \left( \frac{h_s}{2} \right) + \right. \\ \left. + \left[ k_h f [B_t(h_s)]^{a_h + b_h B_t(h_s)} + k_e f^2 \sum_{\nu=1,3}^{\nu_{\max}} \nu^2 [B_{t,\nu}(h_s)]^2 \right] w_t(h_s) \right\}. \quad (\text{A.19}) \end{aligned}$$

The total stator iron power loss is

$$P_{fe} = P_{fe,y} + P_{fe,t}. \quad (\text{A.20})$$

### Mechanical Power Loss

The bearing friction and windage loss can be computed with [38]

$$P_{\text{mech}} = 0.8 \cdot (1.7 + 0.4 \cdot d) \cdot \left( \frac{1.75}{d} \right)^{0.1} \cdot \left( \frac{n}{428} \right)^{0.4} \cdot d^3 \cdot n^2 \cdot \sqrt{l} \cdot 0.01, \quad (\text{A.21})$$

where  $n$  is the rotational speed in rpm and  $P_{\text{mech}}$  is in W.

## Appendix B

# Power Loss and Cost Distribution of the Generator Designs for FSC Operation

The cost of the electrically excited synchronous motor-generator presented in Section 3.2.2 is calculated using the costs for the active material, namely, the stator iron, the rotor iron, and the copper. The distribution of the generator's mass between the stator and the rotor is displayed in Figure 4.2. In addition, the costs for the load dependent power losses as well as the costs for the constant power losses (load independent power losses) during operation are taken into account.

### B.1 Power Loss Distribution

Figure B.1 shows the power loss distribution of the 135 MW, 200 rpm, unity power factor generator designs for various design frequencies which are analyzed in Section 4.2. The total power loss follows the efficiency illustrated in Figure 4.1 inversely, which means that the minimum total power loss results for the 50 Hz design and is 1.23 MW. The total power loss increases for higher design frequencies. This increase of the total power loss is mainly attributed to the increased stator iron power loss at higher design frequencies. The stator iron power loss is 115.6 kW and 384.8 kW for the 30 Hz and the 140 Hz design respectively, which relates to a significant increase by a factor of 3.3.

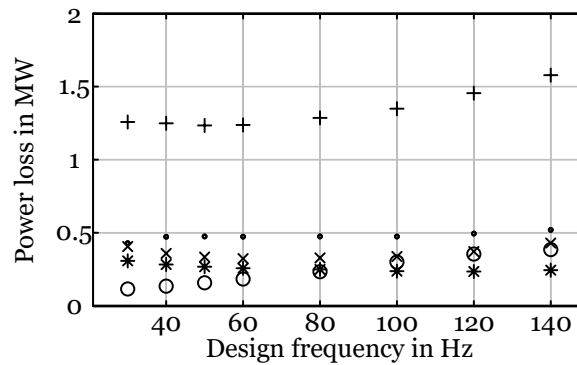


**Figure B.1:** Power loss distribution of the unity power factor generator designs for various design frequencies; + = total power loss, × = load dependent power loss of the stator, \* = field winding power loss, o = stator iron power loss, · = mechanical power loss.

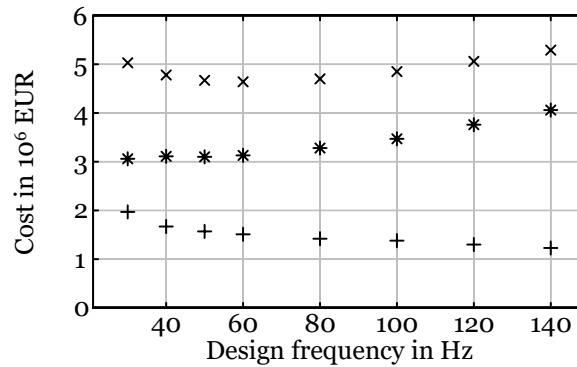


**Figure B.2:** Cost distribution of the unity power factor designs for various design frequencies; × = total cost, + = costs for material, \* = costs for power loss.

## B.2 Cost Distribution

Figure B.2 illustrates the total cost as well as the distribution of the generator’s cost between the costs for materials and the costs for power loss.

### Costs for Materials

The costs for materials follow the trend of the generator’s mass shown in Figure 4.1.

### Costs for Power Loss

The costs for power loss in Figure B.2, however, do not follow the trend of the total power loss presented in Figure B.1: While the total power loss has a minimum

at 50 Hz, the costs for power loss decrease towards lower design frequencies because of the different power loss evaluation cost factors for the load dependent power losses  $C_{\text{load}} = 2000 \text{ EUR/kW}$  and the constant power losses  $C_{\text{const}} = 3000 \text{ EUR/kW}$ . Particularly the stator iron power loss, which increases significantly for higher design frequencies, is rated with the power loss evaluation cost factor for constant power losses.

### Total Cost

The total cost of the generator designs results from the sum of the costs for materials and the costs for power loss. The 60 Hz machine design reveals the minimum cost of  $4.64 \cdot 10^6 \text{ EUR}$  for the analysis presented in Section 4.2.1.



## Appendix C

# Generator Design for Operation at a Load Profile for Common Design Frequencies

As discussed in Section 4.3.3, the load profile of the motor-generator influences the power loss distribution during operation and thus affects the generator designs created by the cost minimization generator design algorithm, as long as the power loss evaluation cost factors for load dependent and for constant power losses differ. To better illustrate this effect, the values presented in Section 4.3.3 are the results for a 135 MW, 120 Hz, 200 rpm,  $\cos \varphi = 1$  generator design with the power loss evaluation cost factors  $C_{\text{load}} = 4000$  EUR/kW and  $C_{\text{const}} = 8000$  EUR/kW. Utilizing these parameters leads to a reduction in the actual cost (comprising costs for materials and costs for power loss during operation) of the generator of 0.7% when comparing the costs for SG1 and SG3 operating at the load profile in both turbine and pumping modes (T + P), see Table 4.5.

This Section shows the results for a 135 MW, 50 Hz, 200 rpm,  $\cos \varphi = 1$  generator design, utilizing the initial power loss evaluation cost factors  $C_{\text{load}} = 2000$  EUR/kW and  $C_{\text{const}} = 3000$  EUR/kW presented in Section 3.2.2. The load profile shown in Table 4.3 is used for this analysis which shows quite severe partial load behavior (operating 80% of the time at  $\leq 75\%$  of the nominal load), and a real power plant might not require such drastic behavior.

Two different generators have been designed, each with a different optimization objective:

- SG4: minimum costs for nominal load operation
- SG5: minimum costs occurring over the course of the operating profile for both turbine and pumping modes (T + P)

Thereby, the role of the operating profile, i.e., consideration of partial load operation, in the generator design shall be identified.

## C.1 Power Loss Distribution

Table C.1 shows the power loss distribution (load dependent power losses  $P_{\text{load}}$  and constant power losses  $P_{\text{const}}$ ) of the two generator designs evaluated for nominal load in comparison to the reference motor-generator design SG4. It illustrates the changes in the power loss distribution of the motor-generator designs when using the two different optimization objectives listed above. As stated in Section 4.3.3, when operating at partial load, both in turbine and pumping modes, all the power loss sources decrease. Thus, the ratios between the different types of power loss do not change significantly and thus no power loss type can be specifically addressed during the design. Utilizing a design frequency of 50 Hz and the initial power loss evaluation cost factors, the constant power losses  $P_{\text{const}}$  decrease by 0.5 %, while the load dependent power losses  $P_{\text{load}}$  increase by 0.3 % for SG5 compared to SG4.

## C.2 Cost

Table C.2 depicts the actual cost of SG4 (comprising costs for materials and costs for power loss), which was originally designed to minimize the cost for nominal load operation when operating SG4 at the load profile including both turbine and pumping modes (T + P). These costs are compared with the costs of the generator specifically designed to minimize the cost for the operating profile (SG5) in both turbine and pumping modes. It shows a cost reduction of SG5 of 0.025 % when comparing the costs of SG4 and SG5 operating at the load profile presented in Table 4.3 in both turbine and pumping modes (T + P).

**Table C.1:** Power loss distribution of the generator designs evaluated for nominal load compared to the reference design SG4; T + P = turbine and pumping modes.

Design	Minimization target	$P_{\text{load}}$ pu	$P_{\text{const}}$ pu
SG4	Nominal load	1.000	1.000
SG5	Load profile T + P	1.003	0.995

**Table C.2:** Total cost of the generator designs evaluated for operation at the load profile presented in Table 4.3 for both turbine and pumping modes (T + P).

Design	Minimization target	Modes of operation	Cost $10^6$ EUR
SG4	Nominal load	T + P	4.023
SG5	Load profile T + P	T + P	4.022

### C.3 Summary

The achieved cost reduction of only 0.025 % highlights the fact that the operating profile only marginally affects the design of the synchronous motor-generator when utilizing a design frequency of 50 Hz and similar power loss evaluation cost factors for the load dependent and the constant power losses, like the initial power loss evaluation cost factors presented in Section 3.2.2.



# Appendix D

## Analytic Average Loss Model of the Modular Multilevel Converter

This Section reviews the analytic average loss model of the modular multilevel converter (MMC) to compute the performance of the full-size converter (including both machine and grid side) in the total system evaluation of the pumped storage power plant. The model uses the parameters described in Section 6.1.1 and the IGBT-module “FZ800R33KF2C” [81]. The schematic of a single DC-AC stage of the MMC can be found in Figure 6.1. The calculation method for the analytic average loss model described in [16] has been extended to consider the number of IGBT modules in parallel  $n_{\text{IGBT}}$ .

Note that this calculation approach does not depend on the output frequency  $f$  of the MMC but on the switching frequency of each individual IGBT-module  $f_s$ . The average switching frequency of the semiconductor power switches is derived from the simulation model of the MMC implemented in MATLAB / Simulink presented in Section 6.1.4.

### D.1 Average Currents Through the Semiconductor Power Devices

The active power required from the DC-link  $P$  is

$$P = 3 \cdot U_{\text{ph}} \cdot I_{\text{ph}} \cdot \cos\varphi \quad (\text{D.1})$$

and the DC-link current  $I_{\text{DC}}$  is

$$I_{\text{DC}} = \frac{P}{U_{\text{DC}}}. \quad (\text{D.2})$$

Assuming sinusoidal waveforms, the peak value  $\hat{I}_W$  and the absolute value  $|\bar{I}_W|$  of the MMC phase current can be computed as follows [16]:

$$\hat{I}_W = \sqrt{2} \cdot I_{ph} \quad \text{and} \quad |\bar{I}_W| = \frac{2}{\pi} \cdot \hat{I}_W. \quad (\text{D.3})$$

The normalized ratio between the AC and DC currents  $y$ , the factor  $x$ , which relates to the dimensioning of the submodule capacitors, and the relative amplitude of the DC voltage controlled by the converter  $b$  can be computed as follows [85]:

$$y = \frac{3 \cdot \pi \cdot |\bar{I}_W|}{4 \cdot I_{DC}}, \quad x = \left(1 - y^{-2}\right)^{\frac{3}{2}} \quad \text{and} \quad b = \frac{U_{DC}}{2 \cdot n \cdot U_{SM}}. \quad (\text{D.4})$$

The average currents for the power semiconductor devices of each submodule, see Figure 6.1, result from [16]:

$$\bar{i}_{Q1} = \frac{1}{4} \cdot b \cdot x \cdot |\bar{I}_W|. \quad (\text{D.5})$$

$$\bar{i}_{D1} = \frac{1}{4} \cdot b \cdot x \cdot |\bar{I}_W|. \quad (\text{D.6})$$

$$\bar{i}_{Q2} = \frac{1}{4} \cdot (1 - b \cdot x) \cdot |\bar{I}_W| + \frac{1}{6} \cdot I_{DC} \cdot \left(1 + \frac{1}{3 \cdot y}\right). \quad (\text{D.7})$$

$$\bar{i}_{D2} = \frac{1}{4} \cdot (1 - b \cdot x) \cdot |\bar{I}_W| + \frac{1}{6} \cdot I_{DC} \cdot \left(1 - \frac{1}{3 \cdot y}\right). \quad (\text{D.8})$$

## D.2 On-State Power Loss

The equivalent on-state currents for positive and negative current direction are computed as follows [85]:

$$I_{on,p}^* = \frac{I_{DC}}{3} \cdot (y + 1) \cdot \frac{\pi}{4} \quad \text{and} \quad (\text{D.9})$$

$$I_{on,n}^* = \frac{I_{DC}}{3} \cdot (y - 1) \cdot \frac{\pi}{4}. \quad (\text{D.10})$$

The voltage drops at the semiconductor power devices can be determined using the output characteristics for the IGBT and the diode given in the data-sheet of the IGBT-module [81]:

$$U_{CE,p} = fcn\left(\frac{I_{on,p}^*}{n_{IGBT}}\right) \quad \text{and} \quad U_{CE,n} = fcn\left(\frac{I_{on,n}^*}{n_{IGBT}}\right). \quad (D.11)$$

$$U_{F,p} = fcn\left(\frac{I_{on,p}^*}{n_{IGBT}}\right) \quad \text{and} \quad U_{F,n} = fcn\left(\frac{I_{on,n}^*}{n_{IGBT}}\right). \quad (D.12)$$

Next, the on-state power loss of the individual power semiconductor devices is computed as follows [85]:

$$P_{on,Q1} = \frac{\bar{i}_{Q1}}{n_{IGBT}} \cdot U_{CE,n} \cdot n_{IGBT}. \quad (D.13)$$

$$P_{on,D1} = \frac{\bar{i}_{D1}}{n_{IGBT}} \cdot U_{F,p} \cdot n_{IGBT}. \quad (D.14)$$

$$P_{on,Q2} = \frac{\bar{i}_{Q2}}{n_{IGBT}} \cdot U_{CE,p} \cdot n_{IGBT}. \quad (D.15)$$

$$P_{on,D2} = \frac{\bar{i}_{D2}}{n_{IGBT}} \cdot U_{F,n} \cdot n_{IGBT}. \quad (D.16)$$

## D.3 Switching Power Loss

The average current for a positive current direction (see Figure 6.1)  $\bar{i}_{arm,p}$  results from [85]

$$\bar{i}_{arm,p} = \frac{1}{6} \cdot I_{DC} \cdot \left( \frac{2 \cdot y}{\pi} + 1 + \frac{1}{3 \cdot y} \right) \quad (D.17)$$

and the average current for a negative current direction (see Figure 6.1)  $\bar{i}_{arm,n}$  results from [85]

$$\bar{i}_{arm,n} = \frac{1}{6} \cdot I_{DC} \cdot \left( \frac{2 \cdot y}{\pi} - 1 + \frac{1}{3 \cdot y} \right). \quad (D.18)$$

Utilizing an average switching frequency  $f_s$ , the switching power loss of the individual power semiconductor devices can be computed as follows [85]:

$$P_{s,Q1} = f_s \cdot \left( \frac{W_{\text{on}} + W_{\text{off}}}{P_{\text{ref}}} \right) \cdot U_{\text{SM}} \cdot \frac{\bar{i}_{\text{arm},n}}{n_{\text{IGBT}}} \cdot n_{\text{IGBT}}. \quad (\text{D.19})$$

$$P_{s,D1} = f_s \cdot \left( \frac{W_{\text{rec}}}{P_{\text{ref}}} \right) \cdot U_{\text{SM}} \cdot \frac{\bar{i}_{\text{arm},p}}{n_{\text{IGBT}}} \cdot n_{\text{IGBT}}. \quad (\text{D.20})$$

$$P_{s,Q2} = f_s \cdot \left( \frac{W_{\text{on}} + W_{\text{off}}}{P_{\text{ref}}} \right) \cdot U_{\text{SM}} \cdot \frac{\bar{i}_{\text{arm},p}}{n_{\text{IGBT}}} \cdot n_{\text{IGBT}}. \quad (\text{D.21})$$

$$P_{s,D2} = f_s \cdot \left( \frac{W_{\text{rec}}}{P_{\text{ref}}} \right) \cdot U_{\text{SM}} \cdot \frac{\bar{i}_{\text{arm},n}}{n_{\text{IGBT}}} \cdot n_{\text{IGBT}}. \quad (\text{D.22})$$

## D.4 Total Power Loss and Efficiency

Considering a three-phase configuration with two arms per phase and a number of  $n$  submodules per arm, the total on-state power loss  $P_{\text{on}}$  and the total switching power loss  $P_s$  of a single DC-AC conversion stage are computed:

$$P_{\text{on}} = 3 \cdot 2 \cdot n \cdot (P_{\text{on},Q1} + P_{\text{on},D1} + P_{\text{on},Q2} + P_{\text{on},D2}) \quad (\text{D.23})$$

$$P_s = 3 \cdot 2 \cdot n \cdot (P_{s,Q1} + P_{s,D1} + P_{s,Q2} + P_{s,D2}). \quad (\text{D.24})$$

The total power loss of a single DC-AC conversion stage of the MMC is computed as follows:

$$P_{\text{d,DC-AC}} = P_{\text{on}} + P_s. \quad (\text{D.25})$$

The efficiency of a single DC-AC conversion stage of the MMC  $\eta_{\text{DC-AC}}$  results from  $P_{\text{d,DC-AC}}$  and the active power  $P$  delivered:

$$\eta_{\text{DC-AC}} = \frac{P - P_{\text{d,DC-AC}}}{P}. \quad (\text{D.26})$$

It is assumed that the rectifier stage and the inverter stage operate at the same average switching frequency and are built of two identical units. The total efficiency of the MMC  $\eta_{\text{MMC}}$  results from the product of one DC-AC conversion stage operating as a rectifier and one DC-AC conversion stage operating as an inverter:

$$\eta_{\text{MMC}} = \eta_{\text{DC-AC,rectifier}} \cdot \eta_{\text{DC-AC,inverter}}. \quad (\text{D.27})$$

# Appendix E

## Test Bench Equipment and Measurement System

### E.1 Electrical Machines and Supplies

#### Synchronous Machine Under Test

Selected machine parameters of the custom-built electrically excited synchronous machine (SM) under test are illustrated in Table 7.1. The field winding of the SM is supplied by an “Argos DC power supply” from TET Electronic (160 V, 6.5 A).

#### Driving Machine

The nameplate of the permanent magnet synchronous machine (PMSM) can be found in Table E.1. The PMSM is used to drive the SM and can also be used to apply a load to the SM under test. The PMSM is supplied by a “b maXX 4000” from Baumüller.

**Table E.1:** Nameplate of the PMSM (Baumüller, DS 132 B23R30-5, serial number: 21030516).

$P$	$U_{ll}$	$f$	$n$	$\cos \varphi$
kW	V	Hz	rpm	-
92	350	150	3000	0.95

### **Power Amplifier**

The power amplifier “DM 15000/PAS” from Spitzenberger + Spies allows generating arbitrary voltage waveforms and is used to supply the SM under test with voltage waveforms of various power converter topologies. The rated data is as follows: 3 x 5 kVA, AC: 270 V rms, DC: 382 V.

## **E.2 Measurement System**

The measurement system “DEWE-5000” from Dewetron merges the following measurement devices:

### **Voltage Measurement**

- Dewetron DAQP-HV, isolated high-voltage module, 7 ranges ( $\pm 20$  V to  $\pm 1400$  V), bandwidth: 300 kHz.

### **Current Measurement**

- Dewetron DAQP-LV, isolated low-voltage module, 12 ranges (10 mV to 50 V), bandwidth: 300 kHz.
- STW ELAS HBR 10, ratio: 10 mV/mA.
- Signaltec MCTS.
- LEM IT 60-S Ultrastab, 60 A, ratio: 1:600.

### **Measurement of the Voltage Drops at the Individual Damper Bars**

- Dewetron DAQP-LV, isolated low-voltage module, 12 ranges (10 mV to 50 V), bandwidth: 300 kHz.
- Rie-Tech slip ring transducer SRK 80, 24 poles, voltage range: mV to 60 V, current range: mA to 4 A, max. speed: 6000 rpm.

### Torque Measurement

- Dewetron DAQP-HV, isolated high-voltage module, 7 ranges ( $\pm 20$  V to  $\pm 1400$  V), bandwidth: 300 kHz.
- Kistler CoMo Torque, type: 4700BP0UN, serial number: 4946544.
- Kistler torque transducer, type: 4503A500WA2B1C00, serial number: 117507, range: 500 Nm (ext. range: 100 Nm), max. speed: 7000 rpm.

## E.3 Measurement Procedure

This Section describes the measurement procedure for load operation of the SM under test at various power converter supplies presented in Section 8.2.2.

Because of the damper windings of the SM, the machine can start-up like an induction machine and can then be synchronized by increasing the field current. Hence, no complex synchronization strategy is required.

The full-size converter voltage waveform of interest is loaded into the software of the power amplifier. After applying this waveform to the output of the power amplifier, the voltage is ramped up manually to achieve operation close to the synchronous speed. Next, the field current is increased to enable an over-excited no-load operation. At this point, the machine rotates with its synchronous speed of 1500 rpm and the stator voltage is adjusted via the power amplifier to provide an rms value of the phase voltage of 130 V. Then, the SM gets loaded gradually utilizing the PMSM, which is connected to the SM via a common shaft, see Figure 7.1, until the desired load torque, i.e., 16.6 Nm, is reached. Lastly, the SM's field current is adjusted to allow for unity power factor operation. After the SM under test reaches the steady operating point under load condition, the quantities of interest are measured, namely, the stator voltage, the stator current, the field current, the torque, the rotational speed, as well as the voltage drops at the individual damper bars.